PLANAR TUNNELING AND ANDREEV BOUND STATE SPECTROSCOPY OF $YBa_2Cu_3O_{7-\delta}$ THIN FILMS USING SOLUTION-DEPOSITED ZIRCONIA INSULATORS

BY

PATRICK JAY HENTGES

B.A., Drury College, 1997
M.S., University of Illinois at Urbana-Champaign, 2000

DISSERTATION

Submitted in partial fulfillment of the requirements
for the degree of Doctor of Philosophy in Physics
in the Graduate College of the
University of Illinois at Urbana-Champaign, 2004

Urbana, Illinois

Abstract

Planar tunnel spectroscopic measurements are performed on $YBa_2Cu_3O_{7-\delta}$ (YBCO) thin films at four different crystallographic orientations. Since tunneling is a highly surface-sensitive probe on YBCO, films have been optimized for high surface quality. To fabricate the tunneling insulator, a novel fabrication technique has been developed through solution condensation and hydrolysis of zirconia, which has proven to be gentler to the surface than previous techniques. The result is a clean tunneling interface as shown in scanning electron microscopy, atomic force microscopy and transmission electron microscopy, that allows us to detect several new features in the tunneling conductance.

In addition, we have fabricated tunnel junctions with three different counter-electrode deposition techniques. In doing so, various behaviors of the tunneling conductance and its dependence on magnetic field, temperature, and injected current as a function of these counter-electrode deposition techniques has been observed. Modeling of the tunneling conductance has provided insight into the various behaviors. It has been shown that by varying the value of the tunneling cone, surface faceting and quasiparticle lifetime, in agreement with the observations, splitting *vs*. non-splitting of the zero-bias conductance peak can be understood.

Acknowledgements

Many thanks to my wife and family for steady encouragement during this long journey. Though it wasn't always clear how, they were always sure that I would do "just fine". Their confidence inspired my own. Next, I'd like to thank my advisor, Prof. Laura Greene, who made this work possible in every sense, and whose hands-off approach helped to maximize my understanding of Nature and of myself.

The success of this work is due in large part to our strong collaboration with members of Department of Chemistry at the University of Illinois, including Prof. Walter Klemperer, Glenn Westwood and Margaret Pafford. Their work made the zirconia coating process described here possible, and their fresh perspective helped us better understand the physics as well as the chemistry. Special thanks go to Glenn, my colleague in the graduate trenches, for his keen scientific instincts and who always went out of his way to accommodate my schedule.

I'd also like to thank the other group members with whom I had the pleasure of working. First, I'd like to thank Bill Feldmann, our technician or "secret weapon", for sharing his boundless technical knowledge, as well as the occasional sample of soup, cheese, beer, or other delicacy. I am indebted Wan Kyu Park, for many patient conversations regarding the modeling of our tunneling measurements. He has been an integral part of the development of this work. I'm grateful for the conscientious help of Chris Lesher with thin film characterization as well as for the new energy added to this work by Matthew Brinkley, who plans on picking up where I left off. I know I'm leaving the work in good hands. I also enjoyed valuable advice, discussions and collaborations early in my graduate career with Adam Abeyta, Hervé Aubin, Elvira Badica, Mark Covington, Elisabeth Dumont, Justin Elenewski and Igor Roshchin. Special thanks go to Hervé Aubin as well for his Matlab code, which provided the foundation for the conductance calculations in this work.

Finally, this work would not have been possible without help from outside our group. The outstanding staff at the Center for Microanalysis of Materials, including Scott MacLaren, Vania Petrova, Mauro Sardela and Jianguo Wen, were invaluable for thin film analysis. In addition, I’m honored to thank Micke Fögelstrom, Jochen Geerk, Donald Ginsberg, Paul Goldbart, John Rowell, James Sauls and Michael Stone, for fruitful and invigorating discussions. This material is based upon work supported by the U.S. Department of Energy, Division of Materials Sciences under Award No. DEFG02-91-ER45439, through the Frederick Seitz Materials Research Laboratory at the University of Illinois at Urbana-Champaign. Research for this publication was carried out in the Center for Microanalysis of Materials, University of Illinois at Urbana-Champaign, which is partially supported by the U.S. Department of Energy under grant DEFG02-91-ER45439.

Table of Contents

Chapter 1 Introduction......1

1.1 Motivation......1

1.2 Outline......3

Chapter 2 Background......4

2.1 Conventional Superconductors......4

Phenomenology
Microscopic Theory
Background on Tunneling

2.2 High-Temperature Superconductors......13

Andreev Bound States
Tunneling in YBCO: Early Techniques and Results

2.3 Planar Junction Fabrication Method......26

2.4 References......31

Chapter 3 Experimental Techniques......35

3.1 YBCO Thin Film Growth......35

YBCO Crystal Structure
Sputtering Basics
Substrate/Hardware Preparation
Thin Film Growth Process
YBCO Thin Film Characterization

3.2 Planar Tunnel Junction Fabrication......47

Tunnel Junctions with Zirconia Insulators

3.3 Tunneling Conductance Measurements......50

3.4 References......52

Chapter 4 Thin Films......54

4.1 YBCO Thin Film Analysis......54

X-Ray Diffraction
Scanning Electron Microscopy
Atomic Force Microscopy
Resistivity vs. *Temperature*

4.2 Insulating Thin Films of Zirconia......68

Transmission Electron Microscopy
Atomic Force Microscopy
Tunneling Spectroscopy

4.3 References......78

Chapter 5 Tunneling Measurements......79

5.1 Sharpness..80

5.2 Normalization: Removing the Background......................................82

5.3 (001)-Oriented YBCO...88
Statistics: (001)
Observed Characteristics: (001)

5.4 (100)-Oriented YBCO...96
Statistics: (100)
Observed Characteristics: (100)

5.5 (103)-Oriented YBCO...100
Statistics: (103)
Observed Characteristics: (103)

5.6 (110)-Oriented YBCO...103
Statistics: (110)
Observed Characteristics: (110)

5.7 Conclusions 107

5.8 References 110

Chapter 6 Andreev Bound State Studies 111

6.1 Temperature Dependence of ABS...111

6.2 Field Dependence of the ABS...115
Field Orientation Dependence
Field Magnitude Dependence: Splitting vs. *Non-Splitting of the ZBCP*
Doping Dependence of ABS Splitting

6.3 Modeling of the Tunneling Conductance..122
Effect of Disorder on the ABS

6.4 Current Injection Effects on the ABS 130

6.5 References 135

Chapter 7 Conclusions...136

Vita 139

Chapter 1

Introduction

1.1 Motivation

Understanding the mechanism of high-temperature superconductors (HTS) is among the most heavily studied areas in physics today. The interest in these materials comes from two properties of HTS materials. First, compared to conventional superconductors, the temperature for which the electrical resistance drops to zero, T_c, is typically an order of magnitude higher. Second, the physics of the microscopic mechanism is fundamentally different, and is not understood. Not only is it a subject of tremendous scientific interest, there are many exciting practical applications of HTS materials, including applications in electric utilities, energy storage, quantum computing, telecommunications, measurements standards and public transportation. At the center of much of this study is the compound $YBa_2Cu_3O_{7-\delta}$ (YBCO). YBCO is a ceramic compound which has poor conducting properties at room temperature but becomes a superconductor at about 90 K for certain chemical compositions (*i.e.*, certain values of δ). This is well above the boiling point of liquid nitrogen, making practical applications of YBCO and other similar HTS more economically feasible.

Despite the promise of the understanding of new physics and so many practical applications, HTS materials present great challenges in the understanding of underlying microscopic mechanism and the materials fabrication. The complex perovskite structure of YBCO and complex dependence of the superconducting properties on the charge carrier concentration, or doping, of the material makes materials and measurement reproducibility a challenge in many experiments, including tunneling spectroscopy. Planar tunneling spectroscopy is a powerful electron spectroscopic technique with high energy and momentum resolution and which provides a mechanically stable configuration for studying various dependencies such as temperature and magnetic field.

Because of the material complexity of YBCO, recent planar tunneling spectroscopy measurements from different research groups have produced varying results. Variations in material composition and tunnel junction fabrication techniques make the comparison of results from different groups difficult. Further complicating the situation is the two-fold problem of the surface of YBCO in these measurements. The first problem has to do with the extreme sensitivity of the YBCO surface to oxygen loss, degrading the surface superconducting properties. The second problem deals with the nature of tunneling spectroscopy in YBCO, which only probes this sensitive surface region. The focus of this thesis is to address this experimental controversy in three ways: first, by producing oriented YBCO thin films of exceptional surface quality; second, by fabricating tunneling insulators that impart as little surface damage as possible; and third, to perform the tunneling spectroscopy measurements using various counter-electrode deposition techniques, in attempt to reconcile previous results from various groups.

These objectives are achieved by employing a novel tunneling insulator deposition technique by solution-deposition of zirconia onto the as-grown YBCO surface. After the insulator is been deposited, three different counter-electrode deposition techniques are employed. These techniques, including thermal evaporation of silver, deposition of silver colloid paste and pressing of indium electrodes onto the zirconia-coated YBCO surface produce various results. Much of the interesting behavior occurs at low bias in our tunneling experiments, in the properties of the zero-bias conductance peak (ZBCP), though new and interesting behavior is observed throughout the spectrum in measurements that probe crystallographic orientation, temperature, magnetic field (magnitude and orientation) and current injection dependencies of the tunneling conductance.

1.2 Outline

The outline of this thesis is as follows. Chapter 2 provides detailed background information on the history and theory of conventional superconductors, particularly the role of tunneling spectroscopy. The history and background of tunneling is then given for HTS, including a discussion of the formation of Andreev bound states at the YBCO surface. Previous techniques for fabricating junctions on YBCO are also discussed.

Chapter 3 discusses the experimental methods of junction fabrication and measurement, including the details of YBCO thin film growth at four crystallographic orientations, the novel insulator deposition technique of solution-deposition of zirconia, and the conductance measurement procedure. In Chapter 4, we discuss the results of thin film analysis, both for the YBCO thin films and the solution-deposited zirconia insulating layers.

Chapters 5 and 6 present the results of our tunneling conductance measurements. Chapter 5 reports on the observed characteristics and reproducibility as a function of crystallographic orientation and counter-electrode deposition technique. Chapter 6 focuses on the studies of the Andreev bound state as a function of temperature, magnetic field and injected current. Modeling of the conductance spectrum is also presented in Chapter 6 in order to interpret the results. Conclusions are discussed in Chapter 7.

Chapter 2
Background

2.1 Conventional Superconductors

In 1911, three years after he first liquefied helium, Heike Kamerlingh-Onnes observed the electrical resistance in lead as it dropped precipitously below a critical temperature, T_c, thus discovering superconductivity [1]. This discovery earned him the Nobel Prize in Physics just two years later. As work continued, it was discovered that many more metals and metallic alloys exhibit the same zero-resistance property. In 1933, Meissner and Ochsenfeld discovered the second hallmark of superconductivity, i.e., that superconductors are also perfect diamagnets [2]. That is, magnetic fields are expelled from the bulk of superconductors up to a certain critical field, H_c – the field strength at which superconductive properties vanish. This field expulsion, the so-called Meissner effect, is produced by screening supercurrents, which flow within the London penetration depth (λ_L) [3] of the surface.

Phenomenology

The quantity λ_L was calculated in a phenomenological theory developed by two brothers, F. and H. London [4], to treat the electrodynamics of superconductors. They started with two equations. The first equation,

$$\mathbf{E} = \frac{\partial}{\partial t}(\Lambda \mathbf{J}_s) \quad \text{where} \quad \Lambda = \mu_0 \lambda_L^2 = \frac{m}{n_s e^2}, \tag{2.1}$$

describes perfect conductivity, where $\mathbf{J}_s$ is the supercurrent density, m is the electron mass n_s is the superfluid number density and e is the electron charge. The second equation,

$$\mathbf{B} = -\nabla \times (\Lambda \mathbf{J}_s), \qquad (2.2)$$

describes perfect diamagnetism, where **B** is the magnetic flux. Measurements of the penetration depth in various materials consistently show values higher than predicted by the London theory. This led Pippard [5] to extend the electrodynamic theory to include the concept of the coherence length, ξ_0, a measure of nonlocality in superconductors.

Pippard argued that if the phenomenon of superconductivity has an onset temperature of T_c, only electrons within $\sim k_B T_c$ of the fermi energy, E_F, can be major contributors. These electrons have a momentum range given by $\Delta p \approx k_B T_c / v_F$ where v_F is the Fermi velocity. According to the uncertainty principle, $\Delta x \gtrsim \hbar/\Delta p \approx \hbar v_F / k_B T_c$. Thus,

$$\xi_0 \propto \frac{\hbar v_F}{k_B T_c} \qquad (2.3)$$

The phenomenology of the superconducting electrons was further addressed by Ginzburg and Landau (GL) [6] who employed Landau's treatment of phase transitions to introduce an order parameter, ψ, which obeys Schrödinger-like equations and predicts the spatial and temperature variations of the superconducting electrons near T_c. The theory includes a GL coherence length, $\xi(T)$, which is consistent with London's ξ_0 for pure superconductors at $T \ll T_c$, but which diverges at T_c as phase fluctuations set in near the transition.

They also define a quantity, now called the GL parameter, given by

$$\kappa = \frac{\lambda}{\xi}, \qquad (2.4)$$

which determines the nature of the screening currents in the material. If $\lambda \ll \xi$ in the material, then it is classified as a Type I superconductor. This is the typical case for pure metallic superconductors. In this case, introducing flux penetration into the material, which breaks up the superconductor into superconducting and normal regions, increases the free energy of the system. Thus, a single superconducting domain in this case is energetically favorable. Materials for which $\lambda \gtrsim \xi$ are classified as Type II superconductors. This is typical for many alloys and compounds including unconventional superconductors. In this case, domain walls carry a negative surface energy, encouraging the formation of many domains of normal and superconducting regions. There still exists an upper critical field (now called H_{c2}), which completely destroys superconductivity. However, there also exists a lower critical field, H_{c1}, above which scattered normal regions exist throughout the superconductor within vortices of electric current. These vortices inside the bulk of the superconductor carry single quantum of magnetic flux.

Microscopic Theory

Early evidence of an absence of thermoelectric effects [7], suggested an energy gap, Δ, of order k_BT_c in the quasiparticle excitation spectrum. Further evidence for a gap in the quasiparticle spectrum was seen in specific heat measurements [8], which showed an exponential dependence in the electronic specific heat in the superconducting state, rather than the normal state linear behavior. The following year, electromagnetic absorption measurements [9] in the far-infrared region showed a value for Δ of three to four times k_BT_c. A comparison of this value to the minimum excitation energy per particle derived from the specific heat measurements of ~1.5 k_BT_c, gave evidence that excitations were created in pairs.

In 1957, Bardeen, Cooper, and Schrieffer (BCS) [10] incorporated this knowledge with earlier results from Maxwell [11] and Reynolds *et al.* [12], which showed that the T_c of a superconductor depends on the isotopic mass of the constituent element, to develop the microscopy theory superconductivity. They demonstrated that, given an attractive interaction such as the one provided by phonons, electrons are unstable to the formation of pairs of opposite momenta and spin. These Cooper pairs allow electrons, which are fermions, to form a bosonic state and condense into the bose-condensate-like, many-body state that characterizes superconductivity. This means that all electrons in the condensate are described by a single quantum-mechanical wavefunction. This wavefunction plays the same role as the GL order parameter (ψ), and determines the energy gap (Δ) measured in the quasi-particle density of states (DoS). This work won them the Nobel Prize in Physics in 1972.

The following year's Prize was given to Giaever [13], who used planar tunneling into lead to provide unambiguous proof that the BCS theory correctly described the microscopic mechanism of conventional superconductivity. Further tunneling studies at lower temperature [14] revealed fine structure in the tunneling spectrum outside the gap in Mg/MgO/Pb tunnel junctions. This structure, which was due to phonons in the superconducting lead counter electrode, [15] provided solid evidence that the attractive interaction necessary for Cooper pairing was caused by the electron-phonon interaction. Finer structure still was detected by Rowell *et al.* using senstive measurements of the first and second derivative of the current-voltage characteristics of lead-based junctions [16]. McMillan and Rowell then developed an interative computer program that employed the Eliashberg gap equation to calculate the electron-phonon coupling using this sensitive tunneling data [17]. In doing so, they showed that by using tunneling spectroscopy, measurements in the superconducting state are powerful probes of normal state properties, as well as of the superconductor.

Background on Tunneling

Planar tunnel junctions consist of two electrodes separated by a nano-thin insulator, which acts as potential barrier. If both of the electrodes are normal metals, the tunneling probability is, to a first approximation, independent of the applied bias and is proportional to [18]

$$|T|^2 \propto \exp\left\{ -2\int_0^d \sqrt{\left(\frac{2m}{\hbar^2}\right)[U(x,V)-E_x]dx} \right\}. \tag{2.5}$$

In the case of a square barrier (i.e., U independent of x and V, or $\Delta U = 0$, as defined in Figure 2.1), the probability of a quasiparticle tunneling through the insulating barrier falls exponentially with increasing barrier thickness d. Employing Fermi's golden rule, the tunneling current is written as

$$I(V) = I_{1\to 2} - I_{2\to 1} = C|T|^2 \int_{-\infty}^{\infty} N_1(E)N_2(E+eV)[f(E)-f(E+eV)]dE, \tag{2.6}$$

where $N_1(E)$ is the density of quasiparticle states for electrode 1, C is a constant of proportionality and $f(E)$ is the Fermi-Dirac distribution function. If both electrodes are normal metals and $eV << E_f$, then $N(E) = N(E_f)$. Obtaining the bias from the Fermi energy (i.e., $E_F \equiv 0$), we are left with:

$$\begin{aligned} I(V) &= C|T|^2 N_1(0)N_2(0)\int_{-\infty}^{\infty}[f(E)-f(E+eV)]dE \\ &= C|T|^2 N_1(0)N_2(0)V = G_{nn}V \end{aligned} \tag{2.7}$$

Thus, for two normal metals, we recover Ohm’s law and can see that for an arbitrarily small voltage, current will flow across the junction. The conductance, *i.e.*, the derivative of $I(V)$ with respect to V, is in this case a constant, i.e., $G(V) = dI/dV = G_{nn}$.

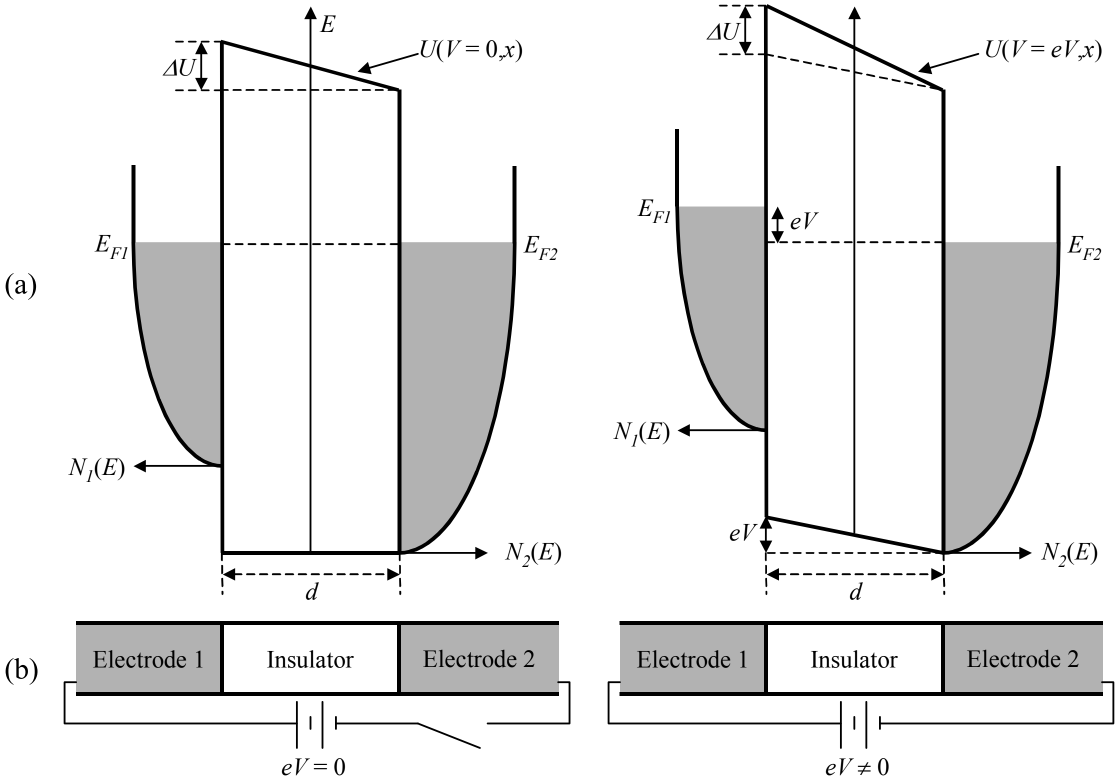

Figure 2.1. (a) Voltage space representation and (b) physical configuration of a tunneling junction, with no applied voltage (left) and applied voltage (right)

Brinkman, Dynes and Rowell [19] showed that for a trapezoidal barrier ($\Delta U \neq 0$ in Figure 2.1), the conductance has the form,

$$\frac{G(V)}{G(0)} = 1 + A(eV) + B(eV)^2 \text{, where} \tag{2.8}$$

$$\begin{aligned} A &= \frac{\Delta U (2m)^{1/2} d}{12 \hbar U^{3/2}} \\ B &= \frac{m d^2}{4 \hbar^2 U} \end{aligned} \tag{2.9}$$

Thus, if the voltage dependence of the barrier is considered, the background is no longer constant but is parabolic.

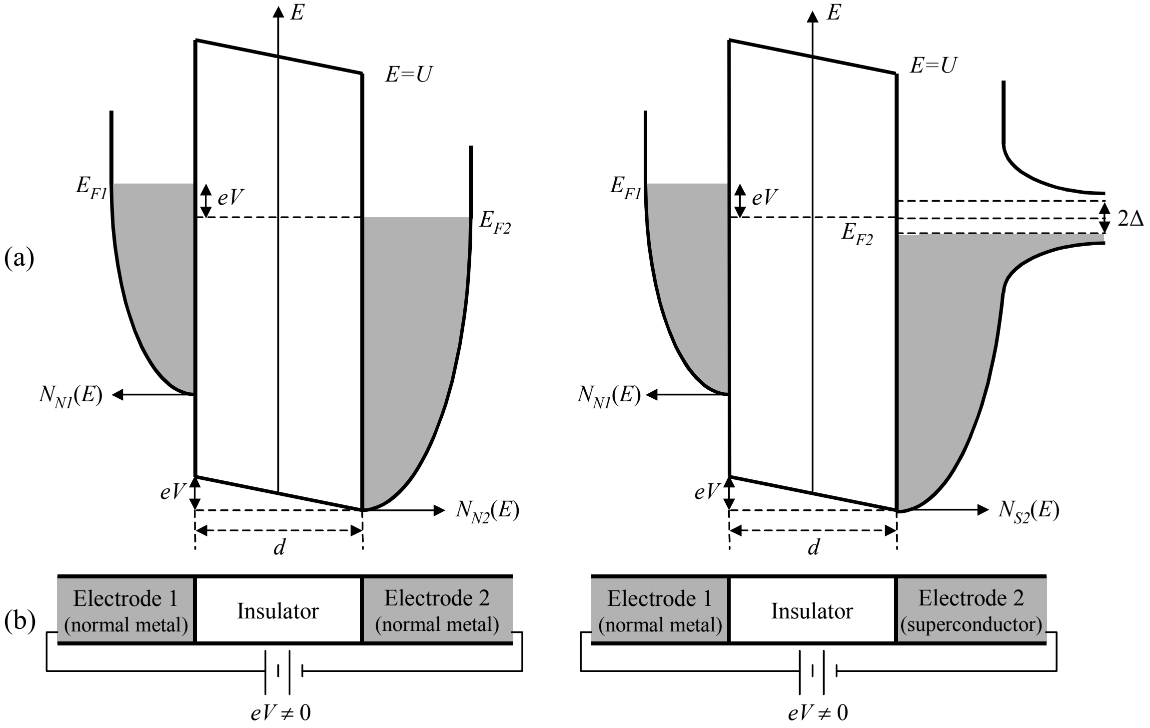

Figure 2.2. (a) Voltage space representation and (b) physical configuration of a tunneling junction, for two normal metal counter electrodes (left) and for one electrode in the superconducting state (right).

If electrode 2 is replaced with a superconductor, the current and conductance are then written as,

$$I_{ns}(V) = \frac{G_{nn}}{e}\int_{-\infty}^{\infty}\frac{N_{2s}(E)}{N_2(0)}[f(E) - f(E+eV)]dE$$

and

$$G_{ns}(V) = \frac{dI_{ns}(V)}{dV} = G_{nn}\int_{-\infty}^{\infty}\frac{N_{2s}(E)}{N_2(0)}\left[-\frac{\partial f(E+eV,T)}{\partial(eV)}\right]dE, \tag{2.10}$$

Thus, tunneling is a direct probe of the superconducting DoS. At $T = 0$, the derivative of the Fermi population function is a delta function, so that to a good approximation at low temperature, the conductance gets us to within a multiplicative constant $[G_{nn}/N_2(0)]$ of the superconducting density of states [$N_{2s}(E)$]. Due to the presence of the 2Δ gap centered around the Fermi energy, no current will flow in the superconducting junction for $|eV| < \Delta$. The states lost inside 2Δ, consequently, are conserved immediately outside the gap, and form the "coherence peaks", which are measured at +Δ and –Δ, as shown in Figure 2.3.

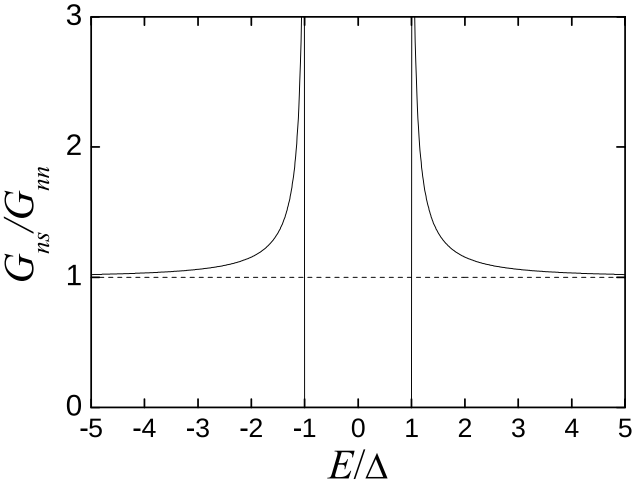

Figure 2.3. Simulation of the tunneling conductance of a BCS *s*-wave superconductor at T=0, which shows the DoS. The dashed line indicates the normal state conductance and the solid line shows deviations from the normal state when one electrode is a superconductor.

In addition to providing a direct probe of the superconducucting DoS, planar tunneling provides a mechanically stable configuration with which the dependence on temperature, magnetic field, and field orientation can be measured on a single junction. Though point-contact spectroscopy and scanning tunneling spectroscopy (STS) can provide high spatial resolution, the junction configuration is perturbed by mechanical disturbances in the system caused by changing temperature, magnetic field, etc. Thus, obtaining these dependencies is extremely difficult using point-contact or STS measurements.

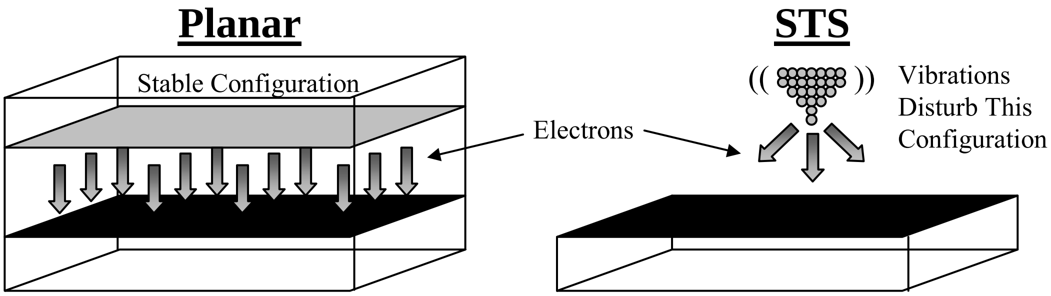

Figure 2.4. Schematic illustration of the physical configuration for planar junctions vs. STS or point contact junctions. Planar junctions provide a mechanically stable configuration compared to STS or point-contact spectroscopy.

There are useful electron spectroscopy techniques other than tunneling. Two important optical techniques include angle-resolved photoemission spectroscopy (ARPES) and infrared (IR) reflectance/absorption measurements. Each has specific advantages and provides complementary information to tunneling measurements. ARPES employs the photoelectric effect by injecting photons of known energy and detecting the momentum (magnitude and direction) of the emitted electrons. In this way, the density of electron states in materials is measured. The power of this technique is that it is angle-resolved, with angular resolution of 0.2° [20]. This means that the orientational anisotropy of YBCO can be explored. The main drawback compared to tunneling spectroscopy is the energy resolution of the present detector technology (~2 meV [20]). In contrast, tunneling is limited only by the width of the derivative of the fermi occupation function or $\sim k_BT$, which, at 1.5 K for example, is 0.13 meV. Also, ARPES is more sensitive to surface quality than tunneling. Whereas tunneling probes only within a coherence length of the surface ($\xi_{ab}\sim 2$ nm), the ARPES measurement depth, which is determined by the energy of the photons used for the measurement, is typically ~0.5 nm [20].

An advantage of IR spectroscopy techniques is that the region probed extends much deeper into the sample than either tunneling or ARPES, making surface quality less important for these measurements. However, low carrier concentrations in cuprate materials (which make λ large) and small values for ξ_0, place cuprates in the "clean limit" [21] ($\xi_0 < \ell < \lambda$, where ℓ is the electronic mean-free path) . In this regime, the Drude peak at low frequency in the frequency-dependent conductivity is narrower, making it more difficult to measure loss in spectral weight due to the superconducting gap. More fundamentally, infrared reflectivity measures the complex dielectric function and Drude model, which is typically obeyed for low-T_c superconductors, does not describe the behavior observed in YBCO. Since the mechanism for high-T_c is not known, the relationship to the electron DoS is not well understood and the data are difficult to interpret.

2.2 High-Temperature Superconductors

In 1986 by Bednorz and Mueller [22] discovered superconductivity at the unprecedented temperature of 35K in the La:Ba:Cu:O system. This, along with the subsequent discovery by Wu *et al.* at 92 K – some 15 Kelvin above the boiling point of nitrogen – in $YBa_2Cu_3O_7$ (YBCO) gave the field renewed enthusiasm. Now, 18 years have passed since the discovery of cuprate superconductors, the superconducting mechanism is still a matter of debate. Though BCS theory can make some consistent quantitative predictions about these materials [23], phonon-mediated coupling is too weak to produce superconductivity at temperatures in the high-T_c regime [24].

Interestingly, all of the compounds in this class of materials were found to be layered cuprates. These ceramic materials are anti-ferromagnetic insulators in their most stable configuration (parent compounds) and only become superconductors when doped with atoms that inject additional charge carriers (electrons or holes) into the material. Figure 2.5 shows the behavior of two of these materials, one electron doped, one hole doped as a function of carrier doping and temperature. By convention, compounds with doping values higher than that value which results in the maximum T_c are considered overdoped. Those with doping less than that which produces maximum T_c are underdoped.

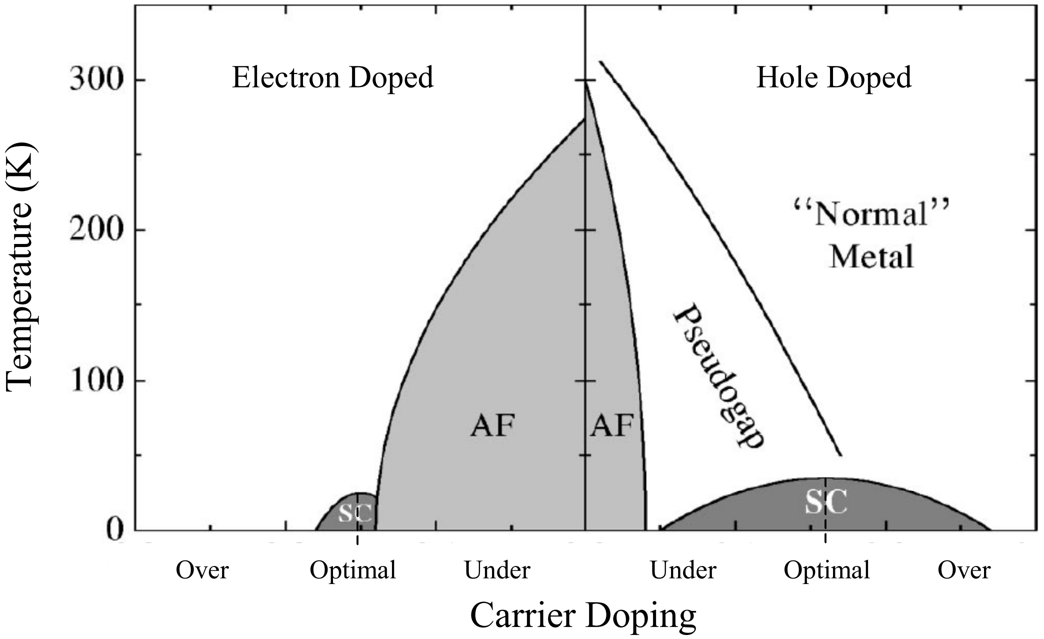

Figure 2.5. Generic phase diagram of electron-doped (left) and hole-doped (right) cuprate superconductors. Typical behavior for high-T_c materials is shown, including antiferromagnetic (AF) parent compounds with limited regions of superconductivity (SC) centered around optimal doping, which is defined as the value of doping that yields maximum T_c. Figure after Ref. [25].

The hole-doped materials typically exhibit non-Fermi-liquid behavior at optimal and underdoping, as a function of temperature, so that even the "normal" state of these materials is not like that of a pure metal. Furthermore, in the underdoped regime, suppression in the density of states centered around zero bias has been measured by many spectroscopic techniques, indicating a “pseudogap” in this vicinity [26]. To determine the microscopic mechanism will likely require a microscopic understanding of the entire phase diagram. Since anti-ferromagnetic backgrounds are present in the parent compounds of many of the high-T_c materials anti-ferromagnetic spin fluctuations are also present throughout the doping range and may play a key role in the pairing mechanism [27].

Although the means of microscopic pairing is unknown, strong support from nuclear magnetic resonance measurements has existed since the early days of high-T_c superconductivity, provided strong support for singlet pairing [28]. Since the total wavefunction must be antisymmetric, this limits the order parameter to a symmetric orbital wavefunction e.g., *s*-wave or *d*-wave [29]. We now know that in contrast to conventional, low-T_c superconductors, which have an isotropic *s*-wave order parameter and associated gap function, Δ, YBCO exhibits *d*-wave symmetry [30, 31]. More specifically, the symmetry is $d_{x^2-y^2}$, which indicates that the lobes of the cloverleaf shaped order parameter (see Figure 2.6) orient themselves in line with the *a*- and *b*-axes of the YBCO unit cell, which is along the Cu-O bond directions [32]. Not only is the magnitude of order parameter anisotropic, having nodes along the (110)-direction (as well as $n\pi/2$ rotations from that direction), the phase of the order parameter changes sign in alternating lobes.

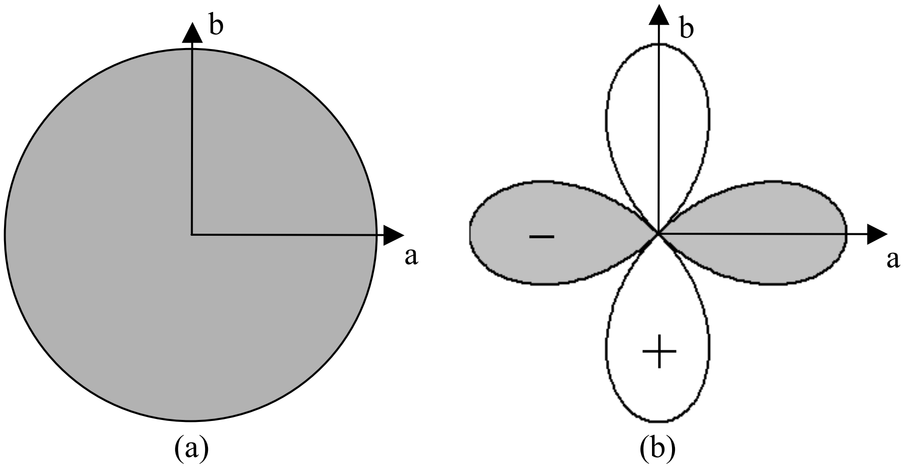

Figure 2.6. Wavevectors ($k–k_f$) associated with the quasiparticle excitations for an *s*- and (a) a *d*-wave (b) superconductor. The enclosed areas represent regions in k-space for which quasiparticle excitations are forbidden, since the quasiparticles associated with these wavevectors are participating in the superconducting condensate.

This configuration of the order parameter leads to many interesting phenomena. The change in sign of the order parameter generates an enhancement of quasiparticle density at the surface of YBCO for certain crystallographic orientations. This quasiparticle surface state, comprised of Andreev bound states (ABS), exhibits specific dependencies on the crystallographic orientation, magnetic field and temperature that can be probed by planar tunneling spectroscopy.

Andreev Bound States

A comparison of a bulk *s*-wave DoS to a bulk *d*-wave DoS reveals differences in the details of the gap region, as shown in Figure 2.7a. Note that both symmetries cause a depression in the DoS inside the gap. Both exhibit coherence peaks at the gap edge and return to the normal state conductance outside the gap. The bulk *d*-wave DoS shows non-zero quasiparticle weight for arbitrarily small bias, due to nodes in the gap function, but qualitative features are similar. The ABS, however, marks a qualitative difference in what is observed in contrast to conventional superconductors. The result of tunneling into a surface containing ABSs, along with the bulk *d*-wave DoS is shown in Figure 2.7b.

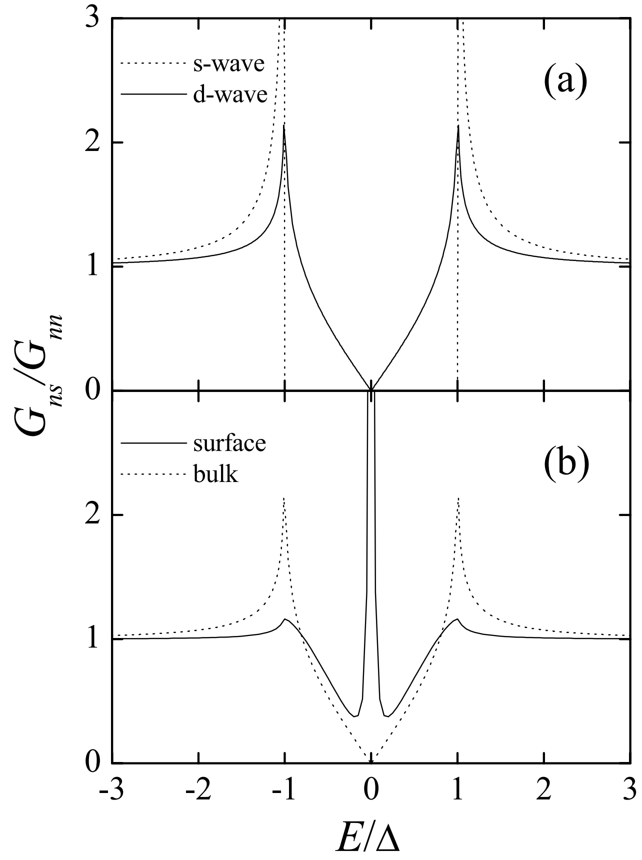

Figure 2.7. **S**imulations (a) showing the difference between BCS *s*-wave DoS (dotted line) and bulk *d*-wave DoS (solid line). Simulations (b) comparing the bulk DoS of a *d*-wave superconductor (dotted line) to the surface DoS (solid line) of the same material if the surface normal is along the nodal direction of the gap function (e.g. YBCO(110)).

That this spectrum is measured at the surface of certain orientations of *d*-wave superconductors is a reflection of the qualitative difference in the functionality of the *d*-wave order parameter compared to *s*-wave, *i.e.*, the phase of the *d*-wave order parameter changes sign for different momentum directions. Thus, Andreev bound state spectroscopy is a phase-sensitive measurement.

To comprehend how an ABS is formed, it is necessary to first understand the process of Andreev reflection. Andreev reflection was introduced as a way to explain a measured increase in thermal resistance for measurements in the intermediate state of superconductors [33, 34]. To explain this increase, it was proposed that additional quasiparticle scattering could occur at the normal metal-superconductor (NS) interfaces in the intermediate state. Since it was assumed that the order parameter is smooth on the order of the Fermi wavelength, however, the process through which such a weak potential could produce such an effect was not understood. Andreev showed that the effect was not classical scattering but electron-hole conversion [35].

Andreev reflection originally was envisioned at a clean NS interface. This process (see Figure 2.8) is one in which a quasiparticle, (consider a quasi-electron) in the normal electrode, with $|E| < \Delta$, is incident on the superconducting electrode. There is no quasi-electron state available in the superconductor so the quasi-electron must pair with another quasi-electron of opposite momentum and spin from the normal metal reservoir to form a Cooper pair. Once the pair is formed, in order to conserve charge, momentum and energy, a quasi-hole is formed with momentum equal but opposite to the momentum of the original quasi-electron. Thus, the quasi-hole travels back along the original path of the incident electron, *i.e.,* it is retroreflected (see Figure 2.8). This results in an enhancement of the conductance inside the gap region to as much as twice the normal state value.

Andreev reflection does not require an NS interface, however. Andreev reflection also occurs at the surface of any *d*-wave superconductor in which the lobe in the order parameter is not perpendicular to a specular surface. Consider the case illustrated in the lower panel of Figure 2.8. In this case, specular reflection at the (110) surface of YBCO results in a change in sign of the superconducting order parameter along the reflected path. If the quasiparticle (e.g., a quasi-electron) has energy less than the gap, this change in sign induces an Andreev reflection, which sends the quasiparticle (which is now a quasi-hole) back to the surface, where it specularly reflects. The process starts over again when the quasi-hole is Andreev reflected back. Thus, the quasiparticle is bound in this periodic motion, as described in Figure 2.8. Since the wavefunctions of the electrons and holes penetrate into the superconductor over a length of the order of the superconducting coherence length, the state is bound within the same length scale [36].

Andreev reflection can occur anywhere within a *d*-wave superconductor, and as long as there is a sign change in the order parameter along the quasiparticle trajectory, and the scattering center is in the unitary limit, the result will be a bound state at the Fermi energy. However, Andreev reflection at the surface is a special case for two reasons. First, since the surface is always in the unitary limit, the unperturbed surface ABS always resides at the Fermi energy. This is zero bias in our tunneling conductance measurements. Second, the translational invariance of the surface leads to the existence of the ABS over a macroscopic distance, enabling its detection by planar tunneling. Thus, for a *d*-wave superconductor having the nodal direction oriented normal to the surface, there exist excess zero-bias quasiparticle states only within a coherence length of the surface. Since tunneling only measures this region, the ABS is a dominant feature in tunneling measurements into *ab*-oriented YBCO films.

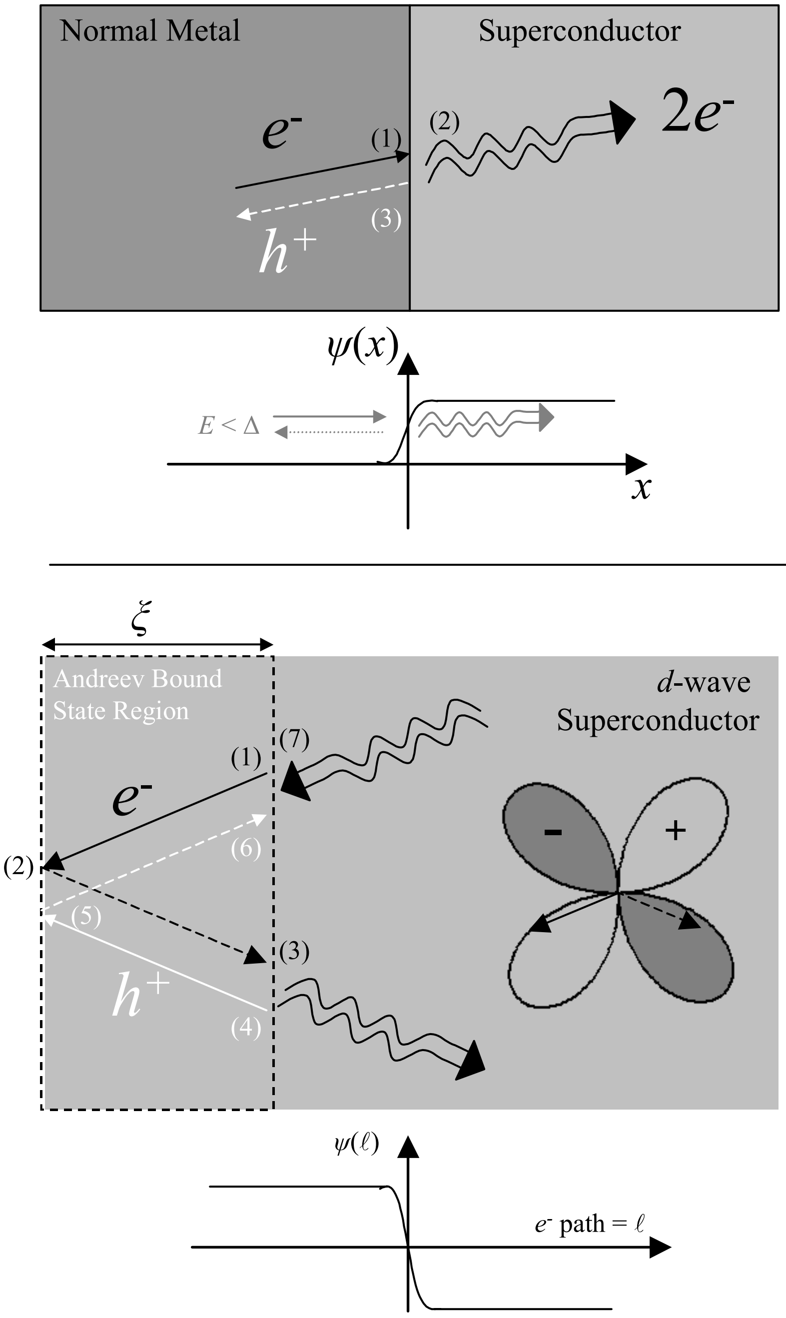

Andreev Reflection:

(1) Quasi-e^- incident on N/S interface with E < Δ.
(2) Quasi-e^- pairs with another quasi-e^- from normal metal reservoir with opposite velocity and spin to form a cooper pair.
(3) This results in a quasi-h^+ that travels with velocity opposite to the original quasi-e^-.

Andreev Bound State Periodic Motion:

(1) Quasi-e^- with E < Δ incident on the surface of a *d*-wave superconductor (node normal to surface).
(2) Quasi-e^- specularly reflects, experiences sign-change of the order parameter, $\psi(\ell)$.
(3) Quasi-e^- undergoes Andreev reflection, cooper pair travels along quasi-e^- path.
(4) Quasi-h^+ returns with opposite velocity along quasi-e^- path.
(5) Quasi-h^+ specularly reflects, experiences sign-change of the order parameter, $\psi(\ell)$.
(6) Quasi-h^+ undergoes Andreev reflection, cooper pair travels along quasi-e^- path.
(7) Periodic motion begins over.

Figure 2.8. Illustration of Andreev reflection at a normal-metal/superconductor interface (top) and at the surface of a *d*-wave superconductor (bottom), which leads to the formation of an Andreev bound state (enclosed by a dotted line) within ξ of the surface through the execution of the periodic motion described here.

This state can be shifted away from zero bias, however. This occurs if a supercurrent is present at the superconducting surface, as in the case of a Meissner screening current induced by a magnetic field. In this case, the supercurrent carries a net momentum, so that the Cooper pairs no longer have opposite (i.e. time-reversed) momenta $[k, -k]$, but now have momenta $[k + s, -k + s]$, where the momentum per Cooper pair is given by $p_s = 2\hbar s$. Thus, when the Andreev reflection leg of the ABS trajectory is completed, the retro-reflected hole no longer travels along the original path, but now carries additional momentum of $2s$ in the direction of the supercurrent. In this manner, the quasiparticles are "dragged along" with the supercurrent. This coupling only occurs if the quasiparticle momentum has a component of the trajectory along the direction of the supercurrent. Since only Fermi energy quasiparticles participate in the ABS, the energy shift due to this coupling is given by $\varepsilon = \pm v_F \bullet p_s$, where, as it is a Doppler shift, the plus sign corresponds to quasiparticles moving along the supercurrent direction and the minus sign to quasiparticles moving counter. This splitting of the ABS in applied field has been observed in many works [37-42], and has been observed to occur in decreasing temperature without applied field [39, 41, 43-46]. This spontaneous splitting has been attributed to the possible existence of a sub-dominant superconducting order parameter at the surface of YBCO [47].

Tunneling in YBCO: Early Techniques and Results

Fabricating high quality tunneling junctions has proven to be more of a challenge on high temperature superconductors (HTS) than on metallic superconductors. According to BCS theory, the coherence length is related to other material parameters according to the expression [4]

$$\xi_0 = \frac{\hbar v_F}{\pi \Delta(0)}. \tag{2.11}$$

This is consistent with Pippard's expression (Equation 2.3) since in BCS theory, $\Delta(0) = 1.74\ k_B T_c$.

For low temperature superconductors, this characteristic size of the Cooper pair can be hundreds of nanometers. Since tunneling probes superconductors on the order of the coherence length [36, 48], it constitutes a bulk measurement for these materials. In YBCO, the value of v_F is an order of magnitude lower than for most simple metals while the value of $\Delta(0)$ is an order of magnitude higher, resulting in a coherence length that is substantially shorter, on the order of a few nanometers or less. In YBCO, for example, $\xi_{ab} \sim 2$ nm and $\xi_c \sim 0.3$ nm [49, 50]. Hence, for YBCO, tunneling is a highly surface-sensitive probe.

Because of this sensitivity, the surface of the YBCO sample must be an accurate representation of the bulk material if one hopes to obtain bulk information. The complex perovskite structure of YBCO makes this a challenge from the outset. Further complicating the situation is that the YBCO surface is susceptible to oxygen loss [51]. Since electron holes arising from oxygen doping are the native charge carriers in YBCO, great care must be taken to keep the surface fully oxygenated. In addition, because of the *d*-wave symmetry, the tunneling results depend on the orientation of the YBCO surface. Rotation of the crystal by 45 degrees, e.g., measurements on the (100) and (110) surfaces, changes the effect of the order parameter on specularly reflecting quasiparticles at the surface. This determines whether the ABS is expected to form, as mentioned above.

Evidently, tunneling in YBCO presents many challenges relative to conventional superconductors. The first attempts at measuring the superconducting gap in YBCO avoided tunneling entirely and used clean metallic contacts [52]. As mentioned previously, Andreev reflection at NS interfaces results in enhanced conductance within the gap region. Thus, the value of the energy gap can be determined by making spectroscopy measurements in this enhanced conductance region. However, in Andreev reflection spectroscopy, it is difficult to measure the full DoS, and tunneling was used in order to gain more information. Planar junctions are stable in their physical configuration allowing checks of reproducibility, temperature and magnetic field dependencies. Furthermore, they can provide momentum resolution and thus proved well-suited for these studies.

As early as April 1987, Iguchi and coworkers [53] measured planar tunnel junctions using Pb counter-electrodes on a sintered sample of YBCO. They observed a multi-peak structure with the first peaks assigned as the gap at ± 21 meV and additional structure at the harmonics 42 meV and 62 meV. The first report of an all thin-film structure was made by Blamine *et al.* [54] in July of that same year. Their YBCO/YO_x/YBCO/Nb multilayers yielded curvature in the I-V characteristics corresponding to a depression in the conductance at approximately ± 35 meV. Then in July of 1988, Benacka *et al.* [55] reported on co-deposited YBCO thin films with native tunneling barriers formed by reaction with Pb counter-electrodes. Although their YBCO films had broad zero-resistance transitions (width of 10–20 K) suggesting that the quality of the YBCO films was poor, their use of a native barrier formed by oxidized Pb and oxygen-deficient YBCO would be widely used in the future.

One month later, Fournel *et al.* [56] reported on using this method of barrier formation on single crystals. They prepared YBCO single-crystal surfaces by cleaving them along the *ab*-planes. This exposed the c-axis surface, on which they deposited Pb counter-electrodes. They were the first to show what would become the signature of c-axis tunneling into YBCO. Their features included a conductance background that increased outside the gap region, a zero-bias conductance dip and a gap-like-feature at ~19 meV. In addition, their tunneling characteristics measured below the T_c of Pb revealed the same Pb phonon structure indicating single-step elastic tunneling across the barrier.

Geerk *et al.* [57] reproduced these features by using Pb counter-electrodes on higher quality YBCO thin films. Gurvitch *et al.* measured tunneling on YBCO single crystals and created a cleaner c-axis surface through a process of chemical etching before deposition of the Pb counter-electrodes [58]. Their results were also consistent with those of Fournel *et al.* After this series of results, the YBCO/Pb tunnel junction configuration became a standard in the industry for planar tunneling devices.

Several other junction fabrication techniques using artificial barriers were also attempted during this time. A notable example is work done by Iguchi and Wen [59], who used electron-beam deposited MgO, AlO_x, and Y_2O_3 as the tunneling barrier, all with Pb counter-electrodes. In comparison to the YBCO/Pb junctions, these methods yielded similar results: broadened YBCO and Pb gap characteristics. Some differences were noted between the different barriers: Pb phonons were observed in the DoS, strongly for the native oxide, weakly for the MgO insulator and not at all for AlO_x and Y_2O_3. This relative success of the native oxide, as well as its reliability and simplicity, established the native oxide technique as the industry standard for planar junction fabrication on YBCO.

Other tunneling methods such as STS have been employed successfully, but using STS sets limits on the dependencies one is able to study, as mentioned in Section 2.1. Still, some authors [60] employed this technique to detect the anisotropy of superconductivity in YBCO; the hallmark of this anisotropy being the presence of a zero-bias conductance peak (ZBCP) at the YBCO (110) surface and its absence at the YBCO (100) surface. Recently, Wang *et al.* [61] have utilized ramp edge junctions to define the direction of tunneling into the *ab*-planes and have been successful in measuring this same asymmetry, showing the continuous suppression of the ZBCP as one moves from tunneling in the [110] direction to [100]. Nonetheless, this method produces broadened features likely due to the disordered surfaces since the ramp-edge surfaces are prepared by Ar ion milling [62].

Measurements into *ab*-oriented YBCO thin films and single crystals [including (103)- and (100)-oriented samples] consistently show a zero-bias conductance peak (ZBCP). As discussed previously, this feature is expected for the (110)-oriented YBCO surface, but this was not known when the early measurements were made. Even after evidence began to surface that *d*-wave was the likely order parameter symmetry for YBCO and the prediction was made for the ZBCP [63], it was not clear that the ZBCP was caused by the ABS. There are many mechanisms that can produce a ZBCP (e.g., magnetic [64, 65] and/or Kondo scattering [66], proximity effects [67], Josephson currents [68], shorts in the barrier, Cooper-pair or reflectionless tunneling, inelastic processes, etc.) so extensive diagnostics were necessary to prove that the observed feature was indeed the ABS.

An extensive body of work amassed that studied the magnitude of the magnetic field [38-40, 43, 45, 61, 69-72], crystallographic orientation [37, 42, 44, 45, 61, 72, 73], impurity doping [74, 75], calcium (carrier) doping [40, 71, 72, 76], and temperature [38, 39, 43-45, 69] dependence of this feature. One was not able to state unequivocally, however, that the ZBCP was indeed composed of ABS until FRS made their prediction [47], as described previously, regarding the dependence of the splitting of the ABS with magnetic field. Once the dependence on the magnitude [43] and orientation [38, 39, 72] were verified, it became clear that the ABS interpretation was correct. The vast majority of tunneling measurements on YBCO, with few exceptions [42, 43, 77, 78], have employed the formation of native oxide barriers at the YBCO thin film-counter electrode interface. In each case listed above, the counter electrodes are composed of either lead or indium.

Exceptions include the present work and the work of Covington *et al*. [43], which employed chemical modification of the surface to form an insulating barrier. This allowed the use of a counter electrode other than lead and indium, both of which superconduct at low temperature. Thus, low temperature measurements at low bias and zero field measurements are masked by the counter-electrode superconducting DoS. Using copper counter electrodes, Covington *et al.* showed that a splitting observed in the ZBCP at low temperature is also present in the absence of a magnetic field, consistent with spontaneously broken time-reversal symmetry (BTRS).

2.3 Planar Junction Fabrication Methods

The native oxide technique is the most common technique for fabrication tunnel junctions on the surface of YBCO thin films and single crystals [37-40, 44, 53, 55-59, 61, 69-76, 79]. Though we've used this reliable technique extensively in our laboratory, native oxides present significant problems. The first problem is the nature of the formation of the tunneling barrier in this technique. Plecenik *et al.* confirmed [80] that for lead counter electrodes, insulator formation is due to oxidation of the lead at the interface. This indicates that oxygen is being removed from the YBCO, affecting the doping at the surface of the film (the region probed by tunneling).

The second problem, as mentioned above, is that both lead and indium become superconductors at low temperatures. Thus, the low-bias conductance features are dominated by the superconducting DoS of the counter electrodes at the lowest temperatures in the absence of a magnetic field above the critical field of the counter-electrode. A bismuth counter-electrode may be used instead of lead or indium, since it superconducts only under high pressure, but the barrier is formed in the same way as for the lead counter-electrodes, so the YBCO is disordered in presumably the same way.

Covington *et al.* avoided the problem of superconducting counter electrodes by using chemical modification of the as grown YBCO surface [43]. This technique required reaction in a solution of 1, 12 diaminododecane in dry acetonitrile acid for 2 ½ days. The intention was to form the insulating barrier using self-assembled monolayers (SAM). However, no correlation between the predicted SAM thickness and junction resistance was found. In addition to the disadvantage of the time investment in this technique, the resulting barrier was largely uncharacterized, with the only means of characterization being the tunneling measurements themselves. In addition, there was evidence from the tunneling measurements that the technique disordered the YBCO surface [43].

We have developed a novel insulator deposition technique that addresses all of the problems mentioned above. A zirconia insulator is deposited by successive condensation and hydrolysis (C-H) reactions between H_2O, diluted with *n*-propanol (Pr^n) and zirconium propoxide [$Zr_4(OPr^n)_{16}$] on the YBCO surface. The experimental details of the technique are discussed in Section 3.2. Here, we describe the chemistry involved.

The molecule, $Zr_4(OPr^n)_{16}$ (see Figure 2.9), is essentially a core of zirconia (ZrO_2) surrounded by loosely-bound propyl alcohol groups.

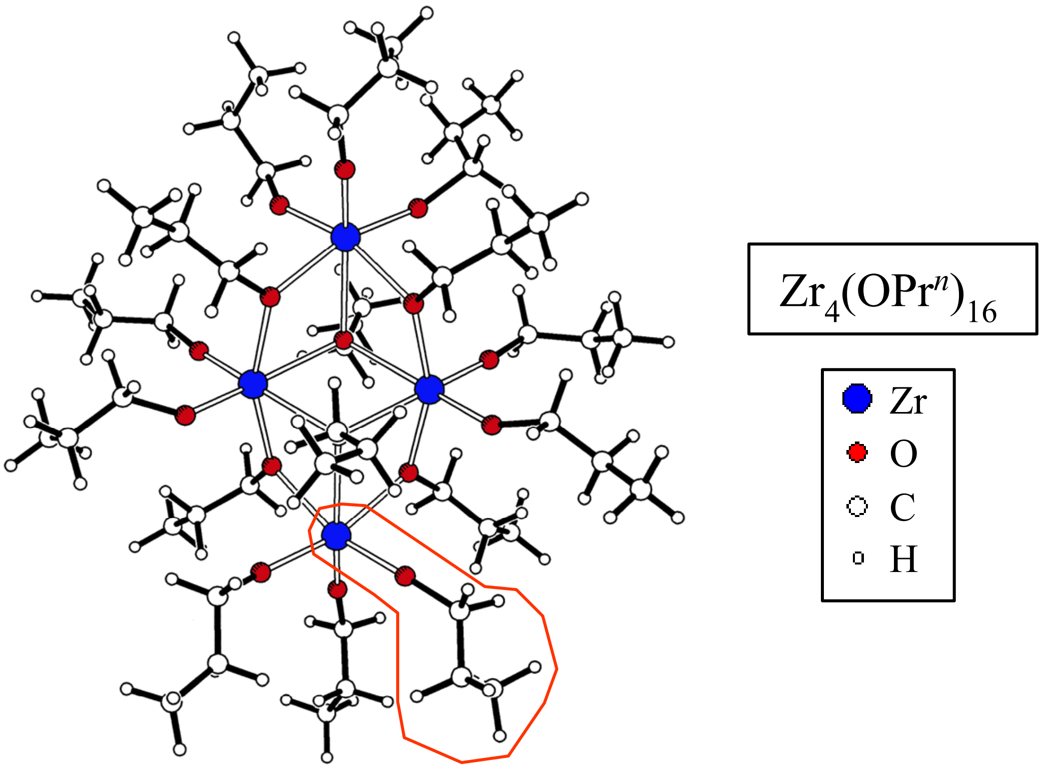

Figure 2.9. Molecular structure of $Zr_4(OPr^n)_{16}$, which is used as a precursor in condensation-hydrolysis reactions to build an insulating layer on the surface of YBCO. The circled region is shown in detail in the next Figure.

Since the C-H process is highly sensitive to moisture, the molecule easily forms large (~100 nm) aggregate molecules if not handled in a dry atmosphere. Thus, if the molecule were used in the reaction directly from the manufacturer, the formation of nano-thin tunneling insulators would be impossible. The $Zr_4(OPr^n)_{16}$ molecule must be isolated in solution, so an extensive purification process has been developed by M. M. Pafford [81]. This process produces precursors composed of individual molecules, allowing us to use the C-H reaction technique to build a sufficiently thin tunneling insulator.

Although the mechanism of the C-H reaction is not understood [82], we imagine the following picture of what might occur in the process, which can be understood if one concentrates on the single zirconium site circled in Figure 2.9. We can see in Figure 2.10 that if an H_2O or other oxide molecule is in proximity with the zirconium site, the loosely-bound propyl group will dissociate from the oxygen. In the case of reaction with H_2O, the propyl group binds with OH, forms Pr^nOH and returns to solution, leaving OH bound to the zirconium. This comprises the hydrolysis step. This configuration is unstable in the presence other hydrolyzed (or unhydrolyzed) zirconium sites on nearby $Zr_4(OPr^n)_{16}$ molecules so that when two such sites come into contact, they combine to form a ZrOZr bond, releasing the H_2O (or Pr^nOH) back into solution. This is the condensation step. The initial hydrolysis step can be facilitated by OH groups and other oxides at the YBCO surface causing the first $Zr_4(OPr^n)_{16}$ molecules to stick to the YBCO. Successive C-H reactions then result in a layered network of zirconia on the YBCO thin film surface.

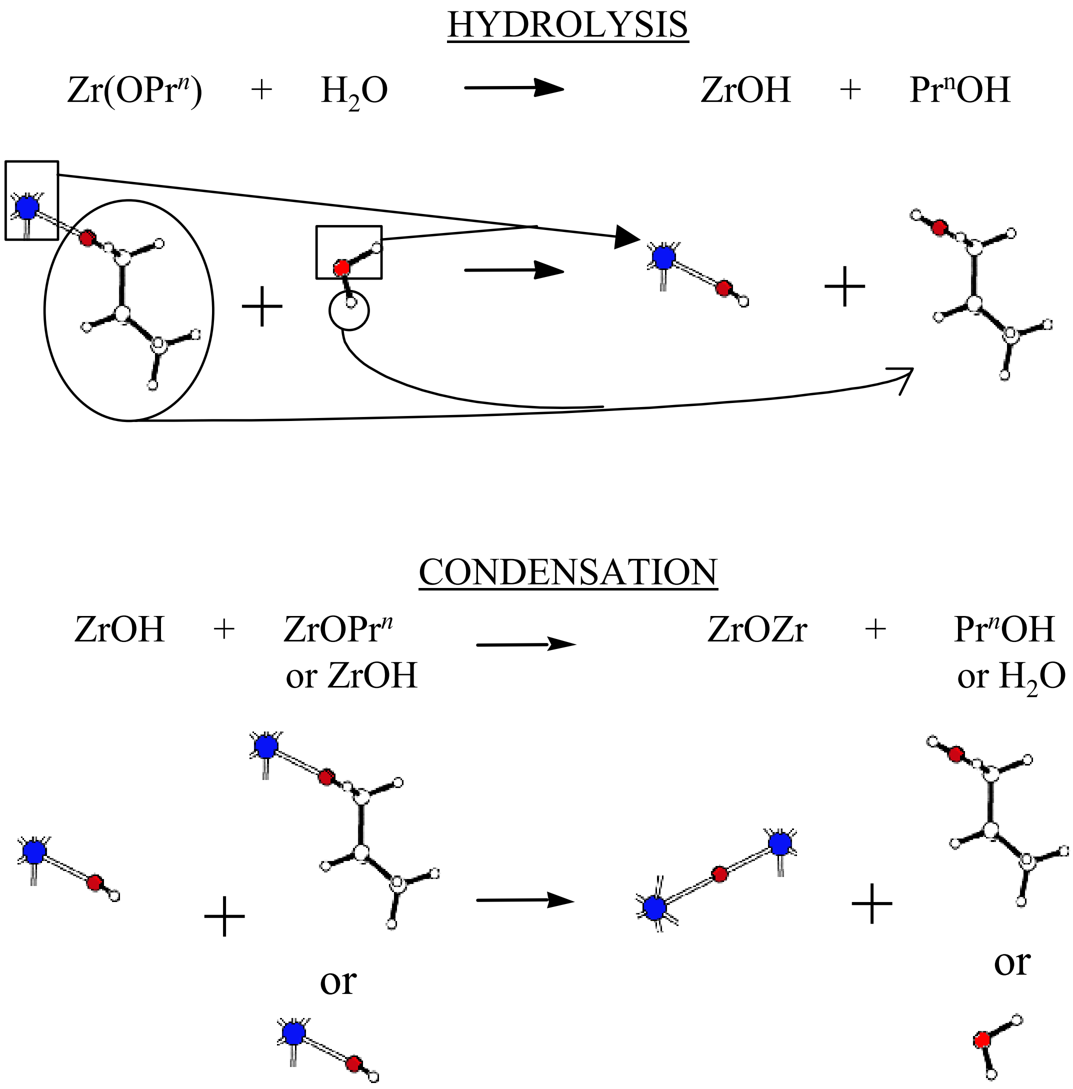

Figure 2.10. Illustration of mechanism for condensation-hydrolysis reactions. This Figure focuses on the single zirconia site circled in the previous Figure.

Within this picture, this novel technique avoids the problems of previous junction fabrication techniques. The artificial barrier allows, in principle, for the deposition of any counter electrode, superconducting or non-superconducting. Though this picture of the reaction depends on the $Zr_4(OPr^n)_{16}$ binding with some oxide species at the YBCO thin film surface, once the first precursors have been deposited, successive precursors need react only with other $Zr_4(OPr^n)_{16}$ molecules to build a barrier so less surface oxygen is lost and any surface damage is minimized. Compared to the chemical modification technique in the work of Covington *et al.*, this deposition process is expeditious (it can be completed in 2–14 hours, depending on the details; see Section 3.2). Finally, the barrier has been well characterized, using x-ray photoelectron spectroscopy (XPS), atomic force microscopy (AFM), and cros*s*-sectional transmission electron microscopy (XTEM) and tunneling spectroscopy as detailed in Section 4.2.

2.4 References

1. H. Kamerlingh-Onnes, Leiden Communications. **122b,** 124c (1911).
2. W. Meissner and R. Oschenfeld, Naturwiss. **21,** 787 (1933).
3. F. London and H. London, Proc. R. Soc. London. **A149,** 71 (1935).
4. M. Tinkham, *Introduction to Superconductivity*. 2nd ed. 1996, New York: McGraw Hill. 94.
5. A.B. Pippard, Proc. R. Soc. London. **A216,** 547 (1953).
6. V.L. Ginzburg and L.D. Landau, Zh. Eksperim. i Teor. Fiz. **20,** 1064 (1950).
7. J.G. Daunt and K. Mendelssohn, Proc. Roy. Soc. London. **A185,** 225 (1946).
8. W.S. Corak, B.B. Goodman, C.B. Satterthwaite, and A. Wexler, Phys. Rev. **96,** 1442 (1954).
9. R.E. Glover and M. Tinkham, Phys. Rev. **108,** 243 (1957).
10. J. Bardeen, L.N. Cooper, and J.R. Schrieffer, Phys. Rev. **108,** 1175 (1957).
11. E. Maxwell, Phys. Rev. **78,** 477 (1950).
12. C.A. Reynolds, B. Serin, W.H. Wright, and L.B. Nesbitt, Phys. Rev. **78,** 487 (1950).
13. I. Giaever, Phys. Rev. Lett. **5,** 147 (1960).
14. I. Giaever, H.R. Hart, and K. Megerle, Phys. Rev. **126,** 941 (1962).
15. J.R. Schrieffer, D.J. Scalapino, and B.J. Wilkens, Phys. Rev. Lett. **10,** 336 (1963).
16. J.M. Rowell, P.W. Anderson, and D.E. Thomas, Phys. Rev. Lett. **10,** 334 (1963).
17. W.L. McMillan and J.M. Rowell, in *Superconductivity*, R.D. Parks, Editor. 1969, Marcel Dekker, Inc.: New York. p. 561.
18. E.L. Wolf, *Principles of Electron Tunneling Spectroscopy*. 1985, New York: Oxford University Press. 21.
19. W.F. Brinkman, R.C. Dynes, and J.M. Rowell, J. Appl. Phys. **41,** 1915 (1970).
20. H. Kamerlingh Onnes, Leiden Communications. **122b,** 124c (1911).
21. D.B. Tanner and T. Timusk, in *Physical Properties of High Tempertaure Superconductors III*, D.M. Ginsberg, Editor. 1992, World Scientific: Singapore. p. 363.
22. J.G. Bednorz and K.A. Mueller, Z. Phys. **B64,** 189 (1986).

23. E. Arrigoni, E. Fradkin, and S.A. Kivelson, Cond-Mat/0309572 (2003).
24. E.W. Carlson, V.J. Emery, S.A. Kivelson, and D. Orgad, in *The Physics of Superconductors*, K.H. Bennemann and J.B. Ketterson, Editors. 2004, Springer-Verlag.
25. A. Damascelli, Z. Hussain, and Z.-X. Shen, Rev. Mod. Phys. **75,** 473 (2003).
26. T. Timusk and B. Statt, Rep. Prog. Phys. **62,** 61 (1999).
27. N.E. Bickers, D.J. Scalapino, and S.R. White, Phys. Rev. Lett. **62,** 961 (1989).
28. S.E. Barrett, D.J. Durand, C.P. Pennington, C.P. Slichter, T.A. Friedmann, J.P. Rice, and D.M. Ginsberg, Phys. Rev. B. **41,** 6283 (1990).
29. S.E. Barrett, J.A. Martindale, D.J. Durand, C.P. Pennington, C.P. Slichter, T.A. Friedmann, J.P. Rice, and D.M. Ginsberg, Phys. Rev. Lett. **66,** 108 (1991).
30. C.C. Tsuei, J.R. Kirtley, C.C. Chi, L.S. Yu-Jahnes, A. Gupta, T. Shaw, J.Z. Sun, and M.B. Ketchen, Phys. Rev. Lett. **73,** 593 (1994).
31. D.A. Wollman, D.J. VanHarlingen, W.C. Lee, D.M. Ginsberg, and A.J. Leggett, Phys. Rev. Lett. **74,** 797 (1995).
32. J.F. Annett, N. Goldenfeld, and A.J. Leggett, in *Physical Properties of High Temperature Superconductors V*, D.M. Ginsberg, Editor. 1996, World Scientific: Singapore. p. 375.
33. K. Mendelssohn and J.L. Olsen, Phys. Rev. **80,** 859 (1950).
34. N. Zavaritsky, Zh. Eksperim. i Teor. Fiz. **38,** 1672 (1960).
35. A.F. Andreev, Sov. Phys. -- JETP. **19,** 1228 (1964).
36. T. Lofwander, V.S. Shumeiko, and G. Wendin, Supercond. Sci. Technol. **14,** R53 (2001).
37. J. Lesueur, L.H. Greene, W.L. Feldmann, and A. Inam, Physica C. **191,** 325 (1992).
38. M. Aprili, E. Badica, and L.H. Greene, Phys. Rev. Lett. **83,** 4630 (1999).
39. R. Krupke and G. Deutscher, Phys. Rev. Lett. **83,** 4634 (1999).
40. Y. Dagan and G. Deutscher, Phys. Rev. Lett. **87,** (2001).
41. H. Aubin, L.H. Greene, S. Jian, and D.G. Hinks, Phys. Rev. Lett. **89,** 177001 (2002).
42. P.J. Hentges, G. Westwood, H. Aubin, W.G. Klemperer, and L.H. Greene, IEEE Trans. Appl. Supercon. **13,** 801 (2003).
43. M. Covington, M. Aprili, E. Paraoanu, L.H. Greene, F. Xu, J. Zhu, and C.A. Mirkin, Phys. Rev. Lett. **79,** 277 (1997).
44. X. Grison, J. Lesueur, M. Aprili, and T. Kontos, Physica B. **284-288,** 559 (2000).
45. P.J. Hentges, L.H. Greene, G. Westwood, and W.G. Klemperer, Physica C. **408-410,** 801 (2004).
46. R. Beck, Y. Dagan, A. Milner, A. Gerber, and G. Deutscher, Phys. Rev. B. **69,** 144506 (2004).
47. M. Fogelstrom, D. Rainer, and J.A. Sauls, Phys. Rev. Lett. **79,** 281 (1997).
48. S. Kashiwaya and Y. Tanaka, Rep. Prog. Phys. **63,** 1641 (2000).
49. D.N. Zheng, A.M. Campbell, J.K. Johnson, J.R. Cooper, F.J. Blunt, A. Porch, and P.A. Freeman, Phys. Rev. B. **49,** 141 (1994).
50. J.R. Waldram, *Superconductivity of Metals and Cuprates*. 1996, London: IOP Puplishing, Ltd. p. 223.

51. L.H. Greene and B.G. Bagley, in *Physical Properties of High Temperature Superconductors II*, D.M. Ginsberg, Editor. 1990, World Scientific: Singapore. p. 509.
52. K.E. Gray, M.E. Hawley, and E.R. Moog, in *Novel Mechanisms of Superconductivity*, S.A. Wolf and K.V. Z., Editors. 1987, Plenum: New York. p. 611.
53. I. Iguchi, H. Watanabe, Y. Kasai, T. Mochiku, A. Sugishita, and E. Yamaka, Jpn. J. Appl. Phys. **26,** L645 (1987).
54. M.G. Blamine, G.W. Morris, R.E. Somekh, and J.E. Evetts, J. Phys. **D20,** 1330 (1987).
55. L. Benacka, V.M. Svistunov, A. Plecenik, S. Chromik, and S. Gazi, Sol. St. Comm. **68,** 753 (1988).
56. A. Fournel, I. Ouija, J.P. Sourbier, H. Noel, J.C. Levet, M. Potel, and P. Gougeon, Europhys. Lett. **6,** 653 (1988).
57. J. Geerk, X.X. Xi, and G. Linkiner, Z. Phys. **73,** 1 (1989).
58. M. Gurvitch, J.M. Valles Jr., A.M. Cucolo, R.C. Dynes, J.P. Garno, L.F. Schneemeyer, and J.V. Waszczak, Phys. Rev. Lett. **63,** 1008 (1989).
59. I. Iguchi and Z. Wen, Physica C. **178,** 1 (1991).
60. L. Alff, H. Takashima, S. Kashiwaya, N. Terada, I. Toshimitsu, O. Kunihiko, K. Masao, and Y. Tanaka, in *Advances in Superonductivity IX*, S. Nakajima and M. Murakami, Editors. 1997, Springer-Verlag: Tokyo. p. 49.
61. W. Wang, M. Yamazaki, K. Lee, and I. Iguchi, Phys. Rev. B. **60,** 4272 (1999).
62. M.B. Walker and P. Pairor, Phys. Rev. B. **60,** 10395 (1999).
63. C.R. Hu, Phys. Rev. Lett. **72,** 1526 (1994).
64. J.A. Applebaum, Phys. Rev. **154,** 633 (1967).
65. L.Y.L. Shen and J.M. Rowell, Phys. Rev. **165,** 566 (1968).
66. E.L. Wolf and D.L. Losee, Phys. Rev. B. **2,** (1970).
67. A. Kastalsky, A.W. Kleinsasser, L.H. Greene, R. Bhat, F.P. Milliken, and J.P. Harbison, Phys. Rev. Lett. **21,** 3026 (1991).
68. C.W.J. Beenakker and H. van Houten, Phys. Rev. Lett. **23,** 3056 (1991).
69. L. Alff, A. Beck, R. Gross, A. Marx, S. Kleefisch, T. Bauch, H. Sato, M. Naito, and G. Koren, Phys. Rev. B. **58,** 11197 (1998).
70. Y. Dagan and G. Deutscher, Phys. Rev. B. **64,** 092509 (2001).
71. Y. Dagan and G. Deutscher, Europhys. Lett. **57,** 444 (2002).
72. G. Deutscher, Y. Dagan, A. Kohen, and R. Krupke, Physica C. **341-348,** 1629 (2000).
73. I. Iguchi, W. Wang, M. Yamazaki, Y. Tanaka, and S. Kashiwaya, Phys. Rev. B. **62,** R6131 (2000).
74. M. Covington and L.H. Greene, Phys. Rev. B. **62,** 12440 (2000).
75. E. Badica, M. Aprili, M. Covington, and L.H. Greene. in *SPIE-Int. Soc. Opt. Eng.* 2000.
76. A. Sharoni, O. Millo, A. Kohen, Y. Dagan, R. Beck, and G. Deutscher, Phys. Rev. B. **65,** 134526 (2002).
77. D. Racah and G. Deutscher, Physica C. **263,** 218 (1996).
78. J. Takada, T. Terashima, Y. Bando, H. Mazaki, K. Iijima, K. Yamato, and K. Hirata, Appl. Phys. Lett. **53,** 2689 (1988).

79. M. Covington, R. Scheurer, K. Bloom, and L.H. Greene, Appl. Phys. Lett. **68,** 1717 (1996).
80. A. Plecenik, S. Benacka, M. Darula, S. Chromik, P. Mikusik, and M. Grajcar, Sol. St. Comm. **78,** 809 (1991).
81. V.W. Day, W.G. Klemperer, and M.M. Pafford, Inorg. Chem. **40,** 5738 (2001).
82. L.H. Greene, P.J. Hentges, W.G. Klemperer, J.-G. Wen, and G. Westwood, J. Mater. Chem. **14,** 1 (2004).

Chapter 3
Experimental Techniques

3.1 YBCO Thin Film Growth

All $YBa_2Cu_3O_{7-\delta}$ thin films are grown by off-axis planar magnetron sputter deposition in a UHV-compatible chamber using stoichiometric targets [1]. The chamber is used exclusively for growing YBCO-based films and related templates to prevent contamination. The targets are purchased commercially with the nominal doping concentrations. The chamber is equipped with two sputtering guns, one containing the stoichiometric YBCO target, the other containing a target of stoichiometric $PrBa_2Cu_3O_7$, (PBCO) which is used to produce a template layer required for growing certain orientations of YBCO, as explained below.

YBCO Crystal Structure

The substrates, which do not exceed 1 cm^2, are anchored to a 2-inch heater block using Ag paste for good thermal conductivity and uniformity. $SrTiO_3$ (STO) substrates are chosen for the small lattice mismatch with YBCO and because STO is chemically inert with YBCO at the growth temperatures. STO has a cubic crystal structure, with a lattice constant of 3.905 Å, while YBCO is orthorhombic at optimum doping with lattice constants of $(a, b, c) = (3.82$ Å, 3.89 Å, 11.68 Å$)$. Thus, the lattice mismatch between YBCO and STO is less than two percent in the a-axis direction and less than 0.5% for b and $c/3$.

STO and YBCO are both examples of the perovskite crystal structure. STO is a classic example in that it’s composition is ABO_3 with A and B each being 2+ ions in a cubic lattice arrangement. YBCO is a modified perovskite, and can be described as three stacked perovskite cells. Deviations from the perovskite structure include a slight orthorhombic *a*:*b* ratio (see Figure 3.1), minor buckling in the CuO_2 planes and missing oxygen atoms at the top and bottom of the unit cell, in the CuO chain layer.

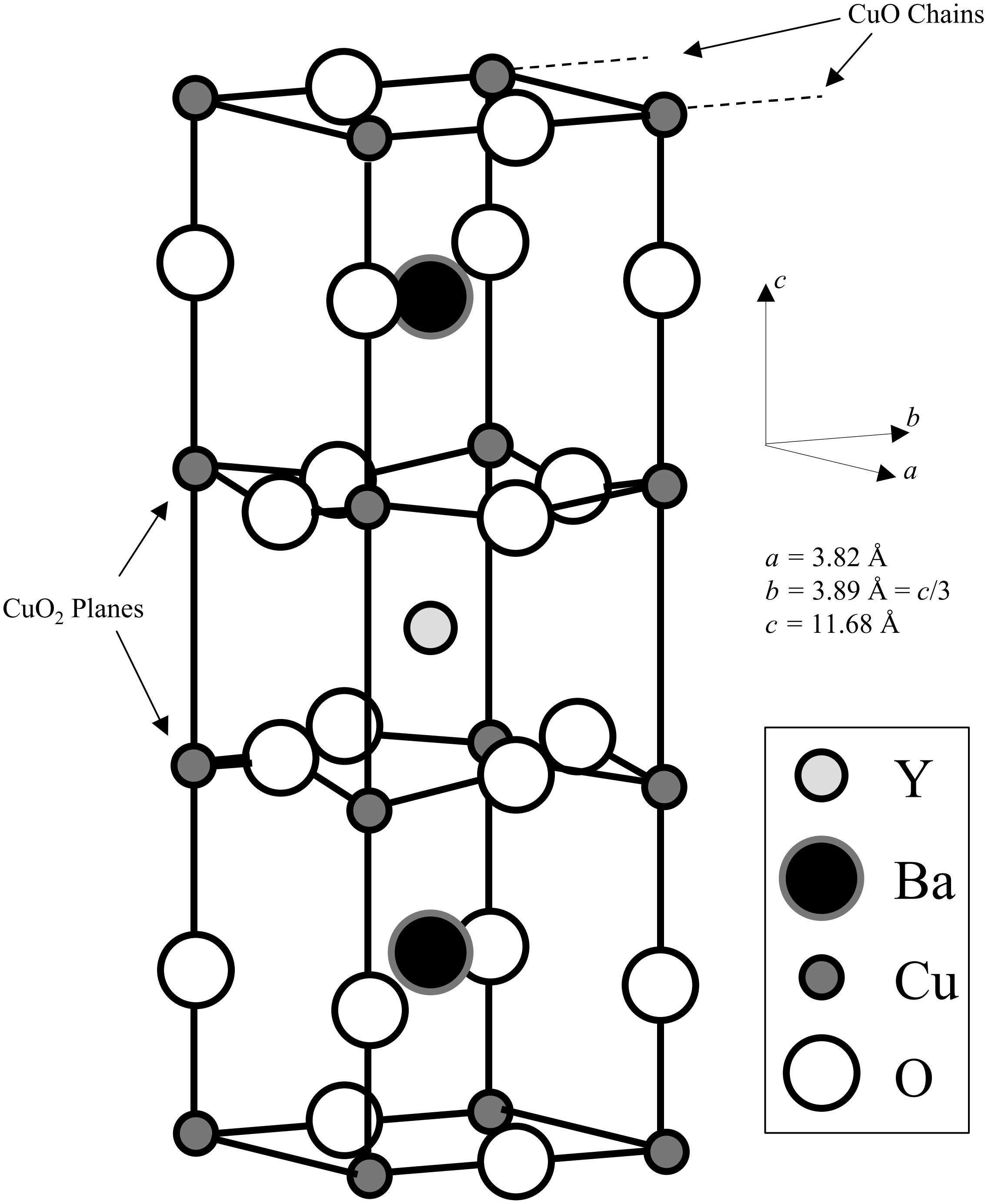

Figure 3.1. Crystal structure of $YBa_2Cu_3O_7$ showing CuO_2 planes and CuO chains. The lattice parameters are also indicated.

This rich crystal structure results in a highly anisotropic electronic structure. Thus, the ability to grow thin films in various orientations is essential if one wants to study anisotropies in electronic structure. We grow YBCO thin films in four crystallographic orientations, by varying the orientation of the substrates, by varying the sputtering parameters and with the use of PBCO template layers. The orientations we grow are the surface parallel orientations of (001) or *c*-axis, (100) or *a*-axis, (103) or *ac*-axis and (110) or *ab*-axis (see Figure 3.2).

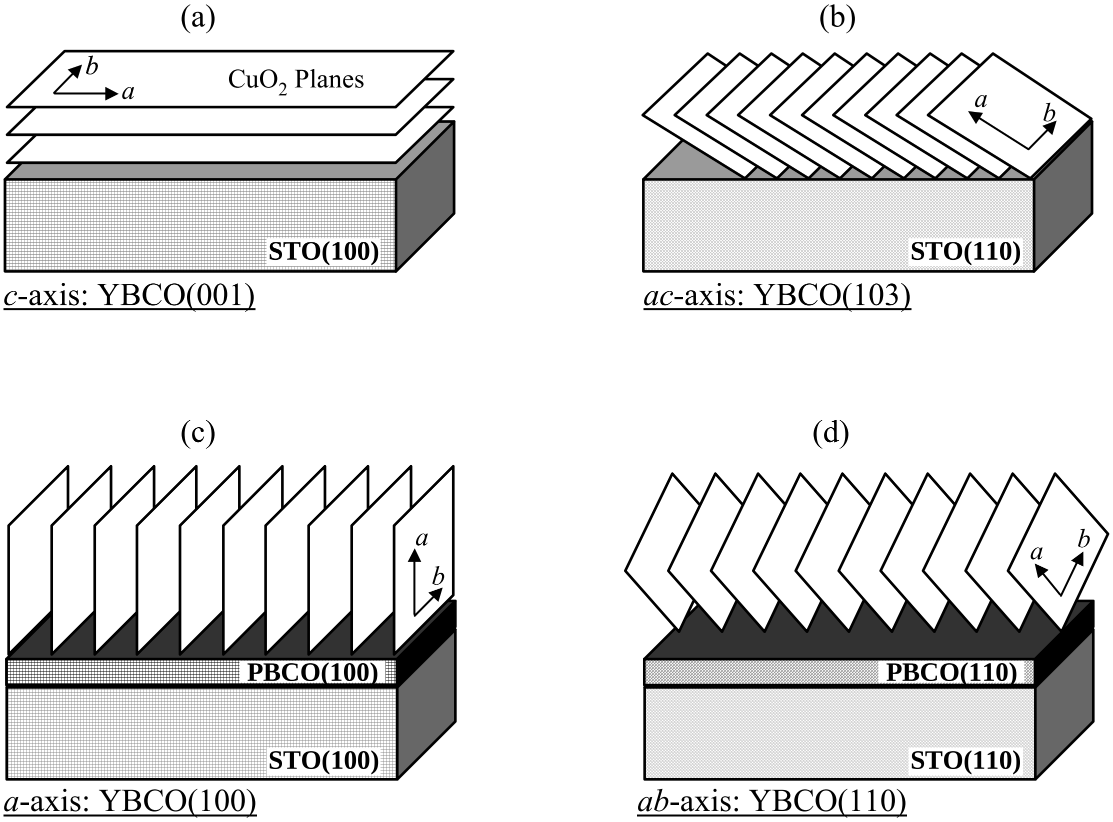

Figure 3.2. Orientation of CuO_2 planes for four crystallographic orientations of YBCO thin films: (a) (001), (b) (103), (c) (100) and (d) (110).

The CuO_2 planes are depicted in the illustrations since these planes are the primary avenues of electronic transport. In the case of *c*-axis films, the CuO_2 planes are parallel to the film surface, making electronic transport along the film most efficient for this orientation. (100)-oriented YBCO exposes the planes normal to the film surface, as does (110)-YBCO, though the planes are rotated 45 degrees relative to (100)-YBCO. For (103)- YBCO, the *a*- and *c*-axes are each at 45° with the surface normal, as are the CuO_2 planes.

Sputtering Basics

Sputtering is a physical process whereby atomic species are ejected into a non-equilibrium gas phase from a solid target material by the bombardment of energetic ions. Argon is used as a sputtering gas because it is plentiful and chemically inert. Oxygen is used in addition to argon to maintain the stoichiometry of YBCO, making this reactive sputtering. The ions are generated by a DC electric field applied between an anode and the target, which acts as a cathode. Sputtering is largely driven by direct momentum exchange between the sputtering ions and atoms in the target. Because it is always the surface atoms that are ejected, sputtering has an important advantage over thermal evaporation as a thin film deposition technique, namely that the composition of the total sputtering plume is roughly the same as the composition of the target [2]. Thus, in principle, if the sticking coefficients of the elements are approximately equal, the resulting film has the same composition as the target [3]. A magnetron sputtering system uses permanent magnets to generate a field normal to the ionizing electric field. This confines the ions to the target surface allowing sputtering rates comparable to a non-magnetron sputter gun with an order of magnitude less power applied to the gun. With this confinement, sputtering non-target materials is also greatly reduced. An additional advantage of sputtering is that for a specified sputter voltage, there is a well-defined sputtering ion energy. This is in contrast to thermal evaporation, which produces a thermal distribution of energies of the evaporated species.

One geometric configuration for sputtering places the substrates directly in line with the sputtered material. This on-axis method results in high deposition rates and is appropriate for single-element sputtering. Though it is expected that sputtering compounds will produce films with the same stoichiometry as the target, this is not the case for HTS materials. There are several sources for potential problems with this configuration. Variations in the sticking coefficients and in the spatial distribution of the different atomic species within the sputtering plasma can result in deviations from the intended stoichiometry in the resulting films. The on-axis configuration presents an additional difficulty for sputtering YBCO, which must be deposited by reactive sputtering in an oxygen atmosphere to produce the proper doping. Since introducing oxygen atoms to the plasma produces negative ions, the oxygen can be "resputtered" into the substrates.

The off-axis sputtering geometry (see Figure 3.3) has been successfully employed to deposit stoichiometric films from a stoichiometric target. This configuration places the plane of the substrates at 90° with the plane of the target. This prevents resputtering of the substrates by removing the substrate from the direct path of the back-sputtered oxygen ions. Though the mechanism for the success of the off-axis configuration is not certain, its implementation reproducibly yields high-quality, stoichiometric films.

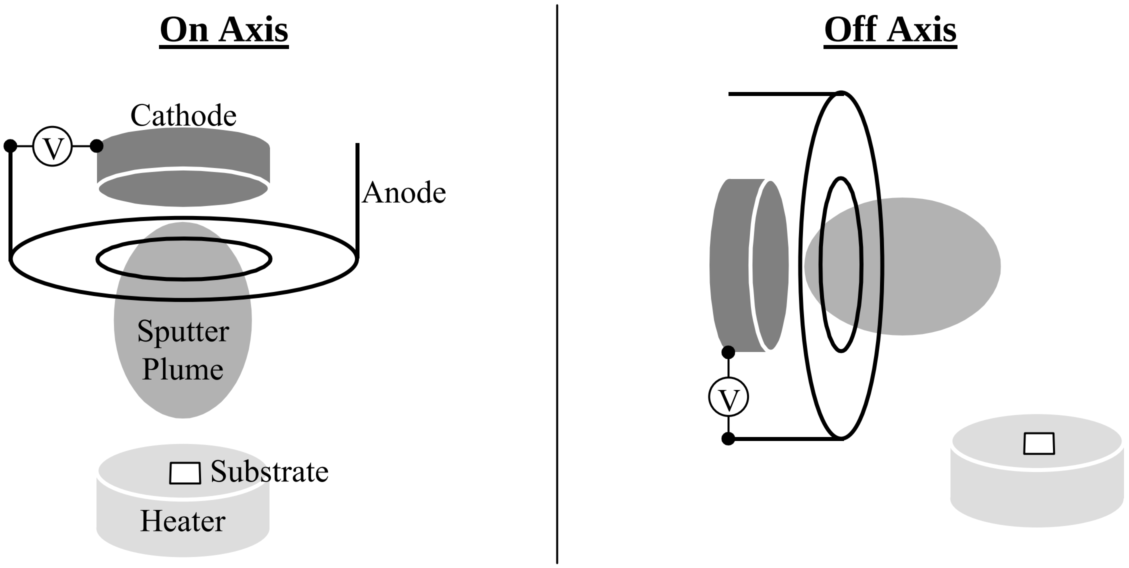

Figure 3.3. Schematic diagram comparing the on-axis to off-axis sputtering geometries. The off-axis geometry has advantages for our applications, as described in the text.

Substrate/Hardware Preparation

The YBCO thin films are grown in a multi-step process. The first step is substrate preparation. In this step, the substrates are cleaned by ultrasonic agitation in a beaker filled with 10 mL of chloroform for 60 seconds to remove any grease or hydrocarbon residue on the surface. After blowing the substrate dry using N_2 gas to remove the chloroform, the second step is ultrasonic agitation in a beaker filled with 10 mL of methanol for 60 seconds to remove any residual chloroform, after which the substrate is again dried under N_2. The third step is to agitate the substrate by hand, holding it with tweezers in a beaker with hot (60–70°C) phosphoric acid for 60 seconds. In the fourth step, the acid is rinsed by placing the substrate under flowing deionized water for 30 seconds and dried with N_2. In the fifth and final step, any remaining moisture residue is removed by another 60 seconds ultrasonic agitation in methanol and the sample is again dried with N_2.

After the substrates have been cleaned, they are mounted onto the surface of the substrate heater, which has been cleaned using a Dremel® rotary tool fitted with a rubberized adhesive polishing tip and then it is wiped down using methanol. The substrates are mounted by coating the back of the substrate with silver paste, centering the substrate on the heater and the pressing on the substrate using a small chip of STO, polished side down, which has also been cleaned to ensure even thermal contact. After the substrate(s) have been mounted, the heater is baked under a heat lamp at 75 ^{o}C for 45 minutes to dry the silver paste.

While the silver paste is drying the cathode bracket that secures the target to the magnetron gun, the anode shield and flexible oxygen tubes are cleaned. These items are etched in a dilute nitric acid bath to remove YBCO buildup from the previous growth. This hardware is etched until all visible traces of YBCO are gone and then rinsed under running tap water. These parts are thoroughly dried by wiping with lint-free cloths, rinsing with methanol and immediately blow-drying with N_2 gas. After the hardware is sufficiently dry and the substrate heater has baked for 45 minutes, the hardware is loaded into the growth chamber and the chamber is pumped to a base pressure of 5×10^{-7} Torr or below. The minimum pumping time is approximately two hours.

Thin Film Growth Process

The YBCO thin films are grown in the vacuum chamber shown in Figure 3.4. Once the base pressure is achieved, argon and oxygen are introduced into the sputtering chamber through flow controllers. The flow controllers are regulated by an MKS gas handler, which keeps the argon and oxygen flowing in a specified ratio and rate. For PBCO growth, the ratio of the flow of argon to oxygen is 5:1 for YBCO growth and 4:3

for PBCO growth, as higher oxygen partial pressure is required for PBCO [4]. The flow rate is 21.0 standard cubic centimeters per minute (SCCM) in both cases. The total system pressure is then regulated by using a butterfly valve to control the pumping rate of a rotary pump. The position of the butterfly valve is controlled by comparing the measured system pressure to the desired value via a PID circuit. The YBCO and PBCO sputter guns are shown in Figure 3.4 with the YBCO gun in the off-axis position. The sputter guns are controlled by a high voltage DC power supply capable of producing the 40–41 W (at 250–270V) required for sputtering. The substrate heater, which is controlled by a separate DC power supply, is shown between the two targets.

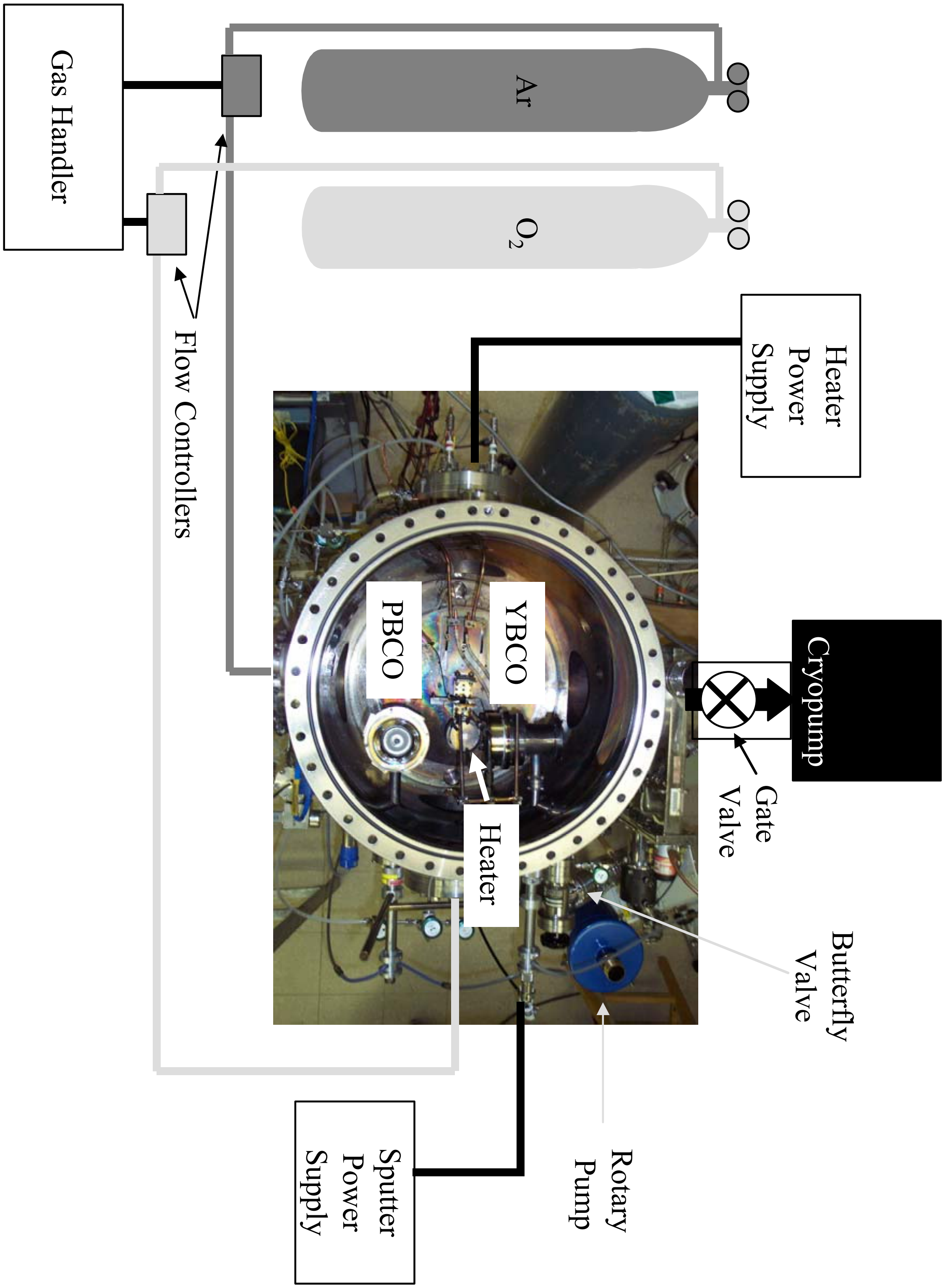

Figure 3.4 Apparatus used for YBCO thin film growth. The process used to fabricate the films is described in the text.

To grow the four different orientations of YBCO, different growth conditions are necessary. The primary control parameters are substrate orientation, substrate temperature, system pressure and the presence or absence of a PBCO template layer. The nominal values for these parameters for each orientation are given in the table below.

Table 3.1. Nominal growth parameters for four orientations of YBCO thin films

YBCO Orientation	STO Orientation	PBCO Template?	Growth T (°C)	System P (mTorr)
(001)	(100)	no	735	170
(103)	(110)	no	735	170
(100)	(100)	yes	700	170
(110)	(110)	yes	730	170

Native orientations for YBCO grown on STO, as can be seen from the table above, are (001)- and (103)-oriented YBCO on (100)- and (110)-oriented STO, respectively, as these can be successfully grown without a PBCO buffer layer. To grow (100)- and (110)-oriented YBCO, some authors [5, 6] have employed a self-template method in which YBCO is first grown at a lower temperature, then after the proper crystal structure has been established, the substrate temperature is increased for the remainder of the growth to ensure higher quality in the bulk film. This technique has the advantage of simplicity but the disadvantage is that the film is left with a sublayer of poor quality YBCO that participates in the electron transport in the film. This is avoided by growing a PBCO layer at a lower temperature (620° C), which acts as a template to seed the proper growth orientation. The PBCO gun is also pointed down 8^{o} from the off-axis position [7]. The entire YBCO thin film is then grown at the higher temperature to achieve higher crystalline quality. The PBCO template does not contribute significantly to electronic transport [8]. The thin film growth rate is approximately 10 nm/hr.

Though the parameters listed in Table 3.1 are the nominal values for high-surface-quality, optimally-doped YBCO, it is sometimes necessary to deviate from these values. One such situation is the case of an aged YBCO target. In this case, the target can become oxygen deficient. Presputtering at a higher oxygen:argon ratio can increase doping back to optimal values [9].

YBCO Thin Film Characterization

Variations in target composition and sputtering environment can cause the resulting films to deviate from acceptable quality. Thus, it is important to constantly monitor the characteristics of the films we grow. As a result, no matter what the intended use of the films produced in a particular growth run, a small analysis film for each orientation included in the run is always grown side-by-side with the other films. These analysis films undergo a battery of analysis techniques intended to probe the bulk and surface quality of the films. Surface analysis techniques include scanning electron microscopy (SEM) and atomic force microscopy (AFM). Bulk film properties are probed by x-ray diffraction (XRD) and resistivity *vs.* temperature (ρ *vs.* T).

SEM provides a relatively quick and easy way to get a sense of the surface quality and uniformity of the YBCO thin film. Coupled with energy-dispersive x-ray spectroscopic (EDS) analysis, SEM becomes a powerful way to identify parasitic oxides at the surface. AFM provides a means for quantifying the vertical scale of features on the surface of the films, which includes the overall roughness and roughness of localized crystalline grains. θ-2θ X-ray diffraction scans provide a verification of bulk crystal structure and texture of the YBCO thin film, the PBCO template layer and the underlying STO substrate. The ρ *vs.* T measurements yield the temperature and width of the superconducting transition. Impurity levels in the film can be inferred from the residual resistivity ratio (RRR) and doping information is apparent from the shape of the ρ *vs.* T curve in the normal state. RRR is defined as the value of the resistivity at room temperature, divided by the value just above T_c, *i.e.*, RRR = $\rho(300\text{ K}) / \rho(100\text{ K})$. Results of these analysis techniques on our YBCO thin films are given in Section 4.1.

3.2 Planar Tunnel Junction Fabrication

Once the YBCO thin film quality is ensured, several techniques for fabricating planar tunnel junctions may be employed, as mentioned in Section 2.3. Here, we focus on the zirconia condensation-hydrolysis (C-H) technique developed in collaboration with Prof. Walter Klemperer's group in the Department of Chemistry at University of Illinois. The chemistry involved in the process is described in Section 2.3 Here we list the experimental details.

Tunnel Junctions with Zirconia Insulators

A four-step procedure is used to deposit insulating zirconia films on YBCO.

1. **Condensation:** The as-grown YBCO thin films are placed into an empty 50 mL beaker, transferred into an argon filled glovebox, and immersed in a 50 mL beaker containing 15 mL of a 9 mM solution of $Zr_4(O\textit{n}Pr)_{16}$ in methylcyclohexane (MCH) for 15 minutes.
2. **MCH Rinse:** After 15 minutes, the thin films are transferred to another 50 mL beaker containing ~10 mL of MCH. After gently swirling the solvent by hand for 10 s, the thin films are placed in another 50 mL beaker containing ~10 mL of MCH. After swirling the solvent again, the films are removed and rinsed twice using a 5 ¾ inch Pasteur pipette full of MCH.

3. **Hydrolysis:** The films are removed from the glove box and placed in 5 mL of 20% H_2O in *n*-propanol under ambient conditions for 15 minutes.
4. **Propanol Rinse:** The thin films are transferred to a 50 mL beaker containing ~10 mL of *n*-propanol and gently agitated. The samples are then placed in another 50 mL beaker containing ~10 mL of *n*-propanol. After gently agitating the beaker, the films are rinsed using a 5 ¾ inch Pasteur pipette full of *n*-propanol.

Each repetition of this four-step process is referred to as one condensation-hydrolysis (C-H) cycle. The extreme reactivity of the $Zr_4(OnPr)_{16}$ with moisture is such that exposure of the $Zr_4(OnPr)_{16}$-MCH solution to air results in premature condensation of the solute. Avoiding premature condensation is the motivation for the use of a glovebox in the condensation step. The use of a glovebox, however, lengthens the time required to complete the process, since the evacuation of the antechamber adds approximately 30 minutes per C-H cycle. We are able to save time in the process by using a glovebag instead of a glovebox. In this case, the $Zr_4(OnPr)_{16}$ solution is kept in an airtight container in the glovebag and a sufficiently moisture-free environment is created by purging the bag with argon gas then evacuating five times before opening the $Zr_4(OnPr)_{16}$ solution to the glovebag atmosphere. We are successfully able to further reduce the cycle time by reducing the time in solution (both condensation and hydrolysis) from 15 minutes down to one minute. Combining these changes to the process reduced the time per cycle from ~60 minutes to seven minutes without noticeable effect in the tunneling conductance measurements.

Once the zirconia insulator is deposited, one of three counter-electrode deposition methods is employed. Two of these methods require an additional step of first covering part of the surface of the film with a thick insulating layer to define regions of the film of various areas for junction fabrication. This layer is composed of Duco® cement, diluted in acetone and is applied to the surface using a fine brush.

Once the Duco® cement has been applied, the counter-electrodes are applied by one of three methods. The first method is by thermal evaporation of silver strips through a stainless steel shadow mask. The strips are evaporated across the areas uncoated with Duco® cement so that the width of the junctions are defined by the width of the shadow mask in one dimension and the space between Duco® cement strips in the other (see Figure 3.5).

The second counter electrode deposition method involves pressing a clean strip of indium onto the treated surface of YBCO. The indium strip is prepared by cutting a small strip of indium from an indium ingot with a clean razor blade such that all exposed surfaces of the indium strip have been freshly cut. The indium strip is then laid across the uncoated YBCO as shown in Figure 3.5 and pressed onto the surface using either a pair of Teflon-coated tweezers or a small vise coated with Teflon tape.

In the third counter electrode deposition method, no Duco® cement is used. The counter electrode is applied by first producing narrow (~0.1 mm) wires from flexible (12 μm thick) aluminum foil. The wire is then bent into a v-shape, the apex of which is then dipped into a bead of silver paste and then applied directly to the treated YBCO surface. The silver paste, which is acquired commercially, is a silver colloid and proprietary polymer solution suspended in butyl acetate. This simple technique, though less robust to thermal cycling, proves to be the most reliable and produces among the highest quality junctions. It is possible to fit many more junctions per film, compared to evaporated metal or pressed indium junctions, which are usually limited to three to four junctions per ~5 mm × 8 mm YBCO thin film.

3.3 Tunneling Conductance Measurements

Once the junctions have been fabricated, leads are attached in a standard four-probe geometry: two on each counter electrode and two directly contacted to the YBCO thin film as shown in Figure 3.5. The positive electrodes are contacted to the YBCO, so that positive bias probes the filled electron states.

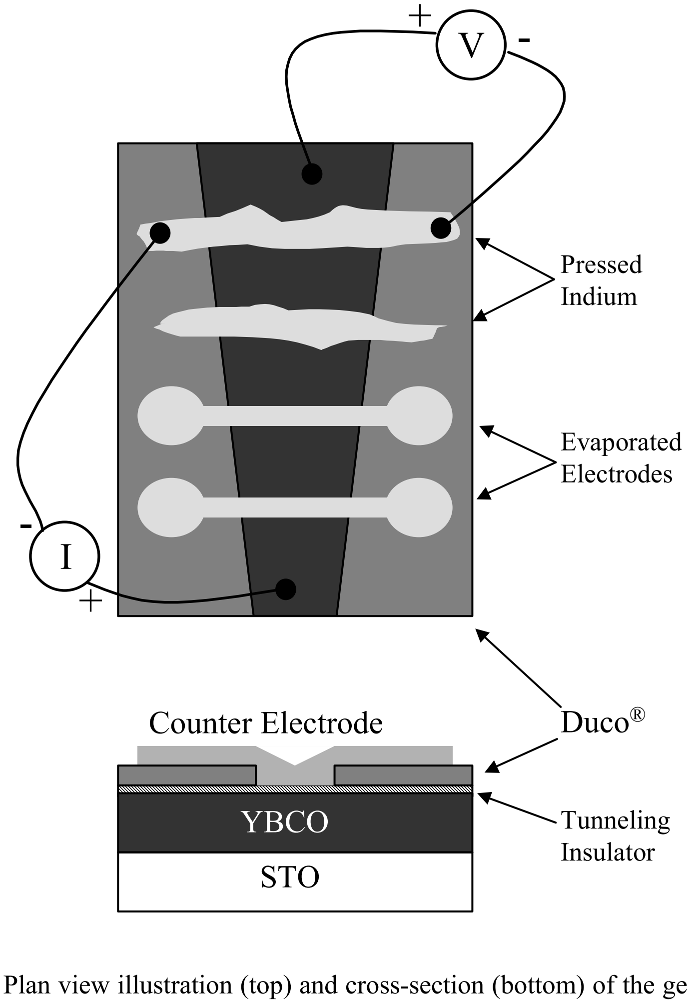

Figure 3.5. Plan view illustration (top) and cross-section (bottom) of the geometry of the planar tunnel junctions, which shows the configuration of the different layers, two types of counter-electrodes and the four-probe measurement geometry. Film dimensions are typically 5 mm × 8 mm × 100 nm. Junction areas are typically 0.1–0.3 mm^2.

The YBCO contacts are made by using a diamond scribe to scratch through the zirconia insulator at the surface of the film and then making contact using silver paste and flexible aluminum wire. Each counter electrode deposition technique requires a different contact method. Contact to evaporated metal electrodes is made in the same way as the contacts to the YBCO, i.e. using silver paint and flexible aluminum wire. Leads to pressed indium are composed of thin (75 μm diameter) gold wires soldered to the indium. As described above, the leads for silver paste counter electrodes are embedded in the electrode. The film containing the junctions is then mounted to a probe for cryogenic tunneling measurements. A diagram of the apparatus for tunneling measurements is shown in Figure 3.6.

The differential conductance is measured directly by biasing the junction with a DC signal superimposed with a small AC signal. This AC signal (current) and the AC response (voltage) are read using separate but synchronized lock-in amplifiers. The signal is swept and the data are taken automatically by a PC using Labview. The DC current-voltage characteristics are also read and are used to verify the AC measurement. Measurements are taken in a ^{4}He cryostat equipped with a superconducting magnet. The cryostat enables measurements from room temperature to 1.5 K and magnetic field measurements, up to 12 T.

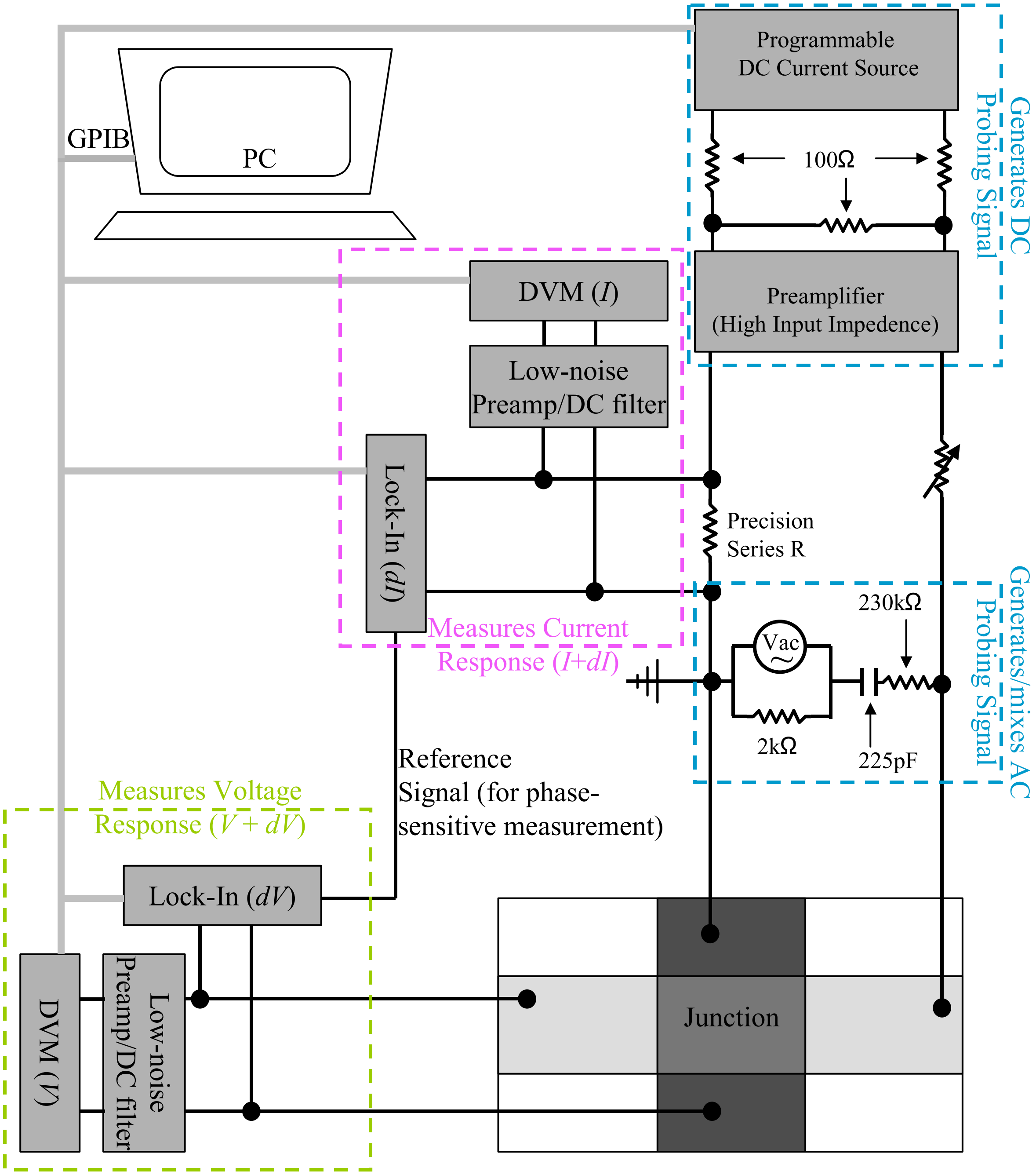

Figure 3.6. Schematic of the electronics used in differential conductance measurements. The measurement process is described in the text.

3.4 References

1. L.H. Greene, B.G. Bagley, W.L. Feldmann, J.B. Barner, F. Shokoohi, P. Miceli, B.J. Wilkens, A. Fathy, D. Kalokitis, and V. Pendrick, Appl. Phys. Lett. **59,** 1629 (1991).

2. R.W. Berry, P.M. Hall, and M.T. Harris, *Thin Films*. 1968, New York: Van Nostrant Reinhold Company.
3. R. Parsons, in *Thin Film Processes II*, J.L. Vossen and W. Kern, Editors. 1991, Academic Press: Boston. p. 188.
4. Z. Trajanovic, I. Takeuchi, P.A. Warburton, C.J. Lobb, and T. Venkatesan, Appl. Phys. Lett. **66,** 1536
5. O. Nakamura, J. Guimpel, F. Sharifi, R.C. Dynes, and I.K. Schuller, Appl. Phys. Lett. **61,** 2598 (1992).
6. S. Mahajan, W. Ito, Y. Yoshida, and T. Morishita, Physica C. **213,** 445 (1993).
7. D.E. Pugel and L.H. Greene, Appl. Phys. Lett. **75,** 1589 (1999).
8. M. Covington, R. Scheurer, K. Bloom, and L.H. Greene, Appl. Phys. Lett. **68,** 1717 (1996).
9. S.K.H. Lam, Physica C. **370,** 79 (2002).

Chapter 4

Thin Films

Thin films are chosen as the vehicle for these experiments as opposed to single crystals for a variety of reasons. First, growing thin films affords the preparation of pristine surfaces of four crystallographic orientations of YBCO: (001), (103), (100) and (110). To expose these surfaces on single crystals, the samples must be polished [1], a process which causes damage to the surface. Furthermore, since thin films are the basis for microelectronics research and industry, a wealth of knowledge and techniques exists for their fabrication and processing. Finally, the large surface area of thin films relative to single crystals allows many junctions to be made on a single film to check reproducibility and increase statistics.

4.1 YBCO Thin Film Analysis

The highly anisotropic nature of YBCO, as described in Section 3.1, is evident in the analysis performed on the films. Each of the four orientations has its own signature in each analysis technique, *i.e.*, ρ *vs.* T, XRD, SEM and AFM, such that once knowledge of the general results of these techniques is established, it is possible to identify the film orientation from any single technique. For a full account of the film quality, however, each technique must be employed. XRD, SEM and AFM measurements are carried out in the Center for Microanalysis of Materials.

X-Ray Diffraction

In an anisotropic material such as YBCO, knowing the crystallographic orientation is essential to understanding the experiments. Information about the crystal structure and orientation is obtained from x-ray diffraction measurements. In this technique, nearly monochromatic x-rays, incident on the YBCO surface with angle θ, scatter from neighboring planes and reflect from them with angle 2θ. The path difference between x-rays scattered by neighboring planes is given by $2d\sin\theta$. When that difference is equal to an integer multiple of the x-ray wavelength, there is constructive interference and a peak in the θ-2θ spectrum is detected.

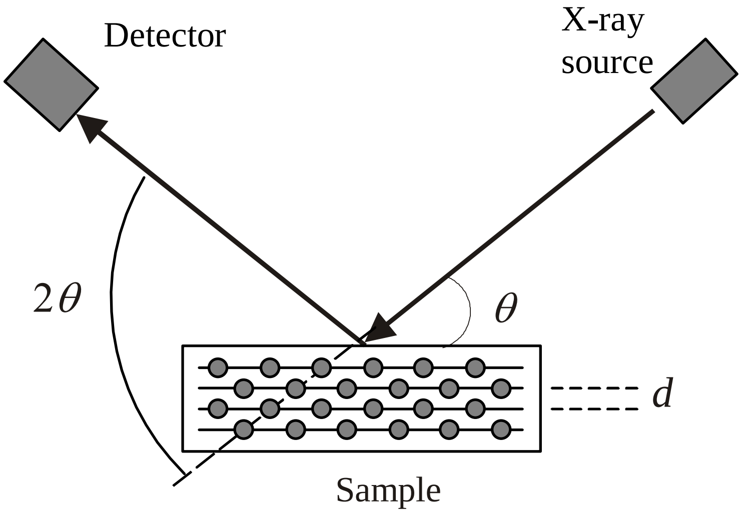

Figure 4.1. Illustration of the Bragg-Brentano geometry used for XRD measurements.

Using this Bragg-Brentano technique, the spacing between planes parallel to the surface is measured, and then by comparing to known values for YBCO, the orientation is determined.

XRD spectra taken on a Phillips X'Pert diffractometer using Cu K-α radiation wtih $\lambda = 1.54439$ Å. The spectra for the four YBCO orientations are shown in Figure 4.2. The most prominent peaks in the spectra are attributed to the STO substrates. From the Figure, it is clear that (001)- and (100)-oriented YBCO are both grown on STO (100), and that YBCO (103) and (110) are grown on STO (110). The remaining peaks in Figure 4.2a are *c*-axis peaks of YBCO, with the exception of the peak at $2\theta \cong 32^{o}$, which is attributed to Y_2O_3 outgrowths, as described in the next Section. YBCO (n 0 3n) peaks are overshadowed by the substrate peaks in Figure 4.2b, due to the close lattice match between STO (110) and the YBCO (103) plane. The (n00) and (nn0) peaks are visible, however in Figure 4.2c and d, respectively, due to the small lattice mismatch with the substrates at those orientations. The data in Figure 4.2c also show the YBCO (005) peak, indicating that a small *c*-axis phase has nucleated in that sample. This is common for *a*-axis films.

Scanning Electron Microscopy

Since planar tunneling is a highly surface-sensitive probe, the YBCO films are optimized for high surface quality. SEM provides a detailed qualitative measurement of the surface morphology. SEM is analogous to optical microscopy but electrons are used in the place of photons. Whereas photons are resolution limited by visible wavelengths, electrons, with a de Broglie wavelength on the order of 1 Å have resolving power over a thousand times greater than visible light.

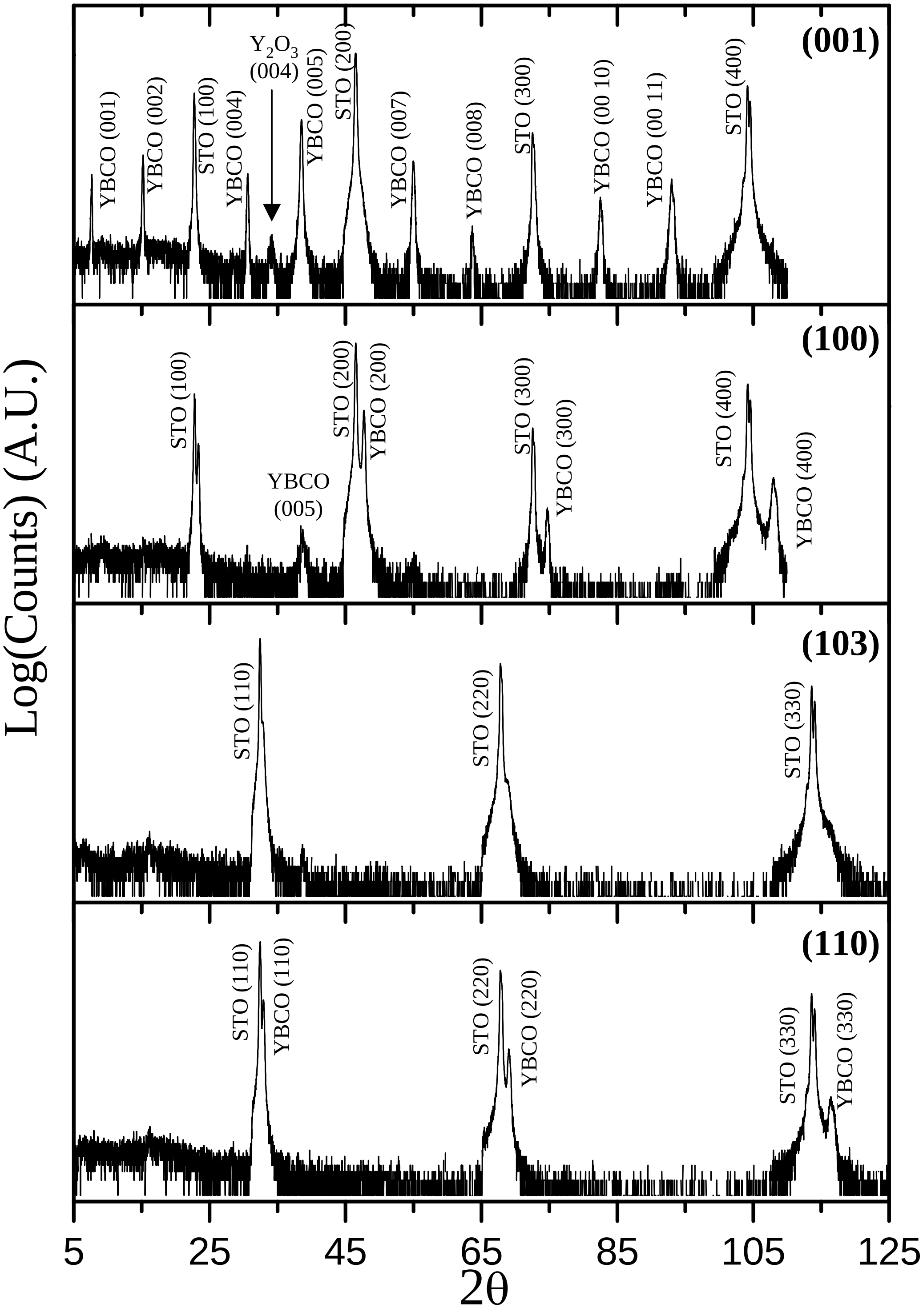

Figure 4.2. XRD spectra for (001)-, (103)-, (100)- and (110)-oriented YBCO. All peaks are native to the substrate or intended crystal orientation except for the Y_2O_3 (004) peak in (001) spectrum and the YBCO (005) peak in (100) spectrum. The lack of visible YBCO peaks in the (103) spectrum is due to the close lattice match of the YBCO thin film with the STO substrate.

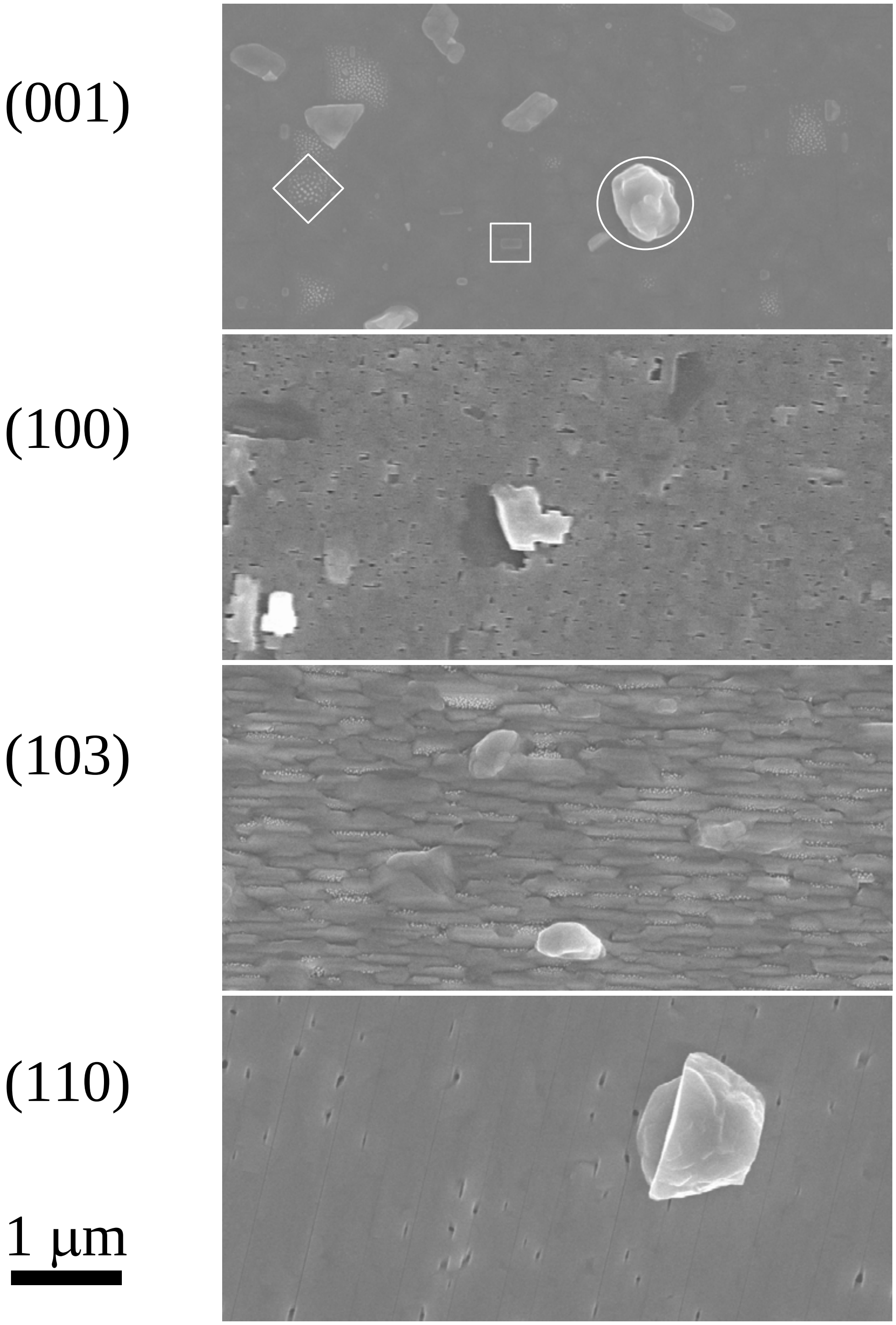

Figure 4.3. SEM images for four different orientations of YBCO: (001), (103), (100) and (110). The (001) image features three common outgrowths common to YBCO films. CuO_x "boulders" (circle) and Y_2O_3 "mushrooms" (diamond) are seen on all four orientations and *a*-axis grains (square) are sometimes observed on (001) films. Holes are also apparent in (c) and (d) and cracks, which indicate the CuO_2-plane direction, are seen in (d).

All SEM images are taken on a Hitachi S-4700 SEM. A representative image for each orientation is shown in Figure 4.3. Each image has features that obviously distinguish it from the other three. For the (001) film (Figure 4.3a), the YBCO background is mostly featureless at this magnification, but various outgrowths are seen in the foreground. The most prominent are the "boulder" outgrowths, indicated by the circle. We have identified these particles by energy dispersive x-ray spectroscopy (EDS) as being copper and oxygen rich, and this is in agreement with the literature [2-4]. These features are most prominent on the two orientations grown on (100)-oriented STO, namely (001)- and (100)- YBCO. The precipitates are observed in YBCO films grown by all common methods, including sputtering, molecular beam epitaxy, chemical vapor deposition and laser ablation [5] and tend to detract significantly from the superconducting critical current of the films because they nucleate at the substrate/film interface [6, 7].

The smaller outgrowths, which we refer to as "mushrooms", are indicated by the diamond in Figure 4.3c. Though these features are too small to be identified by EDS, they have been identified in the literature as Y_2O_3 precipitates [2, 8], and Y_2O_3 (004) reflections have been reported in the literature [9, 10] and routinely appear in our XRD spectra (see Figure 4.2a). These features often appear inside holes in the YBCO surface as shown in Figure 4.4. It has been suggested that these holes result from the nucleation of a Y_2O_3 grain and the inability for YBCO to wet the Y_2O_3 surface [11].

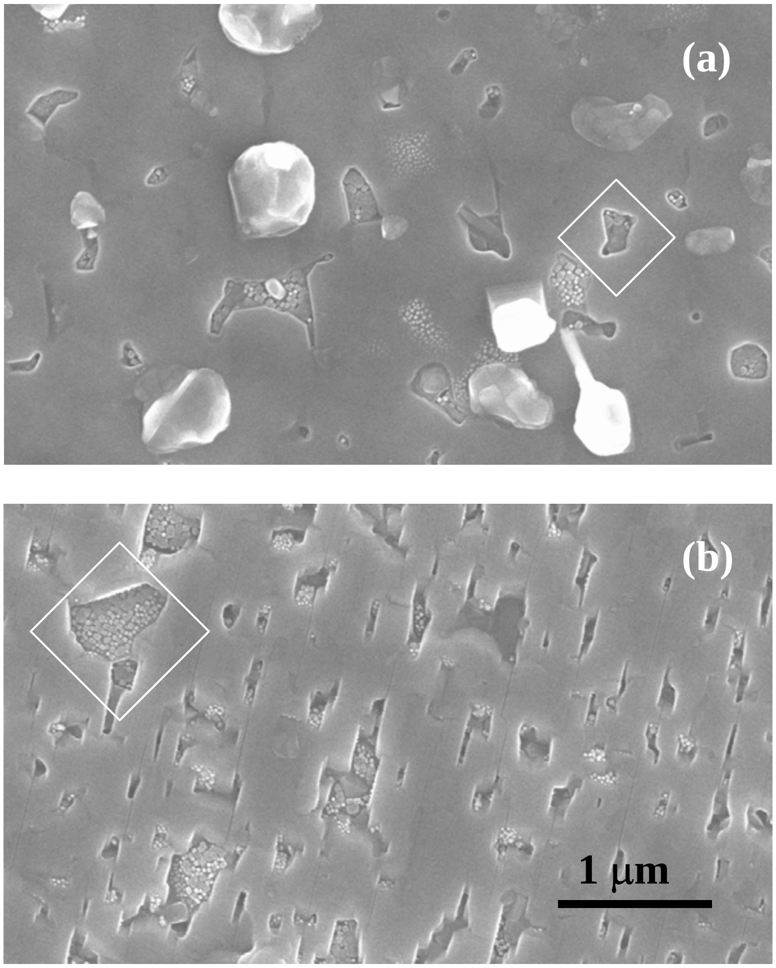

Figure 4.4. Y_2O_3 “mushrooms” growing inside holes in the surface of (a) (001)-oriented and (b) (110)-oriented YBCO films.

Various techniques have been suggested as ways to reduce or eliminate the number of each of these types of outgrowths [3, 6, 11, 12] but conditions change with YBCO target age [12] so that once parameters have been optimized to remove the outgrowths, they can reappear in later growths, making it difficult to eliminate them altogether. Since these species are insulating, however, and the dimensions of the features (hundreds of nm for “boulders” and tens of nm for “mushrooms”) are much too large for electron tunneling, the regions of the film with outgrowths at the surface do not contribute to the tunneling conductance, and are effectively taken out of the experiment.

Regions that contain holes cannot be ignored so easily, however. The edges of the holes expose film orientations other than the surface normal direction and film growth parameters must be adjusted to avoid them. Since it is believed that the holes are present due to a deficiency in target oxygen [11], additional oxygen may be reintroduced to the target by presputtering at a higher partial pressure. Often, however, a new target is necessary [12].

The feature in Figure 4.3a, indicated with a square, is a grain of *a*-axis-oriented YBCO, or an "*a*-axis grain". These grains appear only on (001)- YBCO or on YBCO with mixed (001) and (100) phases. These have been identified by cross-sectional transmission electron microscopy (XTEM) [2] and result when a *c*-axis film is grown at a temperature below the optimal value for *c*-axis growth. Alternatively, for *a*-axis films, *c*-axis phases can nucleate if the growth temperature is too high. The transition from (001)- to (100)- YBCO is shown in Figure 4.5.

Figure 4.3b shows that (103) surfaces have the highest roughness of the four orientations, with their mountain-range-like morphology, which is a manifestation of CuO_2 planes protruding from the surface at 45°. Figure 4.3d illustrates that (110) surfaces are among the smoothest, though cracks that run several microns along the surface are evident in thin films of this orientation. These cracks are always seen in (110)-oriented YBCO and it has been shown [13] that the cracks run along the *ab*-plane direction, making it a straightforward task to determine the plane orientation by a simple SEM analysis.

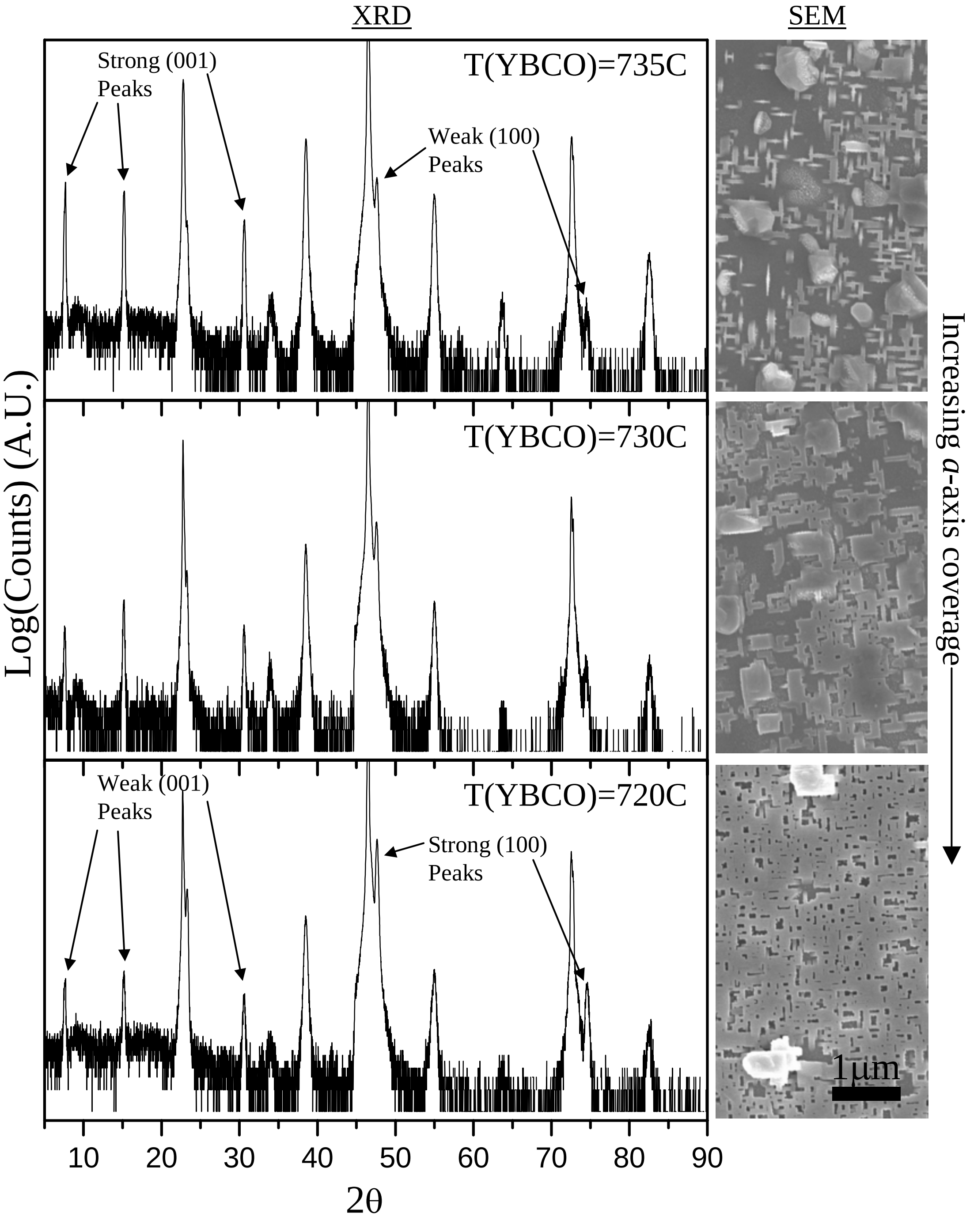

Figure 4.5. Progression from *c*-axis to *a*-axis YBCO thin film orientation by variation of the YBCO growth temperature. SEM images on the right show the surface morphology of YBCO films grown at 735°C (top), 730°C (middle) and 720°C (bottom). An increasing amount of *a*-axis phase results as the temperature is decreased. The figures on the left show the corresponding θ-2θ XRD spectra for the same films, revealing an increase in the magnitude of (*n*00) peaks (*a*-axis phase) from top to bottom and a decrease in the magnitude of (00*n*) peaks (*c*-axis phase).

Atomic Force Microscopy

AFM constitutes another surface probe for our films and gives a quantitative account of the surface morphology to complement the qualitative SEM analysis. AFM gives a topographical mapping of the YBCO surface by suspending a sharp tip (radius of curvature < 10 nm), which has been fabricated on the end of a silicon cantilever, over the surface of the film.

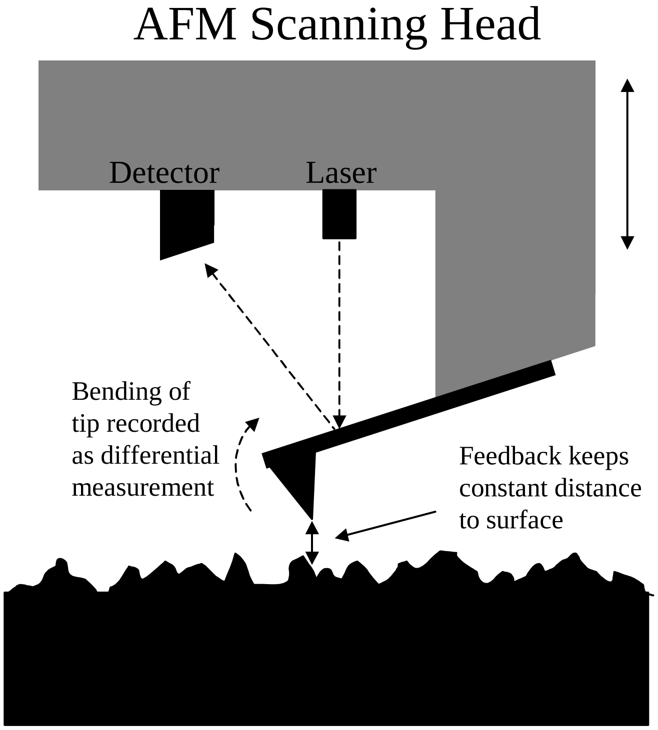

Figure 4.6. Illustration of the AFM measurement apparatus. The scanning head scans in the plane of the film and keeps a constant distance with the film surface through a feedback loop that keeps the laser beam in the center of the detector. Differential images are obtained when deflection of the AFM tip is measured by recording the deflection of the laser beam in the detector.

A laser beam is then reflected from the back of the cantilever and the deflection of the laser beam is measured as the tip is scanned over the YBCO surface. As van der Waals forces between the tip and the film cause the tip to deflect up and down with the topology of the film surface, the deflection of the beam triggers a feedback loop to maintain a constant distance between the tip and the film. Thus, the topology of the surface is recorded with this noninvasive technique. Fine detail is measured on the film surface by differential measurements. The differential AFM measurement reads the bending of the tip from its rest position by recording the position of the laser beam in the detector (Figure 4.6).

A Digital Instruments Multimode AFM is used to obtain the images of YBCO surfaces. Figure 4.7 shows AFM and SEM micrographs. On the left is a differential image of a (001)-oriented YBCO thin film [14]. It reveals pyramidal island growth mode typical of *c*-axis YBCO thin films. The ridges around the pyramid have an average height of 1.2 nm. Given that the *c*-axis lattice constant is 1.168 nm, it's clear that the AFM can resolve single YBCO unit cells. The same ridge morphology is seen in the SEM image.

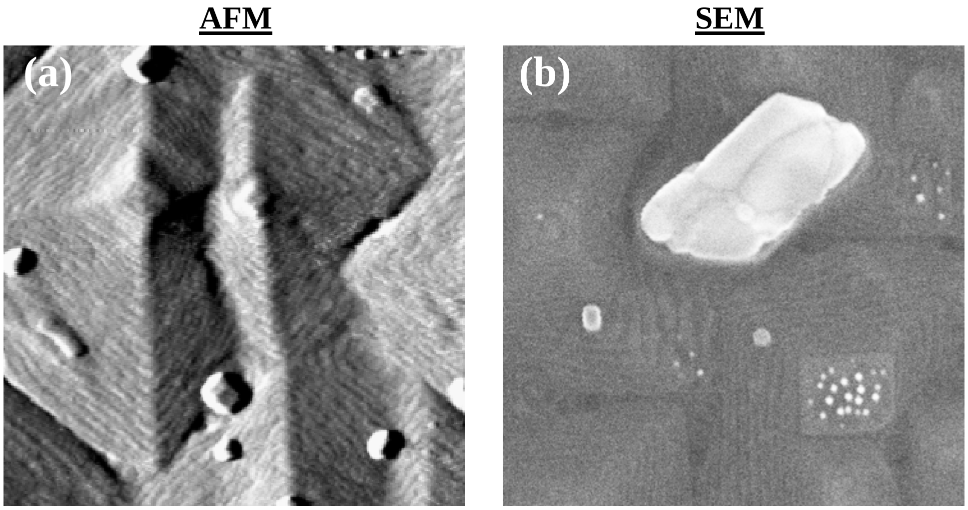

Figure 4.7. AFM (a) and SEM (b) images of (001)-oriented YBCO films. The ridges in the AFM image have a step height of 1.2 nm, which is consistent with the *c*-axis lattice constant of 1.168 nm. The AFM image was taken by Glenn Westwood. The figures are 1 μm per side.

Figure 4.8 compares the results of AFM and SEM images of YBCO (110) thin films. Roughness analysis reveals an RMS roughness of 4.6 nm for the (110)-oriented YBCO thin film and 7.1 nm for the (100)-oriented film with roughness measurements of less than 1 nm over the area enclosed by the 150 nm square, illustrating regions of atomic smoothness.

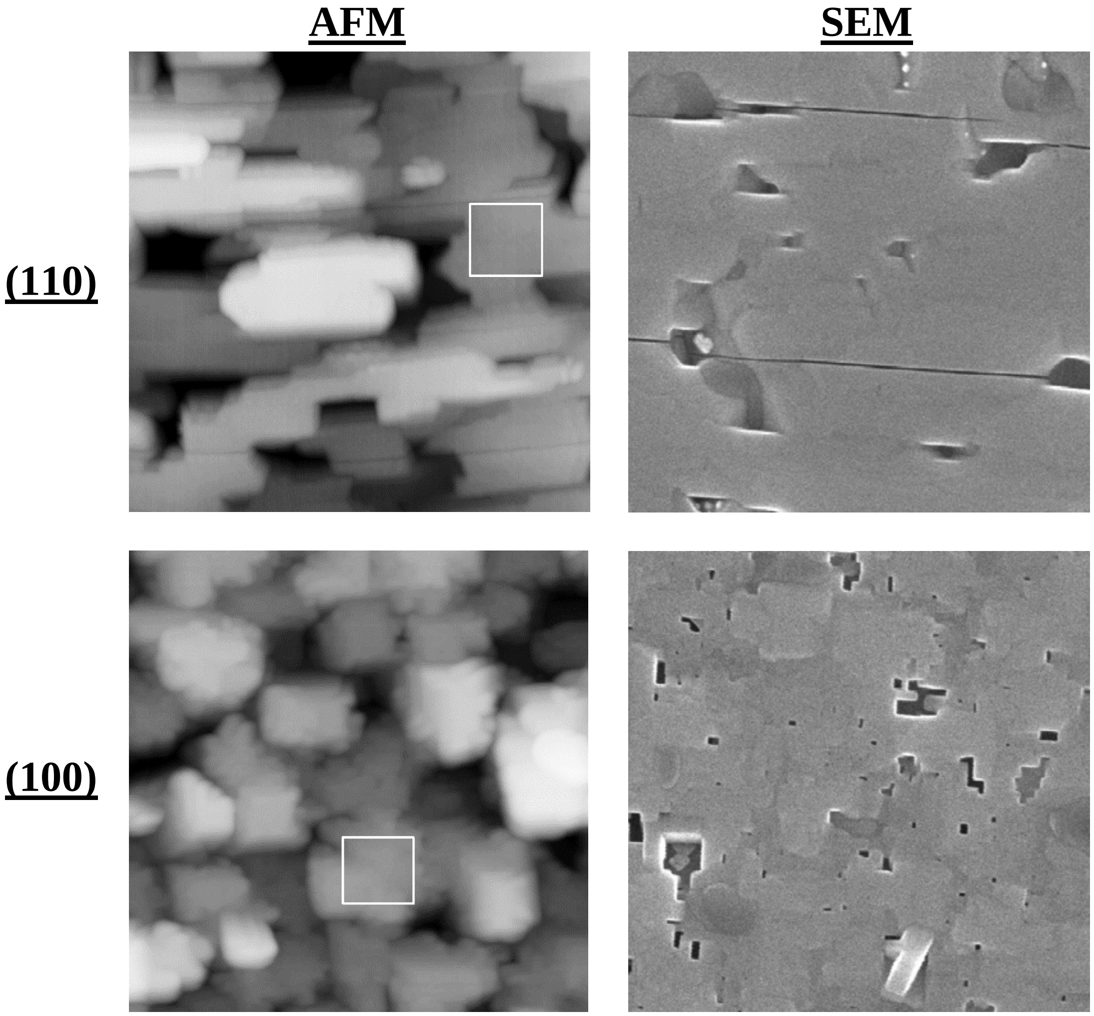

Figure 4.8. AFM (left) and SEM (right) images of (110)-oriented (top) and (100)-oriented (bottom) YBCO thin films. The AFM image and SEM image are from the same film for each orientation. All images are 1 μm on a side. The overall RMS roughness is 4.6 nm and 7.1 nm for the (110)- and (100)-oriented films, respectively. The white squares are 150 nm on a side and enclose areas with RMS roughness of less than 1 nm in each case, illustrating the remarkable smoothness of these YBCO thin films.

Resistivity vs. *Temperature*

It is well-known that the ρ *vs.* T characteristics of YBCO, and most high T_c superconductors, follows a linear dependence in the normal state [15]. This dependence is routinely measured in our *c*-axis and (103)-oriented films, with residual resistivity ratios [$RRR \equiv \rho(300\text{K})/\rho(100\text{K})$] typically exceeding 3.0. The width of the superconducting transition (calculated as 90% – 10% of the value extrapolated from the normal state) is typically 2–4 K. The resistivity *vs*. temperature for (100) and (103) YBCO thin films from room temperature to 75 K are shown in Figure 4.9.

Figure 4.9a shows linear normal-state resistivity, as does the curve in Figure 4.9b with transport in the *ac*-direction (black data). The curve that shows transport along the *b*-axis (grey data), however, shows a resistivity approximately ten times lower with slight upward curvature. According to our interpretation, the difference in the shape of the latter data is due to additional charge carriers in this direction contributed by the CuO chains.

Optimizing surface quality in (110)- and (100)-oriented thin films exacts a cost on bulk transport. Films grown under conditions optimized for surface quality routinely show deviations from the linear normal state resistivity, often exhibiting a slight downward curvature with transition widths of approximately 5 K and *RRR*s typically between 1.2 and 1.5.

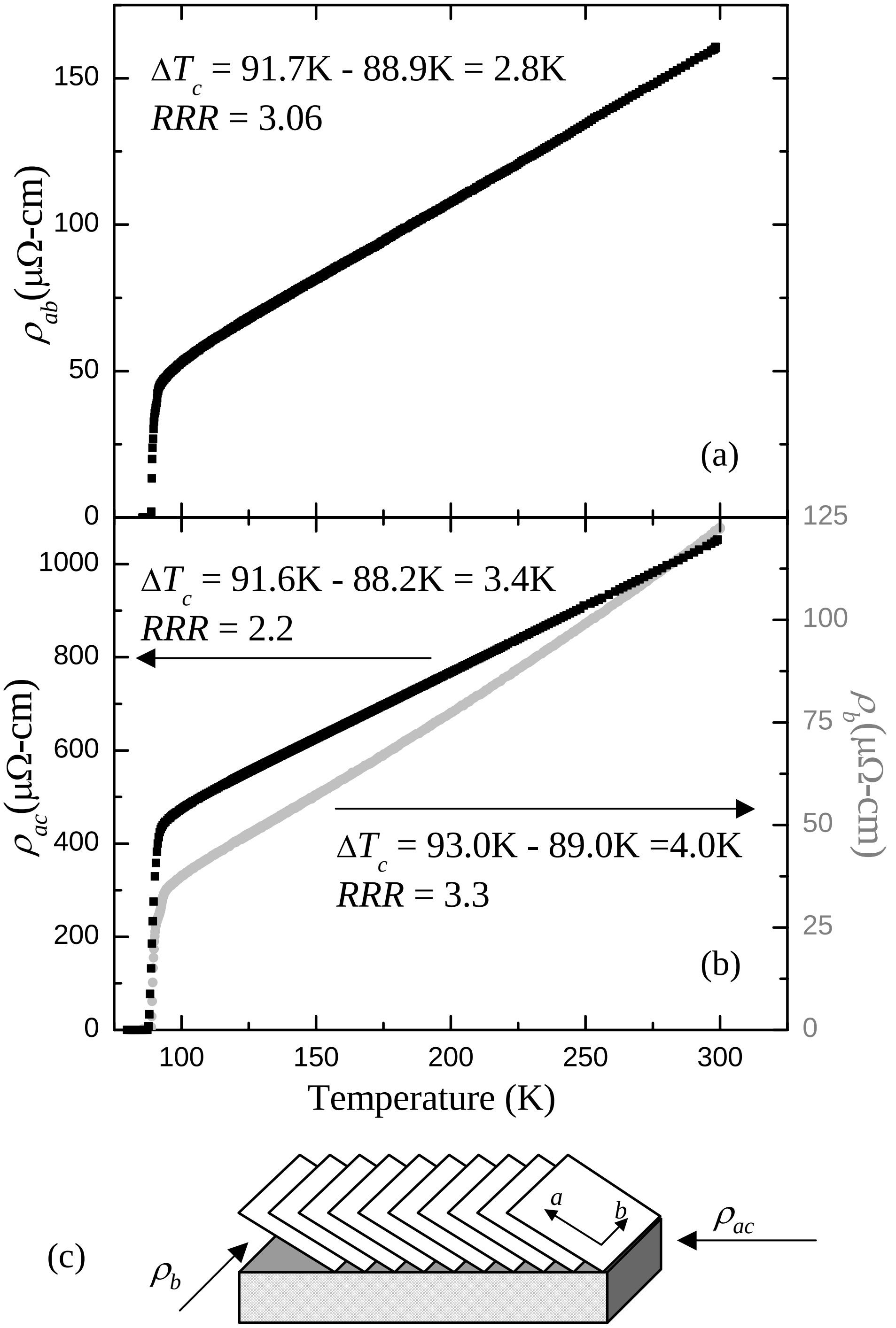

Figure 4.9. Resistivity *vs.* Temperature curves of (103)-oriented (a) and *c*-axis oriented (b) YBCO thin films. The anisotropy in the resistivity of the (103)-oriented films is exhibited by plotting the transport characteristics along the *b*-axis (gray) and along the *ac*-direction (black). The diagram (c) illustrates the geometry for the measurements on the (103)-oriented thin film.

4.2 Insulating Thin Films of Zirconia

We deposit ultra-thin insulating films of zirconia on YBCO by the method described in Section 3.2. The films are characterized using XTEM, AFM and tunneling spectroscopy. XTEM quantifies the thickness and uniformity of the zirconia barrier at the local level. AFM reveals information about the effect of the zirconia coating YBCO surface morphology. Tunneling exhibits the performance of the coating as a tunneling insulator on a macroscopic scale.

Transmission Electron Microscopy

XTEM images are obtained in collaboration with Jianguo Wen at the Center for Microanalysis of Materials. Images are obtained with a JOEL 2010F scanning TEM. Due to delamination of the samples, likely during the mechanical polishing process in preparation for XTEM measurements, images are only obtained for (103)-oriented YBCO films. The zirconia seems to be deposited most uniformly over smooth areas of the YBCO thin film surface as shown in Figure 4.10b and tend to be less uniform around sharp peaks in the (103)- YBCO landscape, as shown in Figure 4.10c.

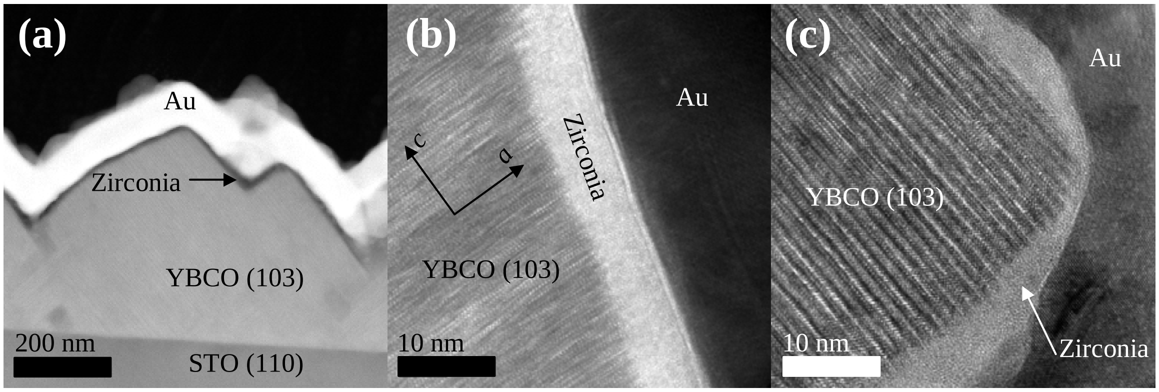

Figure 4.10. XTEM images of (103)-oriented YBCO coated with zirconia according to the process described in Section 3.2. The zirconia barrier is shown to conform well to the surface in (a) but nonuniformity in the barrier is particularly apparent at peaks in the (103) surface morphology as shown in (c).

Further evidence of non-uniformity of the barrier is seen in tunneling analysis, as is described below. The zirconia layers, which are fabricated using fourteen C-H cycles, show barrier thicknesses ranging from 1–7 nm.

Atomic Force Microscopy

Thin films of (001)- and (103)-oriented thin films were prepared in the following ways:

- **Uncoated:** as grown condition
- **Coated:** 14 C-H cycles, as described in Section 3.2.
- **Cycled/Uncoated:** 14 cycles of the C-H process, but with no $Zr_4(OPr^n)_{16}$ present in solution.

AFM measurements are reported for all the films, except for the cycled/uncoated (103)-oriented thin film, for reasons described below. The results of the study are shown in Figure 4.11. The same pyramid-like structures are observed on the (001)-oriented film from each preparation method. The uncoated and coated thin films are similar, but the cycled/uncoated film is covered in small (< 100 nm) particles. To quantify the result of this processing, a 150 nm × 150 nm region is selected on the side of a pyramid structure from each *c*-axis film, a plane was fit to the data and the fit was subtracted.

The result of the altered image from the uncoated film (Figure 4.12) shows an RMS roughness of 0.143 nm. The roughness of the coated film is slightly higher at 0.554 nm. The most dramatic change comes from the cycled/uncoated film, which shows an increase in roughness to 2.01 nm. Similar results are obtained on (103)-oriented YBCO films, which show an increase from 0.133 nm on the uncoated film to 0.381 nm on the coated film, indicating the zirconia coating only increases the surface roughness by ~0.25 nm. In contrast, the surface of the cycled/uncoated film is deteriorated to an extent that was easily visible with the naked eye, so there is not need to perform AFM measurements on this film. The results of roughness analysis for *c*-axis oriented films are illustrated in Figure 4.12.

This analysis shows that the coated films remain smooth when $Zr_4(OPr^n)_{16}$ is present in the C-H processing. Since AFM is a means of providing a topographical map of the surface only, it is impossible to determine from AFM alone whether the YBCO film surface itself remains smooth or if pits are introduced onto the YBCO surface, but are filled in with zirconia. We refer to the TEM measurements to distinguish between these two possibilities. We see no evidence at the YBCO/zirconia interface in Figure 4.10b of the magnitude of surface roughness observed in the cycled/uncoated film in Figure 4.11. Indeed, since Figure 4.10 shows the TEM results for a (103)-oriented film, the YBCO surface degradation is expected to be higher if it exists, due to the high oxygen mobility at this orientation. These results, taken together, show that the YBCO surface smoothness is well-preserved when $Zr_4(OPr^n)_{16}$ is present in the C-H processing. We also have evidence that the C-H processing passivates the surface of YBCO, as shown in the tunneling spectroscopy results in the next section.

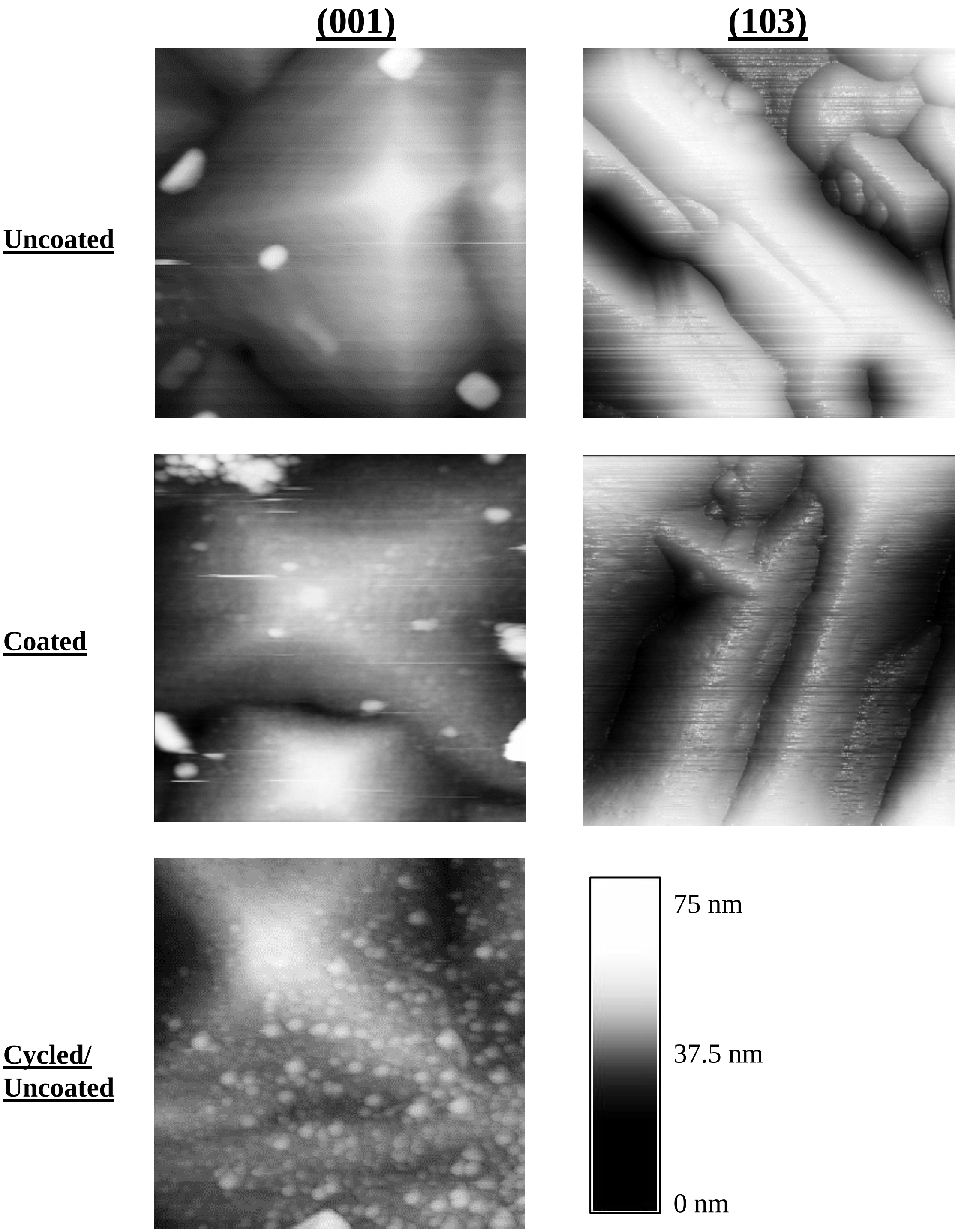

Figure 4.11. AFM results of uncoated, coated and cycled/uncoated (001)-oriented YBCO thin films and from uncoated and coated (103)-oriented YBCO thin films. The images are 1 μm on each side for the *c*-axis images and 500 nm for the images of (103)-oriented YBCO. The grayscale table indicates the height for the *c*-axis images. The (103) images are 3-d renderings with a simulated illumination, intended to emphasize the differences between the two (103) images [14].

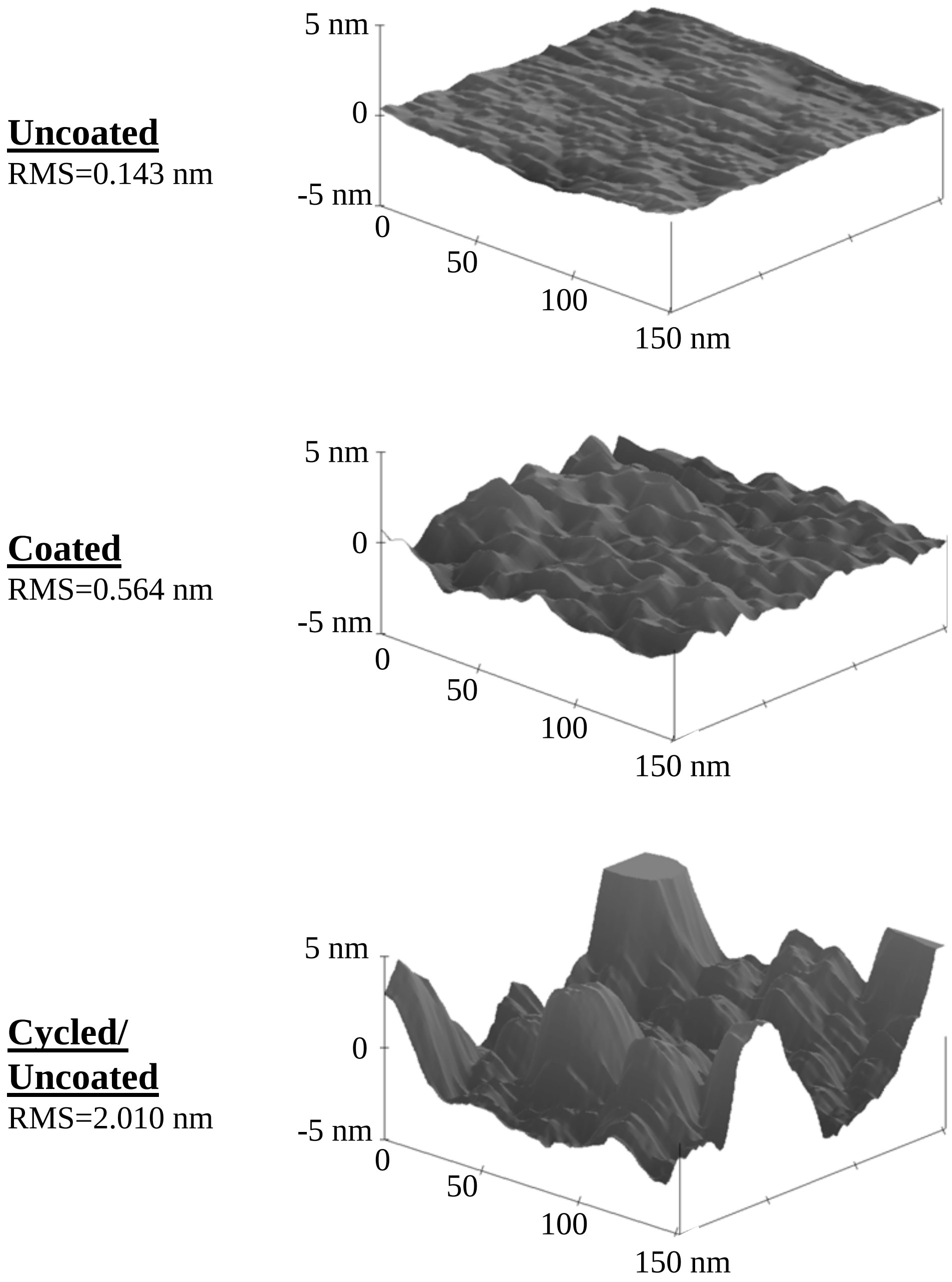

Figure 4.12. Results of plane-fitted AFM scans on (001)-oriented films that have been uncoated, coated and cycled/uncoated. The RMS roughness increases from 0.143 nm for the uncoated film to 0.564 nm for the coated film to 2.010 nm for the cycled/uncoated film [14].

Tunneling Spectroscopy

The efficacy of zirconia as an insulator coating is probed by tunneling spectroscopy. We have evidence that in addition to providing a robust tunneling barrier, the solution-deposited zirconia coating provides a passivating layer that prevents oxygen loss from the surface of the YBCO. As discussed in Section 2.2, the YBCO surface is susceptible to oxygen loss [16], such that surface doping can change over time. Thus, one expects to see changes in the surface DoS as well. We find that films kept at laboratory ambient conditions for over one year, show similar conductance characteristics. In the data in Figure 4.13, two junctions were fabricated on a single (103)-oriented YBCO thin film. The first was fabricated immediately after film growth, using evaporated silver counter-electrodes. The second was fabricated over one year later, using silver paste counter electrodes. Despite the difference in counter electrode deposition method, and time between fabrications of the two junctions, the results are very similar.

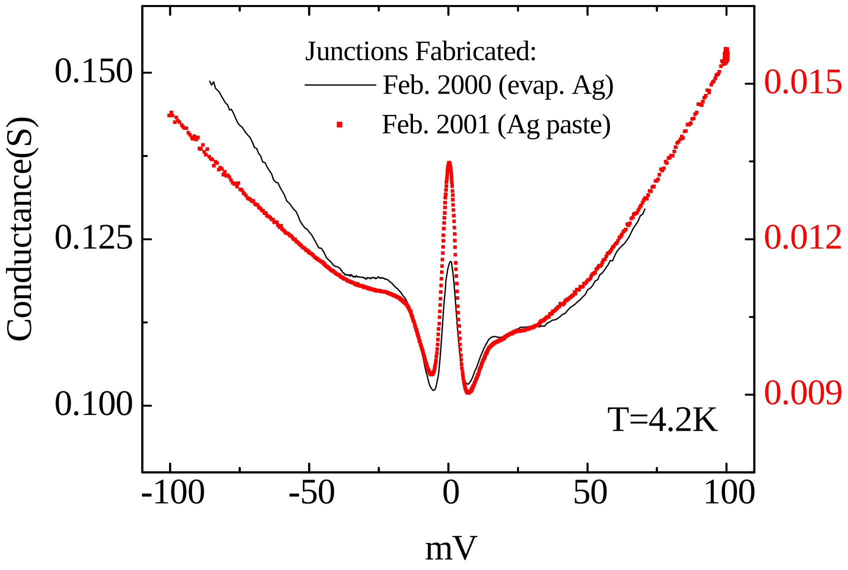

Figure 4.13. Two tunnel junctions, fabricated on the same YBCO thin film over a year apart, and with different counter electrodes show similar characteristics. This suggests the YBCO surface is passivated by the zirconia.

Tunneling can also be used to gain quantitative information about the nature of the tunneling barrier. We have fabricated hundreds of tunnel junctions on YBCO thin films using four crystallographic orientations and using three counter-electrode deposition techniques, as described in Section 3.2. Figure 4.14a shows the values of the product of the junction resistance and junction area, *R*A* for several different tunnel junctions fabricated with varying number of C-H cycles and varying counter-electrodes on a semi-log plot. Each data point with error bars is the result of an average of between two and five tunnel junctions. The error bars are calculated as the standard error of that distribution. The data points without error bars are the result of one junction for each data point.

The data show a strong dependence on the type of counter-electrode used. Junctions fabricated with evaporated silver counter-electrodes in this range of C-H cycles typically show junction resistances that are too small to make tunneling measurements. The silver paste junctions show a weak dependence of junction resistance on C-H cycle number but several junctions in this range of C-H cycles showed sharp peaks and dips in the conductance data, as well as increasing junction resistance with decreasing temperature. Both this temperature dependence and the sharp features are commonly observed in junctions characterized by metallic shorts. Junctions fabricated with pressed indium counter-electrodes, on the other hand, show a strong dependence of junction resistance on C-H cycle number. As shown in Section 2.1, the tunneling resistance is exponentially dependant on the barrier thickness. This is consistent with the linear behavior, up to about four C-H cycles, of the data in Figure 4.14b but data tends to saturate at high cycle number.

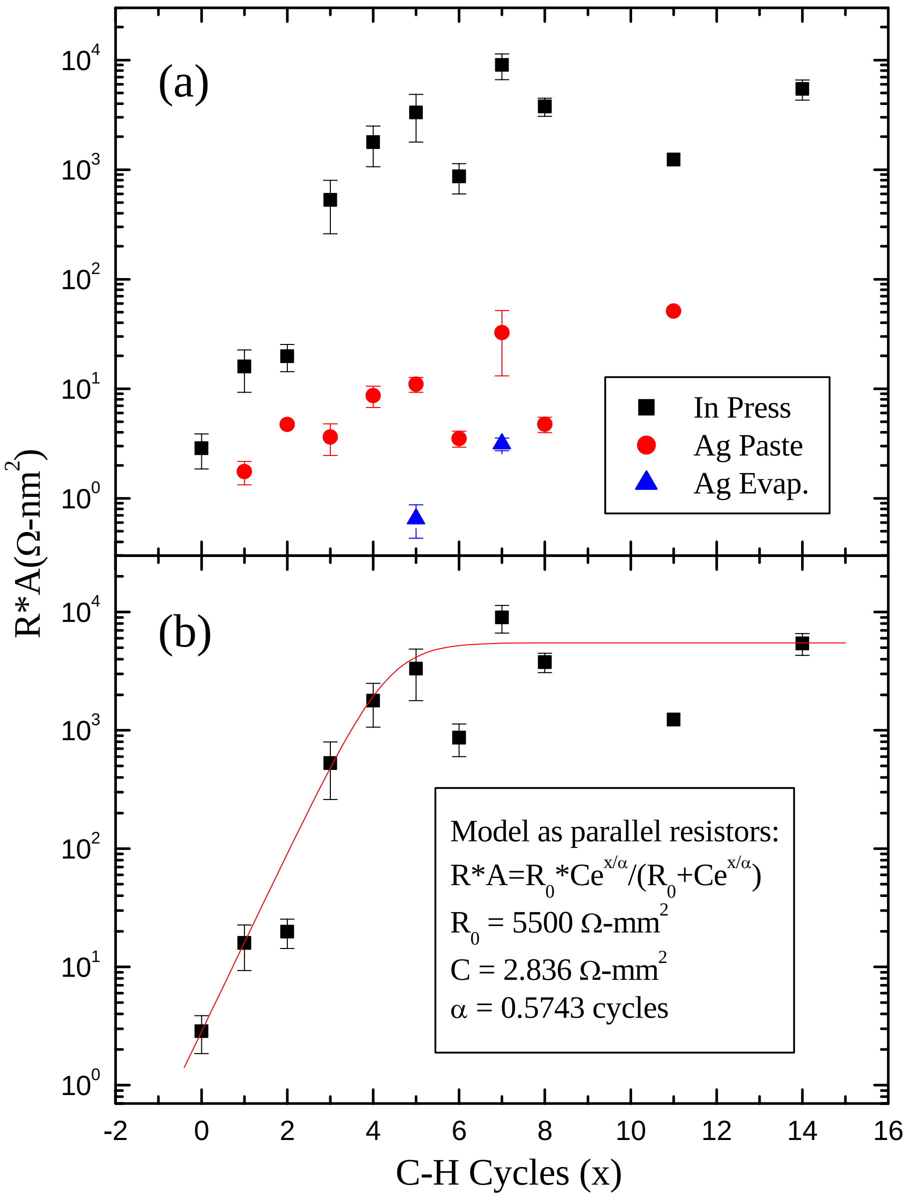

Figure 4.14. Semi-log plot of the resistance times area as a function of the number of C-H cycles for several tunnel junctions on (110)-oriented zirconia-coated YBCO. Results are shown for junctions fabricated with three different counter-electrode deposition techniques (a) and only for junctions with pressed indium counter-electrodes (b). The line in (b) is a model of two parallel resistors, as described in the text. Each data point with error bars is an average of several junctions. All junctions are measured at 1.4K.

We believe this behavior can be understood in terms of the morphology of the zirconia insulator formed at the surface of the YBCO thin films. For films coated with between one and eight C-H cycles, junctions fabricated with evaporated silver counter-electrodes typically exhibit low values of resistance, suggesting that there exist pinholes in the barrier, allowing the counter-electrode to make direct contact to the YBCO film. Considering that the XTEM data on thin films coated with 14 C-H cycles show regions with barriers as thin as 1 nm, thin films coated with fewer C-H cycles could likely contain uncoated regions, which would be prone to production of metallic shorts when a metallic overlayer is evaporated. The silver paste is less likely to produce a short through the pinholes than an evaporated electrode, but is more likely to do so than an electrode fabricating by pressing a soft solid metal onto the coated film surface, as in the case of the indium press junctions. This is consistent with the data, which shows that evaporated silver junctions have the lowest resistances and indium press junctions have the highest.

As shown in Figure 4.14b, the resistance of the indium press junctions as a function of C-H number exhibits crossover behavior. This behavior has been observed previously in tellurium barriers in niobium-based Josephson junctions [17]. We associate this dependence with the existence of electron states within the barrier, which provide “shortcuts” for multi-step tunneling processes in the case of a thick barrier. In such a system, the barrier states provide a conductance channel when the barrier becomes too thick to allow appreciable tunneling current. The solid line in Figure 4.14b shows the result of modeling this system as two resistors in parallel. One resistor, corresponding to the barrier states, is independent of C-H cycle number with a value of $R_0 = 5500\ \Omega$. The other component, corresponding to the tunneling current, is modeled as a resistor with exponential dependence on C-H cycle number. The model fits the data well, lending credence to this interpretation.

To extract an estimation of the barrier height from this analysis, we recall Equation 2.5 and may write

$$R \times A \propto \exp\left(-2d\sqrt{\left(\frac{2mU}{\hbar^2}\right)}\right), \tag{4.1}$$

where d is the thickness of the barrier, m is the electron mass and U is the height of the barrier in eV. From TEM data, we know that applying 14 C-H cycles gives a barrier thickness of ~5 nm. Thus, the thickness per cycle, t, is given by $t \cong 0.36$ nm/cycle and we have

$$R \times A \propto \exp\left(-2tx\sqrt{\left(\frac{2mU}{\hbar^2}\right)}\right), \tag{4.2}$$

where x is the number of C-H cycles. Thus, if we compare the exponent above to the plot of Log(R × A), we find

$$U = \left(\frac{\hbar}{2\alpha t\sqrt{2m}}\right)^2, \tag{4.3}$$

where α is taken from the fit in Figure 4.14. According to the fit, we have $\alpha = 0.57$ cycles. Thus, our estimation of the barrier height yields $U = 0.24$ eV.

Though the pressed indium contacts are effective for studying the effect of C-H cycle number on the tunneling barrier, junctions fabricated using these counter-electrodes typically exhibit broader, less pronounced conductance characteristics than do measurements using silver paste or evaporated silver counter electrodes. This will be explored further in Chapter 5.

4.3 References

1. H. Aubin, L.H. Greene, S. Jian, and D.G. Hinks, Phys. Rev. Lett. **89,** 177001 (2002).
2. C.C. Chang, X.D. DWu, R. Ramesh, X.X. Xi, T.S. Ravi, T. Venkatesan, D.M. Hwang, R.E. Muenchausen, S. Foltyn, and N.S. Nogar, Appl. Phys. Lett. **57,** 1814 (1990).
3. B. Wuyts, Z.X. Gao, S. SLibbrecht, M. Maenhoudt, E. Osquiguil, and Y. Bruynseraede, Physica C. **203,** 235 (1992).
4. Z. Han, T.I. Selinder, and U. Helmersson, J. Appl. Phys. **75,** 2020 (1994).
5. J.-P. Locquet, Y. Jaccard, C. Gerber, and E. Maechler, Appl. Phys. Lett. **63,** 1426 (1993).
6. S. Proyer, E. Stangl, M. Borz, B. Hellebrand, and D. Bauerle, Physica C. **251,** 1 (1996).
7. J.P. Gong, M. Kawasaki, K. Fujito, R. Tsuchiya, M. Yoshimoto, and H. Koinuma, Phys. Rev. B. **50,** 49 (1994).
8. K. Verbist, A.L. Vasiliev, and G. Van Tendeloo, Appl. Phys. Lett. **66,** 1424 (1995).
9. B. Schulte, M. Maul, P. Haussler, and H. Adrian, Appl. Phys. Lett. **62,** 633 (1993).
10. C.-H. Kim, I.-T. Kim, K.-S. Hong, and T.-S. Hahn, Supercond. Sci. Technol. **14,** 66 (2001).
11. R. Krupke, Z. Barkay, and G. Deutscher, Physica C. **315,** 99 (1999).
12. S.K.H. Lam, Physica C. **370,** 79 (2002).
13. M. Covington, R. Scheurer, K. Bloom, and L.H. Greene, Appl. Phys. Lett. **68,** 1717 (1996).
14. G. Westwood, in *Chemistry*. 2004, University of Illinois: Urbana-Champaign.
15. J.R. Waldram, *Superconductivity of Metals and Cuprates*. 1996, London: IOP Puplishing, Ltd. p. 223.
16. L.H. Greene and B.G. Bagley, in *Physical Properties of High Temperature Superconductors II*, D.M. Ginsberg, Editor. 1990, World Scientific: Singapore. p. 509.
17. K. Nagata, S. Uehara, A. Matsuda, and H. Takayangi, iEEE Trans. Magn. **17,** 771 (1981).

Chapter 5

Tunneling Measurements

The tunneling conductance measurements are performed in the standard four-probe configuration, as shown in Figure 3.5, with the positive contacts (current and voltage) on the YBCO thin film and the negative contacts on the counter electrodes. Thus, positive bias in our experiments probes the filled quasiparticle states in the YBCO. Hundreds of junctions were fabricated. Artificial barrier fabrication on YBCO is not a common junction fabrication technique. In particular, this zirconia-based solution-deposition technique is unprecedented for tunneling insulator applications. Consequently, an extensive effort was required to optimize the process and a large number of the junctions were not produced under optimized conditions for the YBCO thin film, the zirconia insulator or both. The numbers reported for the reproducibility at each orientation represent the number of high quality junctions at each orientation out of the total number fabricated at that orientation, and not necessarily under optimal conditions. Comments are given in greater detail on the reproducibility of junctions fabricated on (110)-oriented YBCO, since more data was acquired at that orientation after the junction fabrication process had been optimized.

Conductance measurements are made on YBCO thin films of four different crystallographic orientations. In three of these orientations, *i.e.*, (103)-, (100)- and (110)-oriented YBCO, all or part of the quasiparticle tunneling trajectory is along the CuO_2 planes. In the fourth, (001)-oriented YBCO, quasiparticles tunnel perpendicular to the planes (Figure 5.1). Thus, we find similar tunneling characteristics in these *ab*-plane orientations, but several differences are noted.

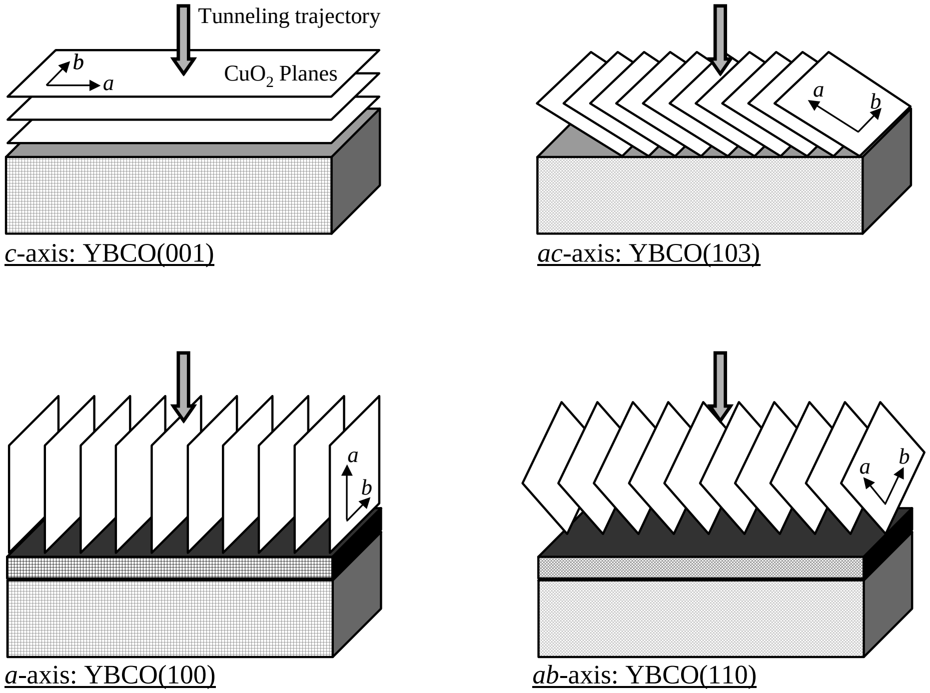

c-axis: YBCO(001)
ac-axis: YBCO(103)
a-axis: YBCO(100)
ab-axis: YBCO(110)

Figure 5.1. The nominal direction of the tunneling trajectory is shown for four crystallographic orientations of YBCO thin films. In all but *c*-axis tunneling, a component of the quasiparticle trajectory is along the CuO$_2$ planes.

5.1 Sharpness

The tunneling characteristics we observe on junctions fabricated with zirconia insulators are sharper than what is measured using other junction fabrication techniques. The term “sharper” is used qualitatively when compared to data from other groups. It is difficult to compare to the literature since normalization is required to extract the values to quantify sharpness and typically, the data are not presented over a broad enough range of voltages to perform the normalization. We demonstrate sharpness compared to other junction fabrication techniques by comparing the data shown in Figure 5.2. A well-defined feature observed in all high-quality junctions is the gap-like feature at negative bias (GLF_L). To extract the sharpness, the data are first normalized as described in Section 5.2. The sharpness is then defined as the magnitude of the GLF_L (measured from unity) divided by the FWHM of the GLF_L. Junctions fabricated using solution-deposited zirconia insulators are compared to junctions fabricated by direct evaporation of bismuth onto bare YBCO of two different crystallographic orientations.

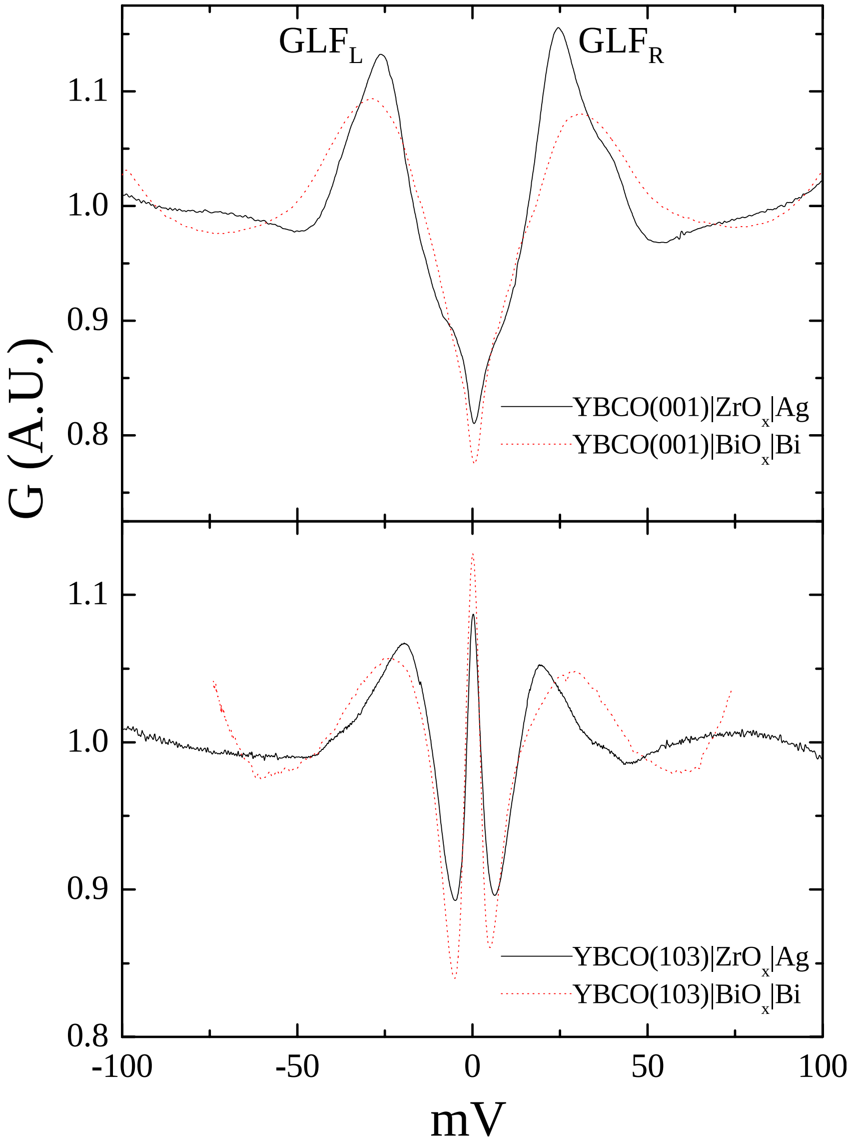

Figure 5.2. Normalized conductance data of junctions fabricated with solution-deposited zirconia tunneling barriers (solid line) compared to those fabricated by direct evaporation of bismuth onto uncoated YBCO (dotted lines) for (001)-oriented YBCO (top) and (103)-oriented YBCO (bottom). The zirconia-coated films consistently exhibit sharper features in the conductance curves. The data are normalized by a quartic fit as described below.

Average sharpness values and FWHM of the GLF_L for the orientations and barrier types in Figure 5.2 are shown in Table 5.1. Three junctions for each combination of barrier type and orientation are used to calculate the average sharpness and standard deviation, σ, except for the values for BiO_x(103), which is calculated from two junctions. The zirconia-based junctions consistently show higher sharpness and narrower GLFs.

Barrier Type	Sharpness (eV^{-1})	σ (eV^{-1})	FWHM (eV)	σ (eV)
ZrO_x(001)	0.0702	0.00522	16.15	1.10
BiO_x(001)	0.0462	0.00312	21.85	0.349
ZrO_x(103)	0.0701	0.00405	15.42	0.985
BiO_x(103)	0.0565	0.000259	18.85	0.05

Table 5.1. Sharpness values along with the standard deviation, σ, extracted from several planar tunnel junctions on YBCO. Three junctions of each barrier type were used for the calculations, except for the sharpness for BiO_x(103), which was calculated from two junctions. Junctions fabricated using zirconia barriers routinely exhibit higher sharpness. The values for the FWHM of the negative bias GLFs and associated standard deviations are also shown.

5.2 Normalization: Removing the Background

As described in Section 2.1, asymmetry and voltage-dependence of the tunneling barrier leads to the parabolic conductance background shown in Equation 2.8. Nonlinear backgrounds (U-shaped or V-shaped) are observed in all planar tunneling measurements on YBCO. For example, the data shown in Figure 5.2 are shown unnormalized in Figure 5.3. The background in each data set is not a constant, but neither is it strictly parabolic. Thus, to extract the DoS characteristics, especially in junctions with larger magnitude variations in the background, such as the junctions fabricated with BiO_x barriers in Figure 5.3, a normalization scheme is required.

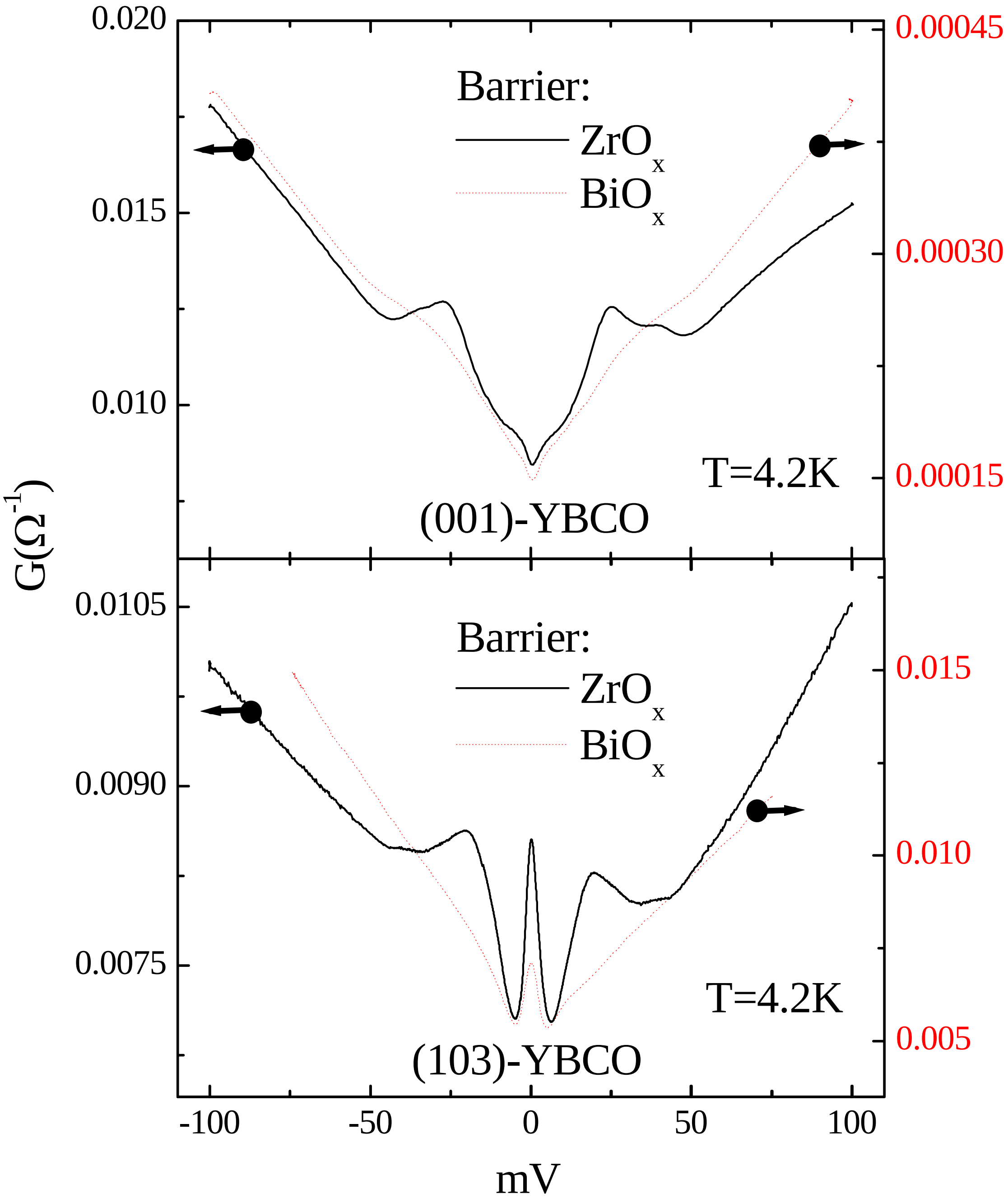

Figure 5.3. The same data as shown in the previous Figure, here unnormalized. Data from junctions with sharp conductance characteristics typically show background shapes that are nearly linear at high bias. Data from (001)-oriented YBCO sometimes shows negative curvature at high bias, as is seen in zirconia-based junction shown here.

Since various shapes of the background are seen for different types of junctions, a sufficiently general normalization technique must be developed to be applicable to all data, so that comparisons can be made. One technique involves fitting the background with the original data, convolved with the derivative of the Fermi population function, *df(eV,T)/d(eV)*, evaluated at high temperature. As seen in Equation 2.10, in the case of a normal metal-insulator-superconductor junction, the measured conductance is given (within a constant) by the superconducting DoS, convolved with *df(eV,T)/d(eV)* evaluated at the measurement temperature. Thus, to simulate data at higher temperature, T_{high}, assuming there are no DoS changes, one can deconvolve *df(eV,T)/d(eV)* evaluated at the measurement temperature from the measured data and convolve the result with *df(eV,T)/d(eV)* evaluated at T_{high}. If T_{high} is sufficiently high, so that no DoS features are present, the convolved data can be used to remove the background from the original low-temperature data.

However, this technique presents several problems. Deconvolution is not a trivial task, but it can be simplified using the convolution theorem:

$$f \otimes g = \tilde{f} \times \tilde{g} \text{, where} \tag{5.1}$$

$$\tilde{f}(\omega) = \int_{-\infty}^{\infty} f(t) e^{i\omega t} dt \,, \tag{5.2}$$

i.e., the Fourier transform of f. Thus, by using the fast Fourier transform (FFT) algorithm and dividing the FFT of the original data by the FFT of *df(eV,T)/d(eV)*, deconvolution can be performed. Even using this technique, however, discrete sampling of the data presents problems and performing the analysis can be a challenge.

Other, more fundamental problems also exist. Due to the large scale of the features in the conductance spectra of YBCO, and to the sharpness of the features we measure, the T_{high} required to remove all DoS features can be well above T_c. Due to the nature of convolution as a "mixing" operation, the data within the width of $df(eV,T)/d(eV)$ (~3.5 k_BT_c [1]) of each end of the data range is not usable for background removal, and some data at high bias is lost. Furthermore, the shape of the background has an effect on the resultant convolved curve. Equation 2.10 describes the convolution with the DoS only, not the background. Convolution in the presence of the background in the data causes a transfer of spectral weight from the high conductance values at high bias to low bias in the calculated background. So, although the convolution technique is convenient in some cases, it has no physical basis for estimating the shape of the background and using it can complicate the analysis. Both the edge effects and the effects of shifted spectral weight are seen in Figure 5.4a in the data convolved to 300K. Note the data convolved even to 300 K (well above T_c) contain a remnant of the negative bias GLF.

Another technique commonly used for normalization is to divide the low temperature data by measured data taken at high temperature, preferably above T_c, so that the effects of the superconducting DoS are absent. This is an effective technique for low-T_c superconductors, for which the necessary normalization temperature is only a few degrees above the measurement temperature. To normalize low-temperature data taken on high-T_c materials, however, the difference between the low-temperature data and normalization data is on the order of 100 K. Over this temperature span, significant changes in the background shape, drifts in the electronics, or structural changes in the junction can make it impossible to use the high-temperature data as a background. Large changes in the background that are sometimes observed at T_c can be avoided in the background if data is taken just below T_c, since at this temperature, superconducting DoS features are often invisible. However, in sufficiently sharp data, as has been produced by zirconia-based junctions, the DoS features are evident as little as 1 K below T_c. In the absence of any of these effects, however, this technique can be very effective, and is the preferable method.

If minor shifts in the high-temperature background are observed, they can be corrected by modeling the shift not as a simple offset but as an extra resistance in series with the junction. In this case, minor shifts and shape changes are often corrected. This is shown for data taken at 77 K in Figure 5.4b. In this case, however, the use of this data as an effective background is impossible due to noise in the data and the persistence of superconducting DoS features at this temperature.

Though the high-temperature data fitting is preferable, it is often impossible, as described above. The normalization technique used most often in this work is always applicable, given a wide enough data range. This technique involves a polynomial fit to the data using a fourth-order, or quartic polynomial. The quartic fit is a technically simple method that accommodates the full range of background shapes observed in our measurements and is capable of being used to fit data at any temperature, crystallographic orientation, etc. A large range of data ($|\pm V_{max}| \gtrsim 75$ meV) is required because it is best to avoid the low-bias superconducting DoS when making the fit. The low-bias (-35 meV $\lesssim V \lesssim 35$ meV) region is removed when making the fit so that higher-order terms in the polynomial do not make too strong a contribution. The efficacy of this method in fitting low-temperature data is shown in Figure 5.4c. The disadvantage of this technique is that it lacks the physical motivation of the high-temperature fitting method. No physical basis is known for fitting the background to a fourth-order polynomial, but the versatility of this technique enables the comparison of many different conductance curves.

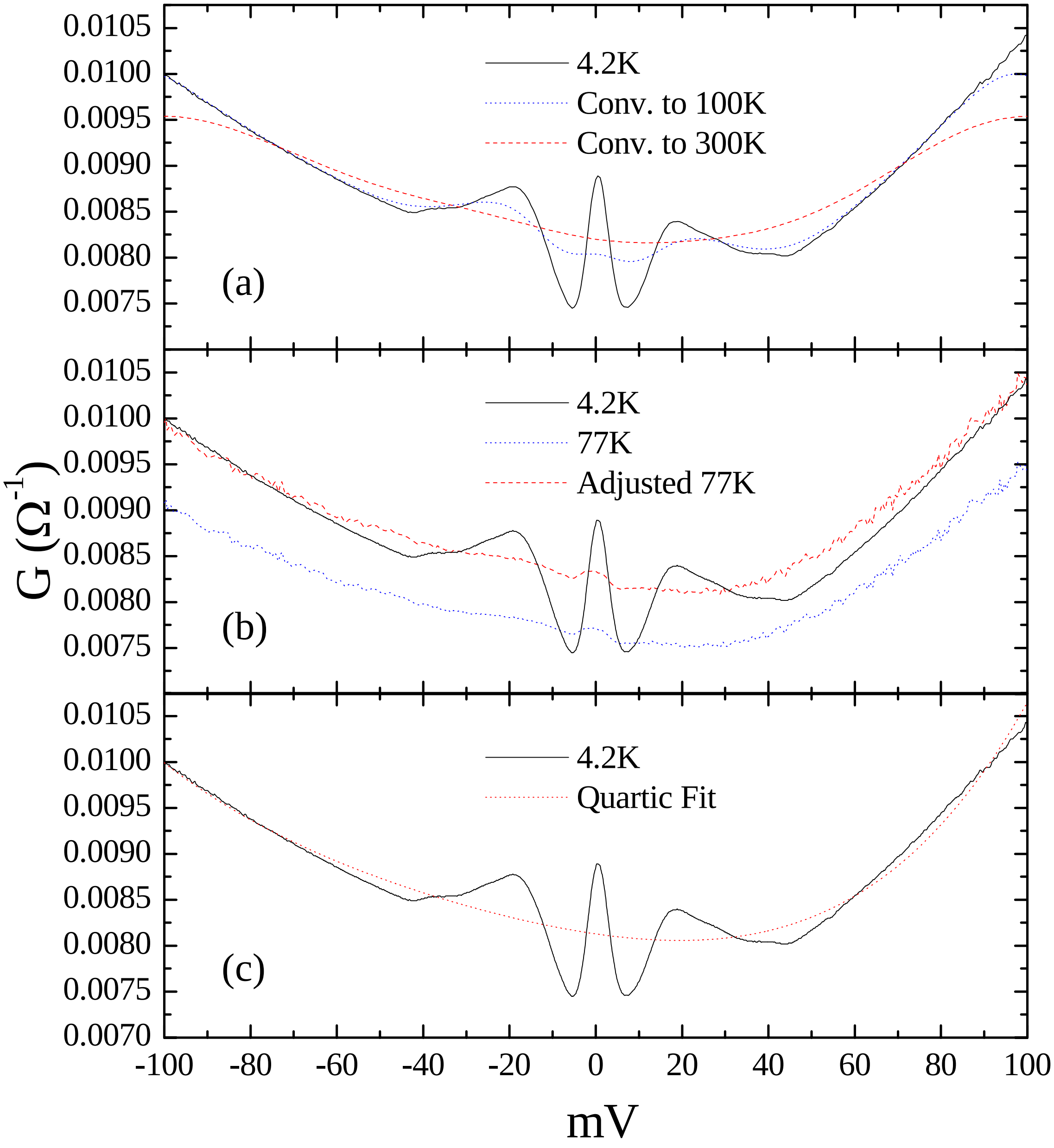

Figure 5.4. Three different techniques are used to fit the background of tunneling conductance data from (103)-oriented YBCO. High-temperature convolution (a) can produce edge effects and features DoS features can survive in data convolved even to 300 K. High-Temperature data fitting (b) provides the most physically justifiable technique but several factors, including noise and DoS features persisting to 77 K make this data unsuitable. Minor shifts in data can be corrected (dashed line) by modeling the shift as a series resistor, as described in the text. Quartic polynomial fitting (c) is a versatile technique and produces an excellent fit.

5.3 (001)-Oriented YBCO

Statistics: (001)

The sharpness required to exhibit features in the “Observed Characteristics” section below was observed on five junctions out of 85 total fabricated on (001)-oriented YBCO, yielding a total reproducibility at this orientation of ~6 %. Unsuccessful junctions typically show results indicative of insulating barriers that are too thick or too thin. Barriers that are too thick show increasing junction resistance with decreasing temperature (semiconductor-like behavior) and a roughly parabolic, but otherwise featureless, conductance curve. Quasiparticle transport in this case is likely due primarily to multi-step tunneling via localized electronic states in the barrier, since the barrier potential is too great for appreciable single-step tunneling, as described in Section 4.2. Since single-step transport is not dominant, the features in the superconducting quasiparticle DoS are not readily observed.

Conductance characteristics from barriers that are too thin show features (peaks and valleys) sharper than the width of the derivative of the Fermi function, indicating that non-tunneling transport processes are present, and are likely due to Cooper pair transport. These processes are allowed if pinholes in the barrier cause direct contact between the superconductor and the counter-electrode and superconductivity is induced in the counter-electrode by the proximity effect. A slight increase is expected in the measured conductance as the junction is cooled through the T_c of the film. The magnitude of this effect depends on the value of the junction resistance compared to the film resistance, as the two resistances are effectively in series. Except for this effect, the overall conductance measured in single-step elastic tunneling should be temperature independent. Junctions with too thin barriers show an increase in the overall conductance with decreasing temperature (metallic behavior). Examples of the characteristics produced by these different types of junctions are shown in Figure 5.5.

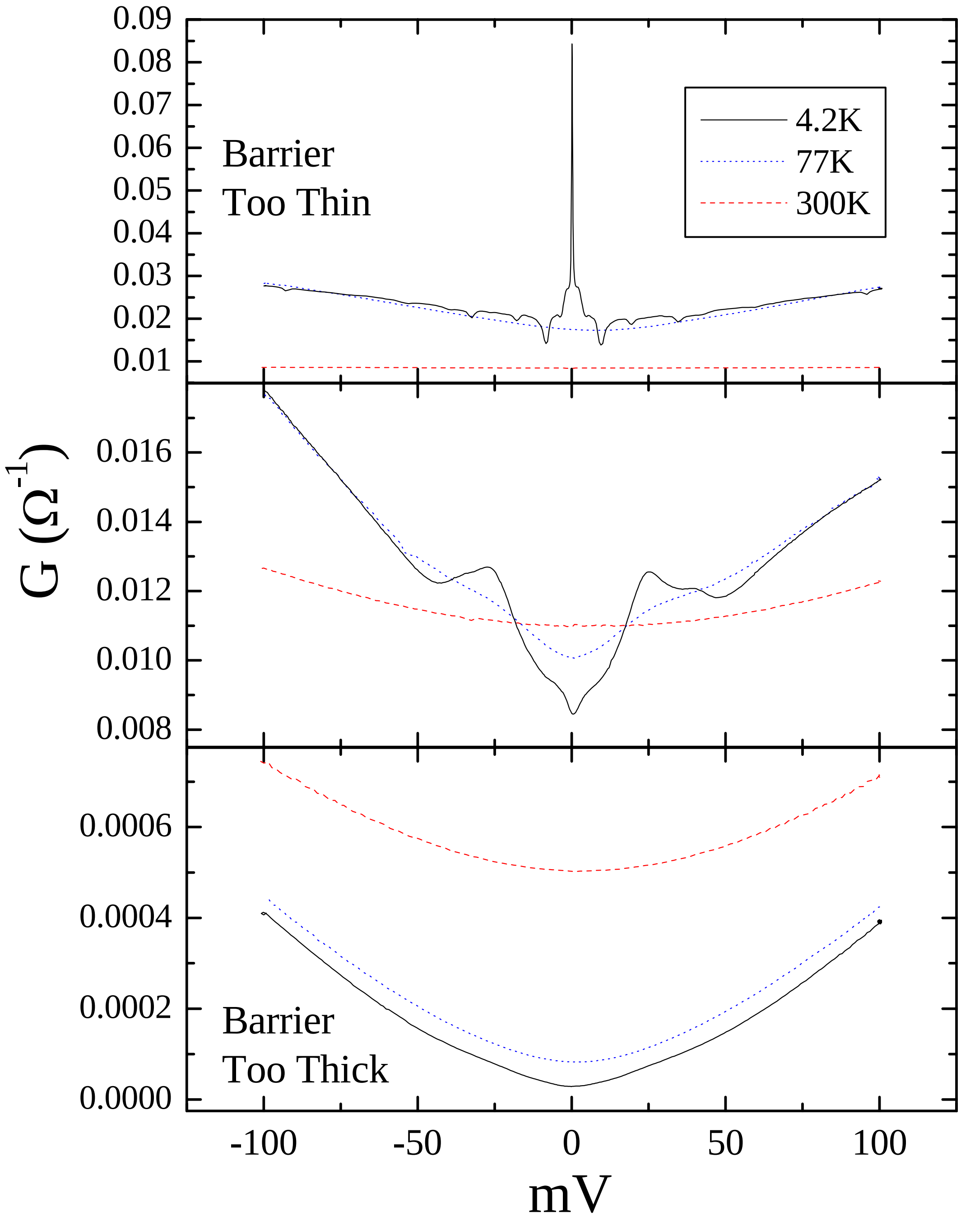

Figure 5.5. Examples of conductance characteristics observed for different types of zirconia barriers on (001)-oriented YBCO thin films. Junctions with too thin barriers or with pinholes (top panel) show an increasing conductance with decreasing temperature (metallic behavior) and exhibit sharp, supercurrent features. Junctions with too thick barriers exhibit decreasing conductance with decreasing temperature (semiconductor behavior). Single-step, elastic tunneling should show little or no temperature dependence of the overall conductance (middle panel).

Observed Characteristics: (001)

Gap-like features (GLF) defined as a quasi-symmetric enhancement of the conductance away from zero bias, are measured in all four orientations shown in this work. These features are observed at the largest energy value in (001)-oriented YBCO. In addition to the GLF, a double-peak structure is exhibited in this gap edge region. The positions of the double-peaks are determined by taking two numerical derivatives of the conductance data and locating the minima (Figure 5.6). These features are observed more prominently on the positive bias side than the negative bias, such that the negative-bias doublet are often only detectable in the derivative spectra.

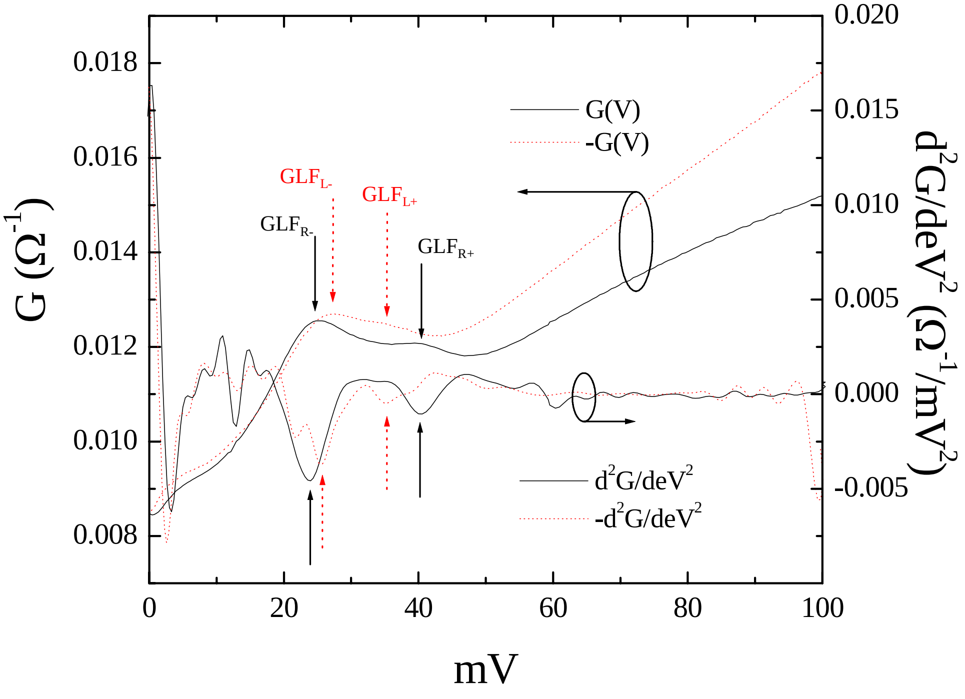

Figure 5.6. Conductance data (left scale) and the second derivative of the conductance (right scale) for a (001)-oriented YBCO tunnel junction. The positive bias (solid lines) and negative bias (dotted lines) data are plotted on the same side to emphasize the asymmetry in the background and positions of the double-peak structures. The spacing between the positive doublets is always larger and is always located “outside” the negative doublets. The second derivative of the conductance is used to locate the positions of the peaks.

As can be seen in the data in Figure 5.6, the spacing between positive doublets is greater than that of the negative doublets. We find this is always the case. Furthermore, the value of the low-energy component of the positive-bias pair (GLF_{R-}) is always less than the absolute value of the low-energy component of the negative-bias pair (GLF_{L-}), while the value of the higher-energy component of the positive bias pair (GLF_{R+}) is always greater than the absolute value of the corresponding negative bias component (GLF_{L+}) (see Figure 5.6). Thus, we say the positive doublets are always "outside" the negative doublets. The average value for the GLFs and the spacings between the doublets (ΔGLF) are shown in Table 5.2, along with the standard deviations. The data are averaged from five different (001)-oriented YBCO junctions.

Another prominent feature commonly observed in (001)-oriented YBCO junctions is the zero-bias conductance dip (ZBCD). This feature appears as a suppression in the zero-bias conductance starting at shoulders ($ZBCD_+$ and $ZBCD_-$) in the data observed at ± 3–4 meV. The average values of the ZBCD shoulders along with the standard deviations are shown in Table 5.2.

Table 5.2. Average values and standard deviations for the spectral features measured on (001)-oriented YBCO tunnel junctions. The data were calculated from values taken from five different (001)-oriented junctions.

	GLF_{R+}	GLF_{R-}	ΔGLF_R	GLF_{L+}	GLF_{L-}	ΔGLF_L	$ZBCD_+$	$ZBCD_+$
Value (eV)	39.5	23.8	15.7	-34.9	26.0	8.9	3.9	-3.3
σ (eV)	0.59	0.91	1.03	1.52	0.72	1.28	0.66	0.68

The temperature dependence of the ZBCD seems to indicate that the ZBCD could be a dynamic element of the DoS in (001)-oriented YBCO films. The data in Figure 5.7 are examples of data normalized using the high-temperature data method. In this case, the data are normalized by the 95K data, just above T_c. The figure also shows the result of convolving the 5K data with $df(eV,T)/d(eV)$ at each temperature. What is observed is that the ZBCD disappears faster in the measured data than in the calculated data at low temperature (5–25 K). At higher temperatures, however ($T \geq 30$ K) we see increasing deviations from the calculated data inside and outside the gap. The high-temperature behavior exhibits the type of dynamics expected for a closing superconducting gap as the temperature approaches T_c, but the low-temperature dynamics displayed by the ZBCD are unexpected.

Due to the decoupling of the CuO_2 planes in YBCO, the Fermi surface is quasi two-dimensional, having a corrugated cylindrical shape with the cylinder axis running along the *c*-axis direction [2]. Since tunneling in the *c*-axis direction does not probe the CuO_2 planes directly, there is no real Fermi surface into which to tunnel. Therefore, *c*-axis tunneling is poorly understood. The linear background often measured at this orientation has been attributed to inelastic scattering [3], rather than to DoS effects.

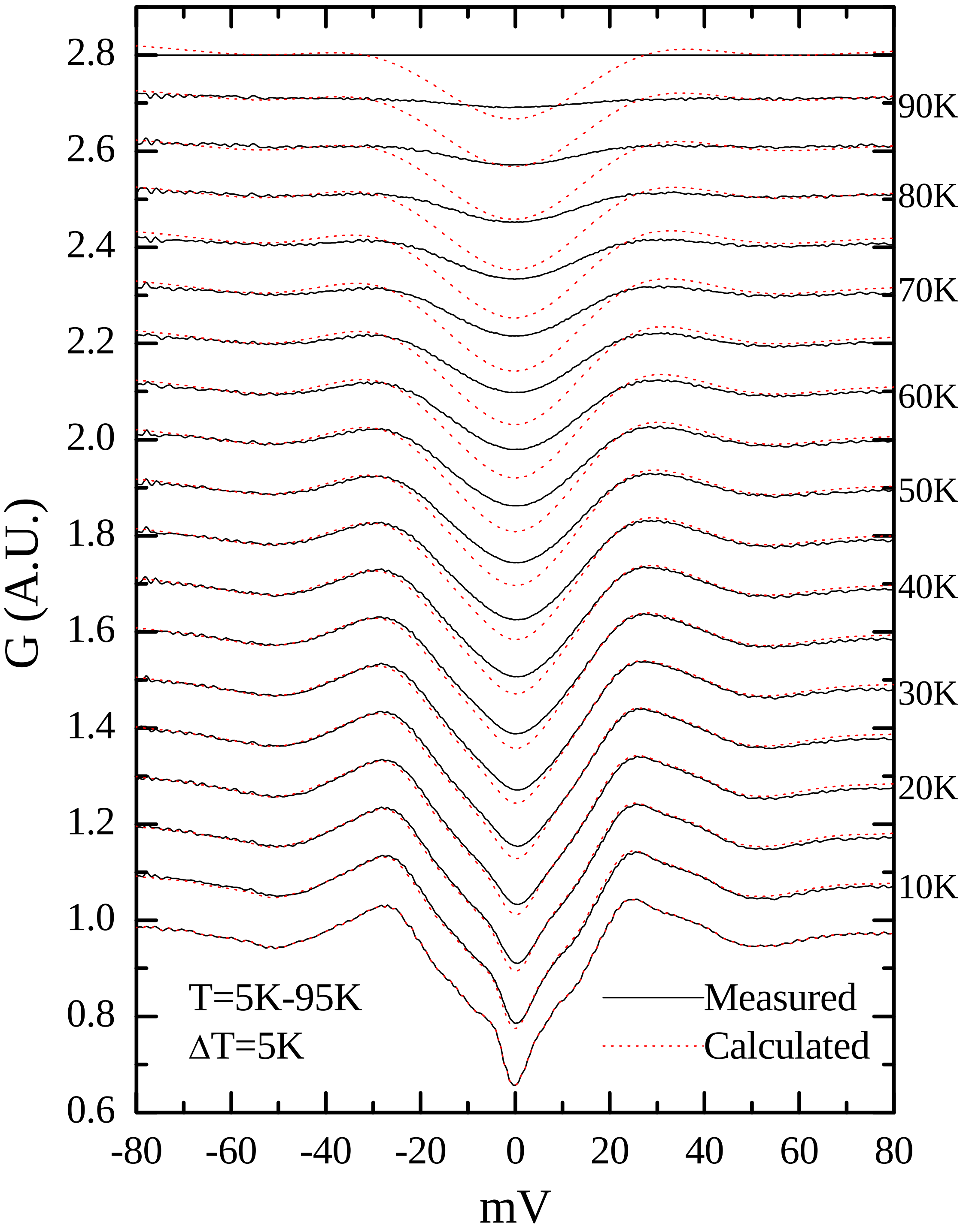

Figure 5.7. Temperature dependence of conductance data (solid lines) from (001)-oriented YBCO thin films from 5 K to 95 K. The data is normalized by the data at 95 K and are offset for clarity. The dotted lines show the result of convolving the 5K data with *df(eV,T)/d(eV)* at the higher temperature. Comparing the measured to calculated data suggests a possible low-temperature dynamics in the dependence of the ZBCD.

It is evident from analysis of the temperature dependent data in Figure 5.8 that there is DoS activity outside the GLF. Since DoS must be conserved, as temperature is increased, spectral weight lost at one value of energy must be gained at another. This means that there exists a constant or "baseline" that can be subtracted from the normalized conductance data such that integration of the resulting data equals zero. That is, the area above the baseline is equal to the area below for all temperatures. What is found in the data in Figure 5.8 is that the position of baseline required for the area above and below to be equal corresponds roughly to the value of the dip outside the GLF at ± ~50 meV in the conductance spectra. What this means is that the spectral weight outside the GLF is required for the total area above and below the baseline to equal zero.

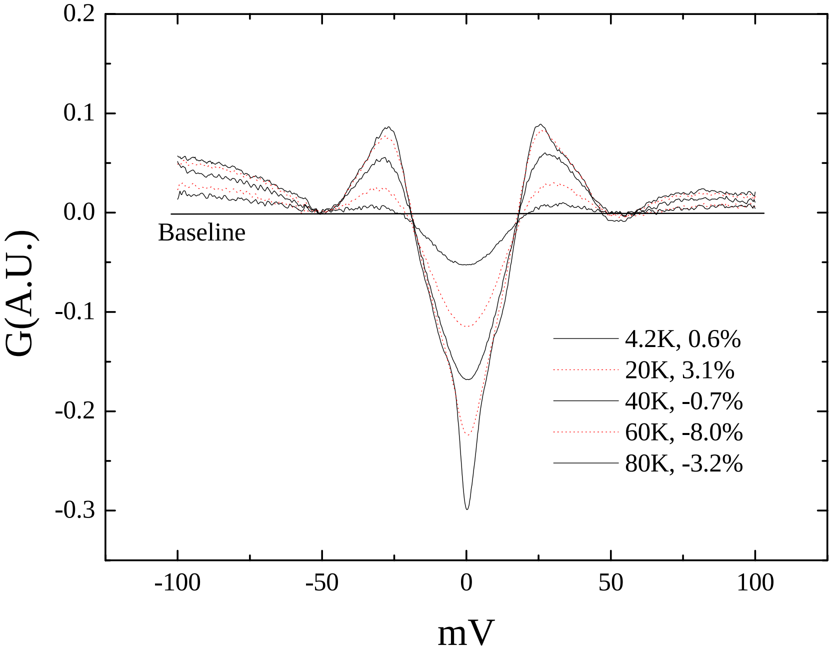

Figure 5.8. Normalized (quartic fit) and baseline-subtracted data from (001)-oriented YBCO junctions at various temperatures. The baseline shown indicates the value of the data for which area above and below the baseline is equal, indicating conservation of DoS. The percent deviation from zero in the area for each curve is indicated in the legend.

This shows that the extra spectral weight in the DoS needed to conserve states lies far outside the GLF, indicating changes in the superconducting quasiparticle DoS in this region. This does not mean, however, that the baseline ascertained by this method is the true baseline, however, since additional DoS spectral weight is likely to exist outside the measured region, especially considering the observed temperature dependence of the conductance at ± 100 meV. These features outside the GLF are reminiscent of similar DoS activity in the "peak-dip-hump" structure measured in ARPES data [4]. This does not rule out inelastic scattering leading to a linear background in at this orientation, but in these sharply-featured junctions, we observe negative curvature in the background to ± 100 meV so that if a linear background is present, it would be recovered outside this range.

5.4 (100)-Oriented YBCO

Statistics: (100)

As in the case of junctions fabricated on (001)-oriented YBCO, tunneling conductance measurements on (100)-oriented YBCO were performed during the insulator and thin film optimization process. Consequently, the reproducibility at this orientation is low. Junctions were fabricated on (100)-oriented YBCO thin films from six separate growth batches. Four of those films were processed with numbers of C-H cycles in the range of 8 to 12. All of the evaporated silver electrode junctions fabricated on these films exhibited conductance characteristics indicative of metallic shorts in the barrier. Two silver paste junctions on one of these films (processed with 8 C-H cycles) showed the weak temperature dependence indicative of single-step elastic tunneling but poor contacts produced significant noise in one junction. The other two films were processed with 14

C-H cycles. There were 11 viable junctions and four of these were successful: two with evaporated silver counter electrodes, two with silver paint counter electrodes, and one of each type on each film. However, both films showed a majority of c-axis crystalline phases by SEM and XRD.

Observed Characteristics: (100)

The results of the evaporated silver junctions are shown in Figure 5.9a. GLFs are observed in these data, with the energy values and sharpness values shown in the figure. The sharpness for these characteristics is lower in these data compared to data listed in Table 5.1 from other junctions fabricated with zirconia barriers. No double-peak structure is observed, though noise in the data would make detection of peak doublets difficult. A ZBCP is observed in one of the data sets but not in the other.

The data observed on the same films with silver paste counter electrodes (Figure 5.9b) are strikingly different from those observed with evaporated electrodes. A prominent ZBCP is observed in both cases with lower energy values for the GLFs and higher sharpness values, comparable to the values listed for zirconia barriers in Table 5.1. The ZBCPs, while being more prominent in these junctions, also exhibit smaller values for the FWHM.

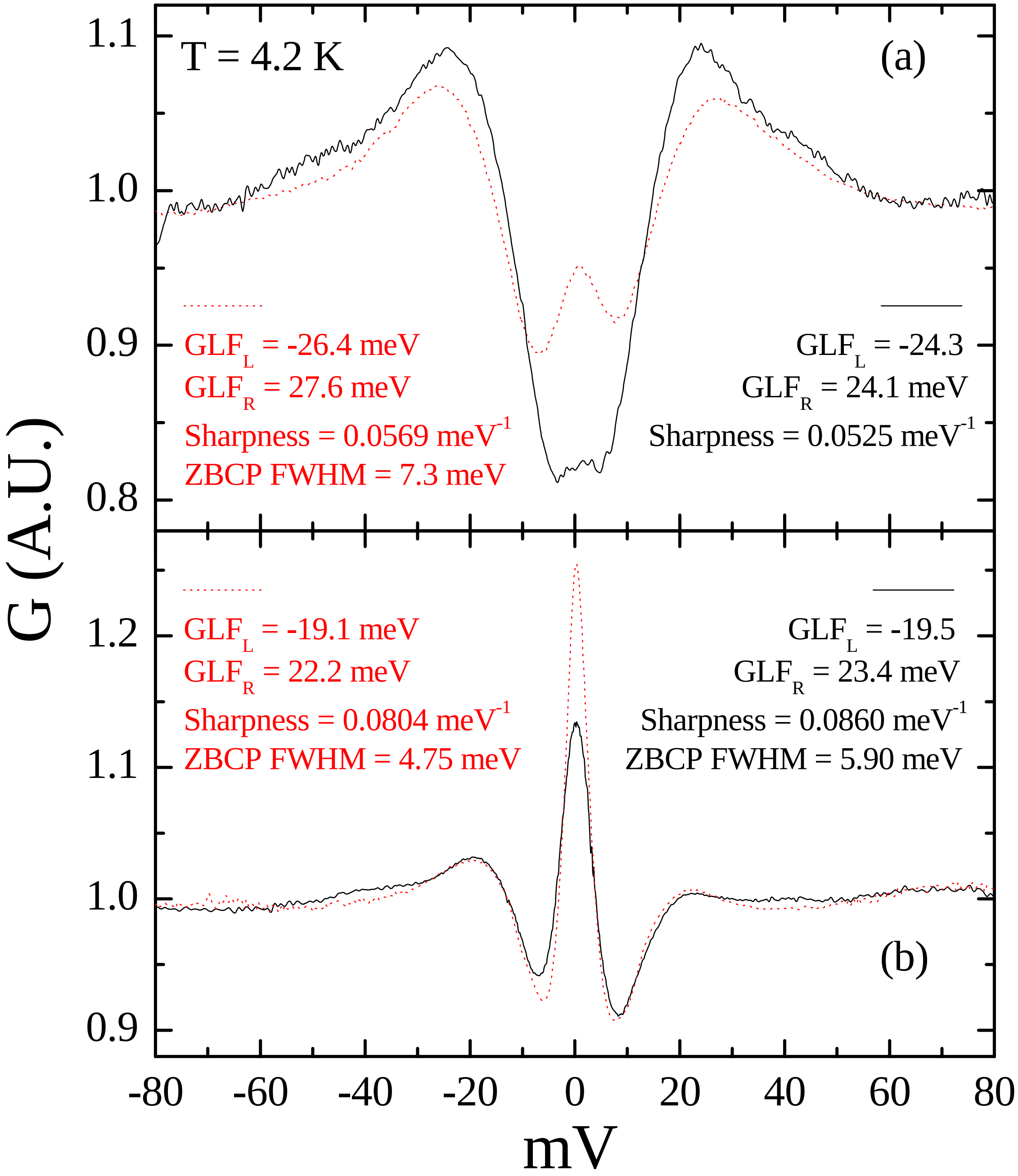

Figure 5.9. Tunneling conductance at 4.2 K of four zirconia-coated, (100)-oriented YBCO thin film junctions, two fabricated with evaporated silver counter electrodes (a) and two with silver paste counter electrodes (b). Energy values for the GLFs and sharpness values are presented for all curves. The FWHM of the ZBCP where applicable are also given. Junctions fabricated with silver paste counter electrodes show strikingly different features from those fabricated with evaporated silver, including more prominent ZBCPs, increased values of sharpness and lower GLF energy values. The data are normalized by a quartic fit.

The larger energy values of the GLFs and suppressed zero-bias conductance of the evaporated electrode junctions make these characteristics similar to characteristics observed on (001)-oriented YBCO thin films, suggesting that these junctions are probing the prominent *c*-axis phase present in these films. The junctions fabricated with silver paste counter electrodes show characteristics similar to junctions fabricated on the other two *ab*-plane orientations (namely, (103)- and (110)-oriented YBCO), as is shown in Sections 5.5 and 5.6.

A single successful silver paste junction was fabricated on a (100)-oriented YBCO film for which no *c*-axis phase was detected by SEM or XRD, *i.e.*, the surface and bulk of the film were pure (100)-oriented YBCO. The characteristics of this junction are shown in Figure 5.10. Though the data contains significant noise, and further experiments are needed to reproduce this result, it shows characteristics predicted for this orientation: no ZBCP and a larger value for the GLFs (GLF_L = -22.0). We also observe a shoulder structures inside the GLFs at -7.6 meV and 5.2 meV.

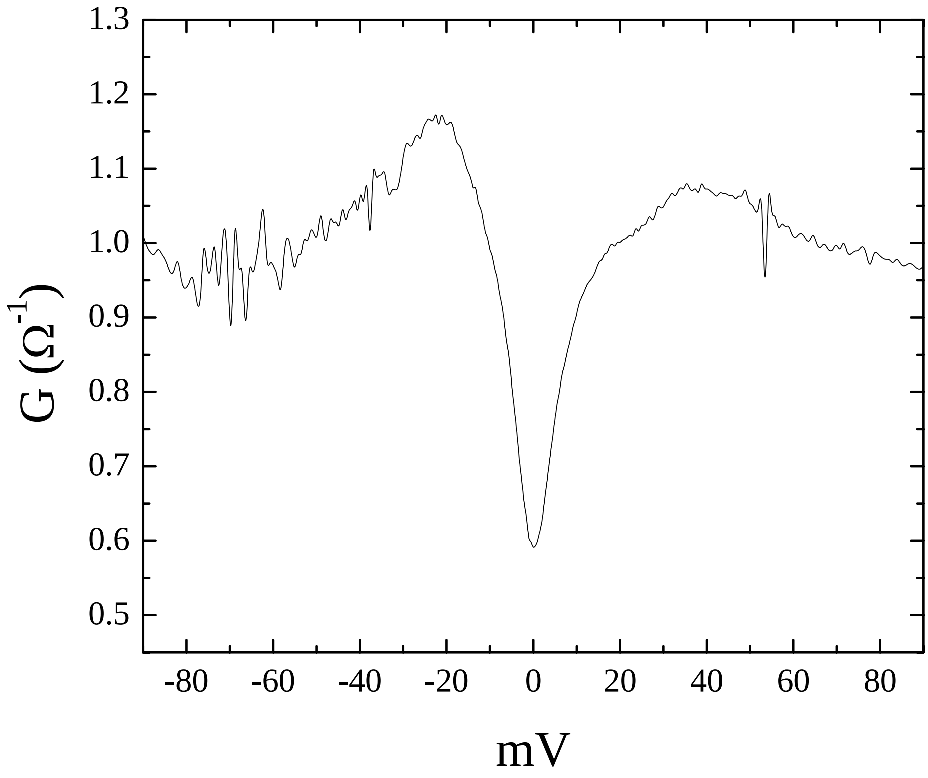

Figure 5.10. Tunneling conductance for a zirconia-coated, (100)-oriented YBCO thin film fabricated with a silver paste counter electrode. This is the only successful junction measured on a pure (100)-oriented YBCO thin film, as measured by SEM and XRD. Though the data need to be reproduced, the characteristics are closer to what is expected for this orientation: no ZBCP and a larger value for the GLF_L.

5.5 (103)-Oriented YBCO

Statistics: (103)

Evaporated silver counter electrodes were used to fabricate 76 junctions on (103)-oriented YBCO thin films. A total of 10 of these junctions showed the weak temperature dependence indicative of single-step elastic tunneling, giving a reproducibility for evaporated silver electrodes of 13 %. Silver paste counter electrodes were used to fabricate 31 junctions. In fact, more junctions were attempted but since silver paste electrodes are less robust to thermal cycling than evaporated electrodes, only 31 survived to be measured at cryogenic temperatures. Of those 31 junctions, 14 were successful, giving a reproducibility of 45 %.

Observed Characteristics: (103)

Observed characteristics for planar tunnel junctions fabricated with evaporated and silver paste counter electrodes on (103)-oriented YBCO thin films are shown in Figure 5.11. The conductance curves for (103)-oriented YBCO in Figures 5.2–5.4 are also from a junction using evaporated silver counter electrodes. Comparing those results to the results in Figure 5.11 shows the variation in results observed for evaporated electrodes. Junctions fabricated with silver paste electrodes showed less variation in results and are, in general, consistent with the results on (103)-oriented films shown in Figures 5.2–5.4. The data consistently show a pronounced ZBCP and $\mathrm{GLF_L}$. The evaporated silver junctions in Figure 5.11 do not show a pronounced positive-bias GLF. This is not uncommon and is the motivation behind choosing the $\mathrm{GLF_L}$ for analysis. This data also exhibits a shoulder (indicated by arrows) sometimes observed inside the GLF, this same feature is brought out in magnetic field dependent measurements on (110)-oriented YBCO films, as shown in Figure 5.14. Values for the GLFs and the FWHM of the ZBCP are given in Section 5.7.

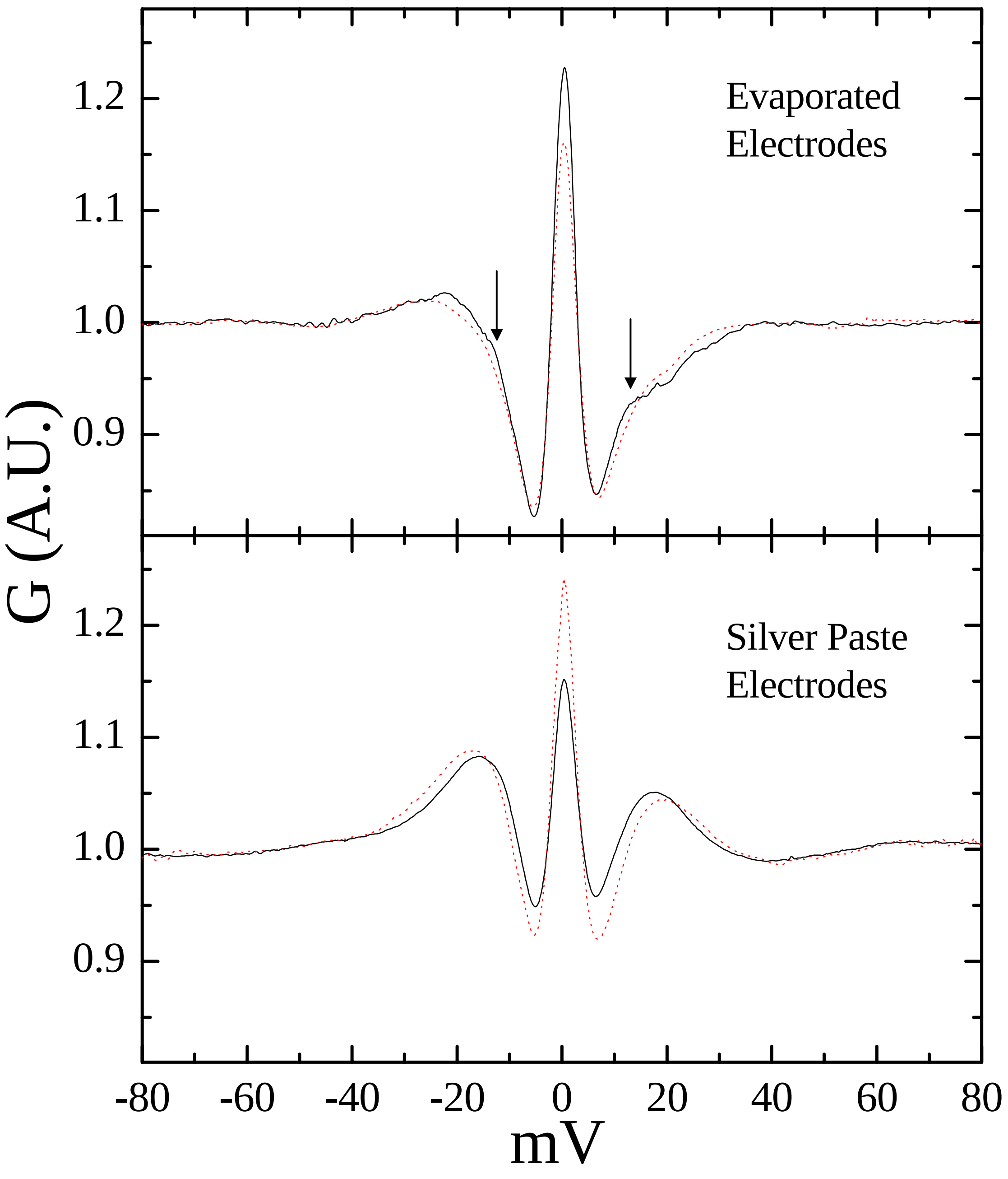

Figure 5.11. Representative tunneling conductance measurements of zirconia-coated, (103)-oriented YBCO thin films using evaporated silver and silver paste counter electrodes. The data from both techniques show typical features observed at this orientation: a prominent ZBCP and negative bias GLF all cases. The data from evaporated electrodes show variations from previous figures, including shoulders inside the GLFs at ± 13 meV, indicated with arrows. The data are normalized by a quartic fit.

5.6 (110)-Oriented YBCO

Statistics: (110)

Planar tunnel junctions on (110)-oriented YBCO thin films were fabricated using all three counter electrode deposition techniques described in Section 3.2. Of 60 viable junctions fabricated with evaporated silver counter electrodes, only three junctions (5 %) showed the temperature dependence indicative of single-step elastic tunneling. However, for silver paint counter-electrodes, 28 good junctions were observed out of 52 total, giving a reproducibility of 52 %. Furthermore, of the 52 total silver paste electrode junctions, 22 were made on optimized films and barriers, with between two and seven C-H cycles and of these, 18 were successful. Thus, the reproducibility on optimized films and barriers for silver paste counter-electrodes was 82 %.

The third counter electrode deposition method, the indium press technique, is a useful way to gain information about the barrier, as shown in Section 4.2, but the quality of the conductance characteristics measured in these junctions is typically less than in the other techniques. Of 22 junctions fabricated with pressed indium electrodes, five showed single-step elastic tunneling. All of the successful junctions were processed with between two and six C-H cycles. The total number of junctions fabricated in that range was 14, making the reproducibility 36 % in that optimal range.

Observed Characteristics: (110)

The nature of the characteristics observed with junctions using pressed indium counter electrodes is shown in Figure 5.12. The indium superconducting DoS is clearly observed at low bias in the 1.4 K data for the one-cycle and two-cycle cases. The temperature dependence of the overall conductance follows the same trend as in Figure 5.4: semiconductor-like temperature dependence for too thick barriers and metallic temperature dependence for too thin barriers. In this case, however, the “good” junction (two C-H cycles) exhibits broad features, common for pressed indium junctions on zirconia coated YBCO.

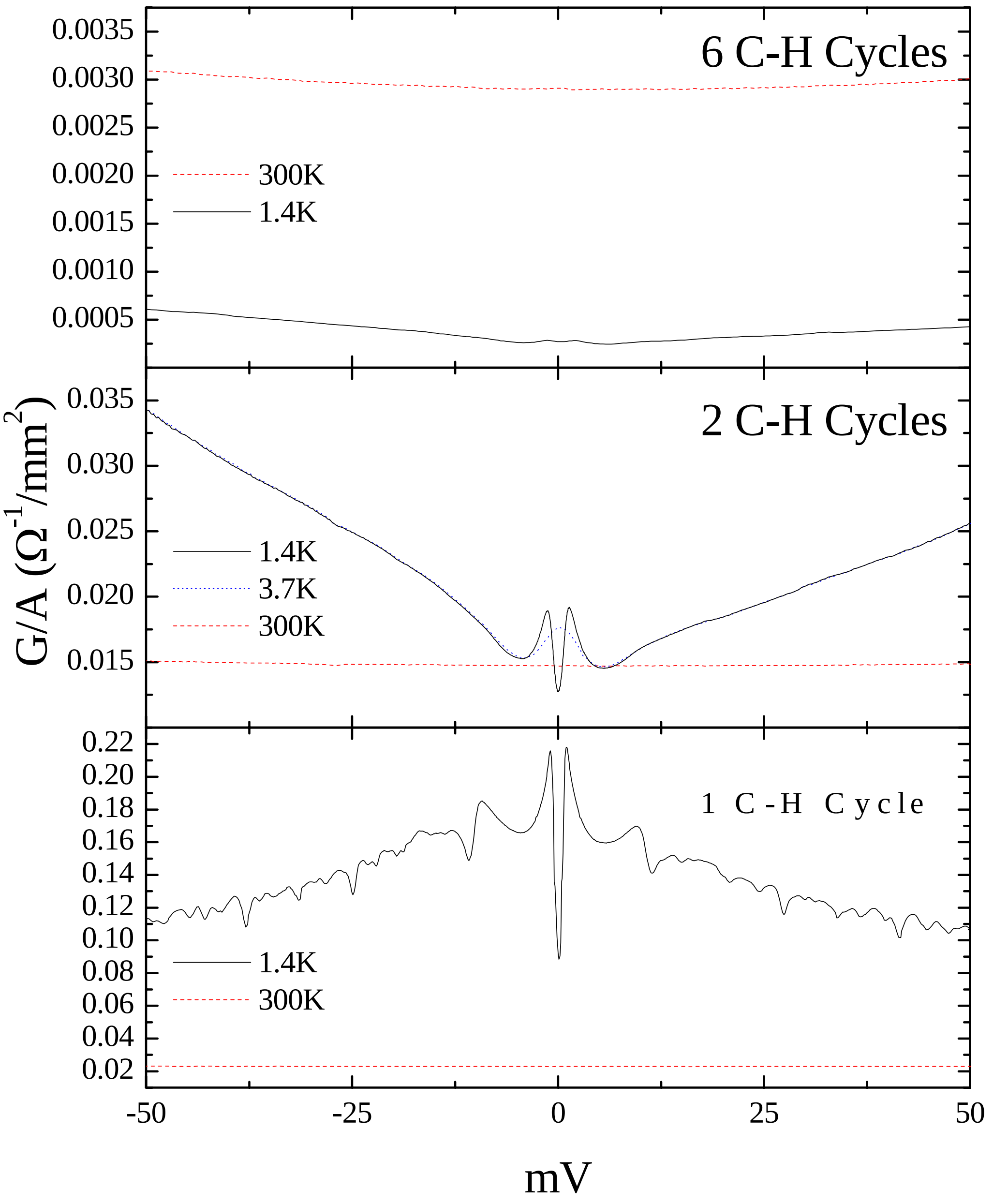

Figure 5.12. C-H cycle number dependence and temperature dependence of the tunneling conductance of junctions fabricated on zirconia-coated (110)-oriented YBCO thin films with pressed indium counter electrodes. The dependencies match those of the evaporated electrode junctions shown in Figure 5.5 but pressed indium electrodes exhibit weaker YBCO superconducting DoS features.

Typical characteristics for a junction fabricated with silver paste counter electrodes on (110)-oriented YBCO thin films are shown in Figure 5.13. Prominent GLFs are routinely observed at negative and positive bias, as is a prominent ZBCP. Values for the GLFs and ZBCP are given in Section 5.7.

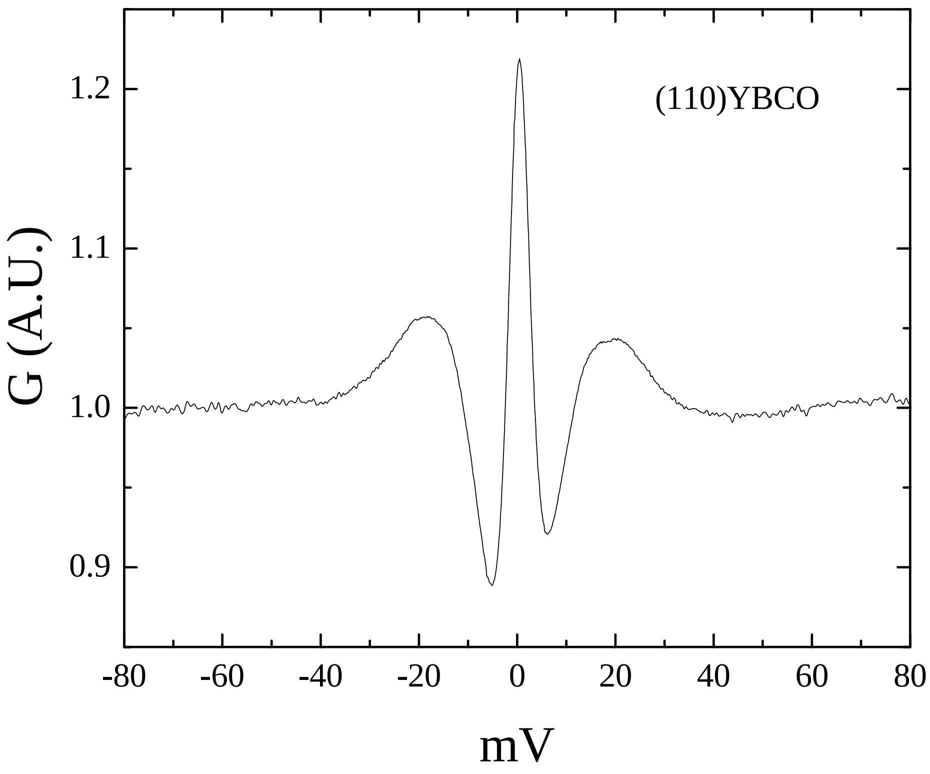

Figure 5.13. Typical characteristics for junctions fabricated with sliver paste counter electrodes on zirconia-coated (110)-oriented YBCO thin films, showing prominent GLFs and ZBCP. The data are normalized by a quartic fit.

In a few cases, shoulders in the conductance similar to those pointed out in Figure 5.11 were observed in junctions fabricated on (110)-oriented YBCO. Applying a magnetic field perpendicular to the CuO_2 planes has a strong effect on the tunneling DoS at this orientation, particularly on the ZBCP, as is explored further in Chapter 6. The GLFs are likewise suppressed by a field perpendicular to the planes but as the field-dependent data in Figure 5.14 show, the shoulder regions inside the GLFs are virtually unaffected by the field, even as the features around them (the GLFs and ZBCP) are suppressed.

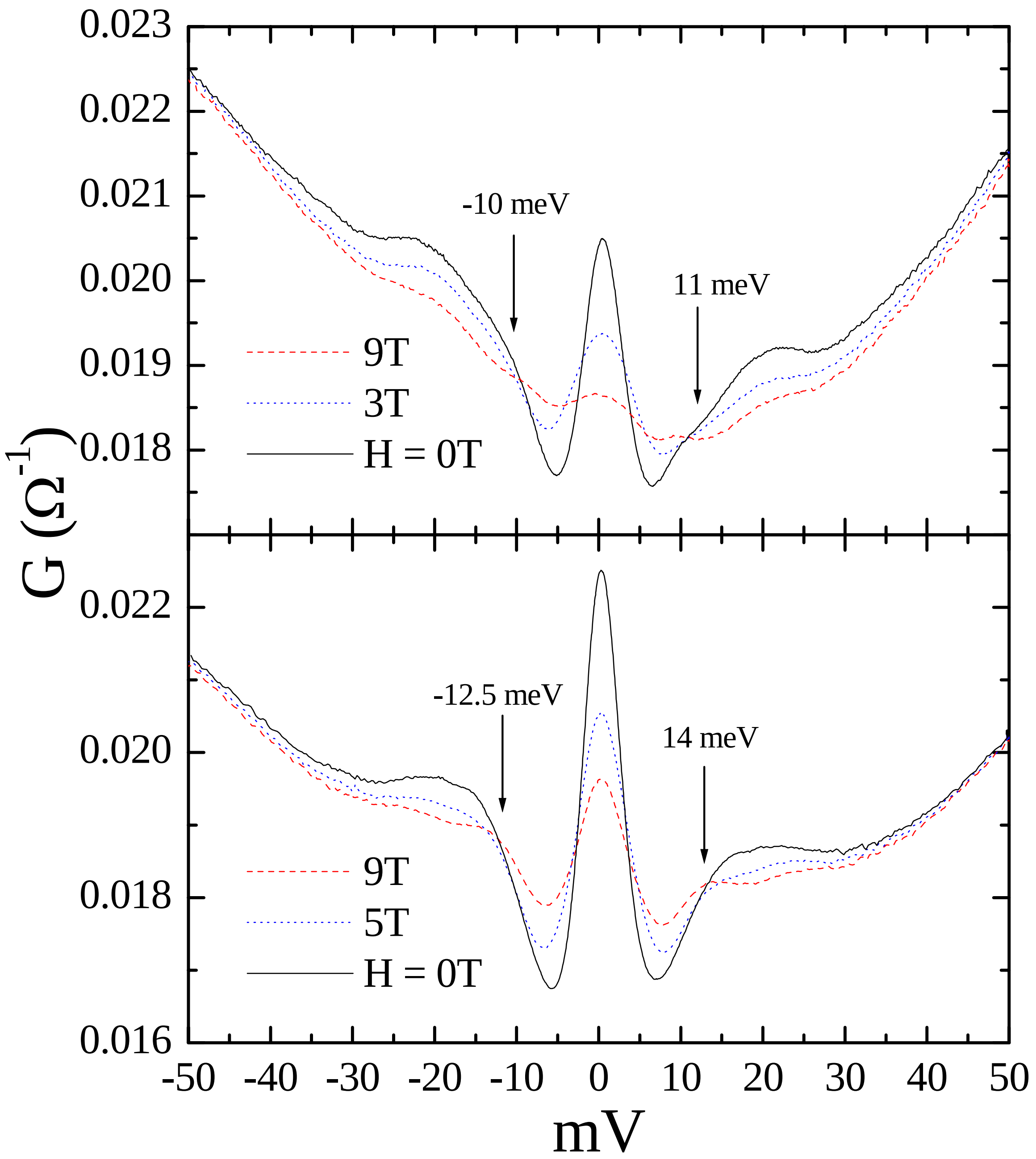

Figure 5.14. Shoulders observed in the magnetic field dependence of these (110)-oriented tunnel junctions fabricated with silver paste counter electrodes. The field suppresses the GLF and the ZBCP while the shoulder feature remains relatively unchanged. The energy values of the shoulders are noted and are consistent with the shoulder observed in data in Figure 5.11.

5.7 Conclusions

Orientation dependence of the tunneling conductance is noted most strongly when comparing junctions fabricated on (001)-oriented YBCO to the three orientations with *ab*-plane exposure, namely, (103)-, (100)-, and (110)-oriented YBCO, but anisotropy also exists between the different *ab*-plane orientations. Recall from Figure 5.1 that in tunneling into (103)-oriented YBCO, quasiparticles are injected nominally at a 45^o angle to the CuO_2 planes. Due to the cylindrical Fermi surface in YBCO, tunneling into the planes has a higher probability. Thus, *c*-axis tunneling can be ignored, and (103) tunneling can be considered as injecting quasiparticles directly along the *a*-axis, and is therefore equivalent to (100) tunneling.

Both of these orientations, however, share an anisotropy with (110) tunneling due to the *d*-wave nature of the superconducting order parameter in YBCO [5, 6]. Quasiparticles traveling along the *a*-axis should see the maximum gap while the gap along the (110) direction is expected to be zero. The GLFs, however, are measured at all *ab*-plane orientations. Furthermore, the ABS, which is expected to be absent in *a*-axis tunneling is also measured at all *ab*-plane orientations. This is likely due to faceting [7] at the YBCO surface, which causes a distribution of orientations to be probed in the tunneling measurements. Modeling of this effect is given in Section 6.3. Given the large number of junctions measured with the zirconia coating method, however, we have been able to measure an anisotropy in the value of the GLF_L as a function of orientation. Figure 5.15 shows histograms of the values of the GLF_L measured for junctions fabricated on (110)-oriented YBCO and for junctions fabricated on (100)- or (103)-

oriented YBCO. The result is a 1.15 meV difference in the measured values of the two *ab*-plane orientations.

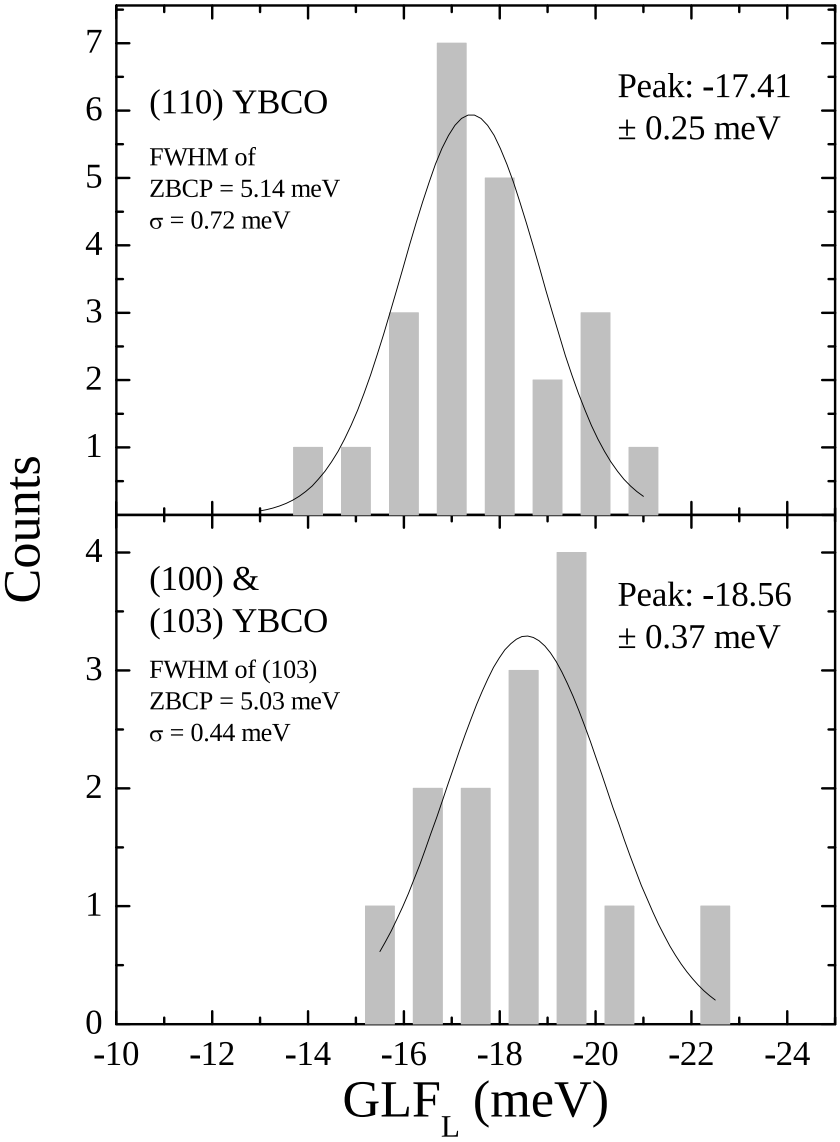

Figure 5.15. Histograms of the GLF_L values for tunneling along the (110)-direction and for tunneling along the *a*-axis are given. Direct *a*-axis tunneling shows a larger value for the GLF_L within statistical error. The values for the FWHM of the ZBCP are also given for comparison for junctions fabricated with silver paste counter electrodes on zirconia-coated (110)- and (103)-oriented thin films.

Asymmetry in the quasiparticle spectrum is commonly measured at every orientation. Asymmetry in the data from (100)-oriented films was observed in the differing values for ΔGLF_L and ΔGLF_R as well as the individual components of the doublets. Asymmetry is also routinely measured in the magnitudes of the GLFs at every orientation. It is not a background effect, as it is observed in the normalized data as well as the raw data, though asymmetry is routinely observed in the background as well. In nearly all cases, asymmetry is characterized by an enhanced value of the GLF_L relative to the GLF_R, as seen, *e.g.*, in Figure 5.11. An asymmetry is also observed in the ZBCP, the base of the right side of the ZBCP is typically at higher conductance than the base on the left side, causing the peak to be shifted from zero to 0.2–0.4 meV. This asymmetry persists in measurements of the splitting of the ZBCP, as shown in Chapter 6. The origin of the asymmetry is unknown, though it is likely due to an asymmetry between electron-like and hole-like quasiparticle spectra and is routinely measured by other groups. More extreme cases of asymmetry have also been observed [8].

Sharpness of features due to novel junction fabrication technique has uncovered features previously undetected in planar tunneling: double peak structure only measured in single crystal tunneling [9] and shoulder-like features inside GLF. In particular, the magnetic field dependence of the shoulder-like features has never been reported.

5.8 References

1. J.M. Rowell, in *Tunneling Phenomena in Solids*, E. Burnstein and S. Lundqvist, Editors. 1969, Plenum: New York.
2. S.L. Cooper and K.E. Gray, in *Physical Properties of High Temperature Superconductors IV*, D.M. Ginsberg, Editor. 1994, World Scientific: Singapore. p. 61.
3. J.R. Kirtley and D.J. Scalapino, Phys. Rev. Lett. **65,** 789 (1990).
4. A. Damascelli, Z. Hussain, and Z.-X. Shen, Rev. Mod. Phys. **75,** 473 (2003).
5. C.C. Tsuei, J.R. Kirtley, C.C. Chi, L.S. Yu-Jahnes, A. Gupta, T. Shaw, J.Z. Sun, and M.B. Ketchen, Phys. Rev. Lett. **73,** 593 (1994).
6. D.A. Wollman, D.J. VanHarlingen, W.C. Lee, D.M. Ginsberg, and A.J. Leggett, Phys. Rev. Lett. **74,** 797 (1995).
7. M. Fogelstrom, D. Rainer, and J.A. Sauls, Phys. Rev. Lett. **79,** 281 (1997).
8. B.A. Davidson, R. Ramazashvili, S. Kos, and J.N. Eckstein, Phys. Rev. Lett. **93,** 107004 (2004).
9. M. Gurvitch, J.M. Valles Jr., A.M. Cucolo, R.C. Dynes, J.P. Garno, L.F. Schneemeyer, and J.V. Waszczak, Phys. Rev. Lett. **63,** 1008 (1989).

Chapter 6

Andreev Bound State Studies

Chapter 5 demonstrates the overall planar tunneling conductance characteristics observed on zirconia-coated YBCO thin films as a function of crystallographic orientation and using various counter electrode deposition methods. In all cases, for the three orientations in which the *ab*-plane edge is exposed to the surface, a ZBCP is observed. This feature has been attributed to a surface-induced ABS in YBCO [1]. Magnetic field (magnitude [2] and orientation [3-5]), crystallographic orientation [6, 7], disorder [8] and temperature [7, 9, 10] dependencies of the ZBCP have confirmed this is the case.

6.1 Temperature Dependence of the ABS

Since the ABS is the result *d*-wave symmetry of the order parameter in YBCO, it is present at any temperature below T_c. The ABS has been detected up to T_c on grain boundary junctions (GBJ) of $La_{1.85}Sr_{.15}CuO_4$ (LSCO) [9] and on planar junctions on single crystals of $Bi_2Sr_2CaCu_2O_8$ (BSCCO) [10]. In the case of LSCO, T_c = 24 K, so the lack of significant thermal broadening facilitated the detection of the ABS up to the T_c of the sample. In the case of BSCCO, the high-quality surface of the single crystal enabled sharp conductance characteristics that allowed the detection of the ABS up to the bulk transition in the sample (T_c = 95 K). Before the use of our novel solution-based zirconia insulator deposition method, the ABS and other superconducting features had never been detected up to the critical temperature in YBCO thin films. Figure 6.1 shows the temperature dependence of the conductance of a zirconia-coated, (103)-oriented YBCO thin film. An enhancement of the conductance at zero bias is clearly visible just below the bulk onset of superconductivity in the film (T_c = 91 K).

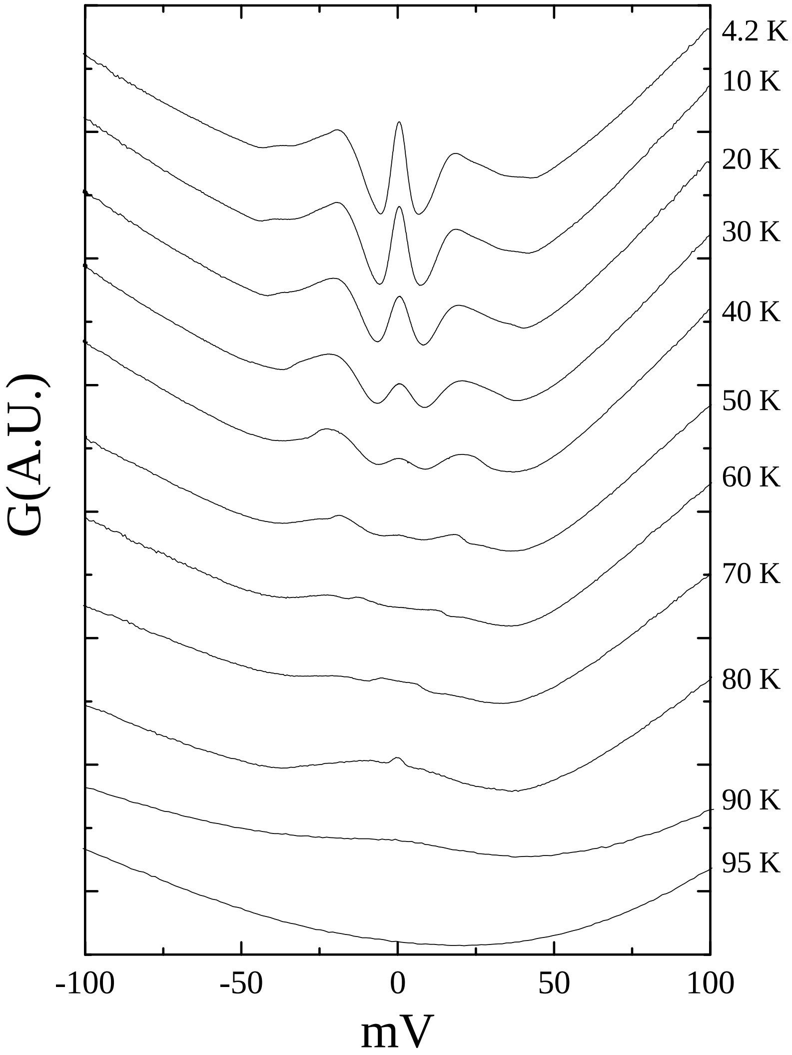

Figure 6.1. Temperature dependence of the tunneling conductance of a zirconia-coated, (103)-oriented YBCO thin film. Due to the sharpness of the characteristics, superconducting features are detected just below the bulk onset of superconductivity in the film (T_c = 91 K). The data are offset for clarity.

Though the ABS is present for any *ab*-oriented surface of YBCO, except for a perfectly smooth specular (100) surface, the magnitude of the ABS is maximal for the (110) surface and in this case, for a perfectly smooth surface in the pure tunneling regime, the ABS approaches a delta function as temperature approaches zero. This makes calculation of the temperature dependence of the zero-bias conductance (ZBC) in this perfect case a simple task. G($eV = 0$) is simply given by the convolution of the ABS delta function with the derivative of the Fermi occupation function, *df(eV,T)/d(eV)*. Convolution of any function *f* with a delta function simply returns *f*. Thus, since the Fermi function is given by

$$f = (1 + e^{-eV/k_B T})^{-1}, \qquad (6.1)$$

and the derivative *df(eV,T)/d(eV)* is given by

$$\frac{df(eV,T)}{d(eV)} = \frac{1}{4k_B T}\cosh^{-2}\left(\frac{eV}{2k_B T}\right), \qquad (6.2)$$

this implies G($eV = 0$) $\propto 1/T$ [11].

In any real junction, however, the ZBCP has finite width. This width is present in many models in different manifestations. The original *d*-wave calculation [12], based on Blonder, Tinkham and Klapwijk's tunneling kernel [13] produces a finite width to the ABS as a function of barrier strength as the spectrum transitions from the pure Andreev reflection limit to the pure *d*-wave tunneling limit. Thus, for any finite barrier strength, ZBC must be finite, but this width decreases monotonically with increasing barrier strength.

Walker *et al.* [14] point out that back-tunneling of the ABS quasiparticles into the normal metal produces a finite lifetime of those quasiparticles, imparting a finite line width to the ABS resonance. They argue, however, that such a lifetime is dominated, in the case of rough surfaces (rough compared to the Fermi wavelength) by surface Umklapp scattering, which imparts a universal width to the ZBCP. They point out that measurements of the ZBCP on YBCO are typically 4–6 meV, independent of surface disorder and tunneling technique. The average values listed in Chapter 5 are consistent with these results, even though, according to AFM measurements, the surfaces of our thin films are smoother than the roughness regime considered by Walker *et al.*

Another model for the finite width of the ABS, first employed by Dynes *et al.* [15] attributes the finite lifetime of the ZBCP to inelastic scattering processes that eventually lead to recombination of the of the quasiparticles into Cooper pairs. This is modeled by replacing the quasiparticle energy E in the expression for the DoS with the term $E - i\Gamma$, causing an exponential decay of the quasiparticle over a timescale given by $1/\Gamma$. When considering the temperature dependence of the ZBC, all of these techniques give qualitatively the same result: a broadening of the ZBCP such that it maintains a finite width, even as $T \to 0$. A natural way to model the ABS, which reflects the resonant nature of the bound state and produces a finite width employs an expression similar to that used by Walker *et al.* [14]. The ABS is described by a Lorentzian-like function given by

$$G_{ABS} \propto \frac{\Gamma^2}{eV^2 + \Gamma^2}\,. \tag{6.3}$$

As is the case for the ABS on a real surface, this function does not diverge at $eV = 0$. Convolving this function with $df(eV,T)/d(eV)$ produces a temperature dependence of the ZBC that approximately follows $1/T$ at high temperature and saturates as T approaches zero. Figure 6.2 shows the temperature dependence of the ZBC of a zirconia-coated, (110)-oriented YBCO thin film tunnel junction. We find that $1/T$ fits the data very well down to ~ 15 K, below which the ZBC begins to saturate. The saturation effect is well described by a numerical simulation of the convolution of the Lorentzian-like term with *df(eV,T)/d(eV)*.

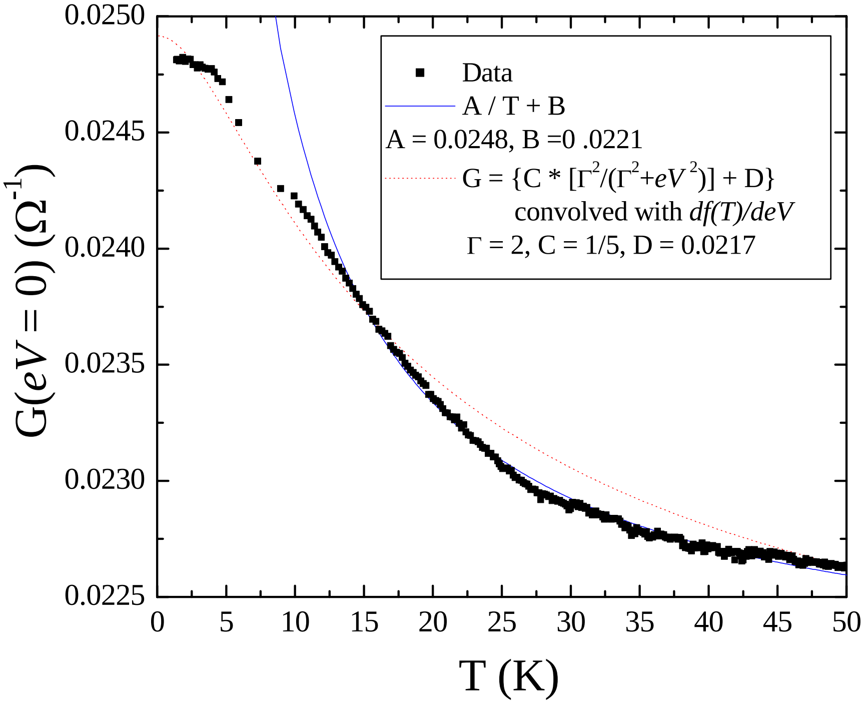

Figure 6.2. Temperature dependence of the ZBC of a zirconia-coated, (110)-oriented YBCO thin film tunnel junction (data points). $1/T$ (solid line) describes the high temperature behavior but cannot account for the saturation at low T, which is modeled by the Lorentzian-based term, as described in the text.

6.2 Field Dependence of the ABS

Field Orientation Dependence

As described in Section 2.2, the presence of a supercurrent couples to the ABS causing a shift in the ABS energy away from zero bias, given by $\varepsilon_B = \pm v_F \bullet p_S$. Quasiparticle trajectories moving along the direction of the supercurrent are shifted upward in energy; those moving counter to the supercurrent are shifted downward. Since the ABS is bound to CuO_2 planes, v_F is always in the plane so that only supercurrent (p_S) along the CuO_2 planes can cause the energy shift. Thus, the ABS is affected only when the field is oriented perpendicular to the planes; applying a field along the planes has no affect. Figure 6.3 shows this anisotropy. Though the ZBCP shown in the figure is already split in zero field, no further splitting, indeed, no effect at all is detected for H = 0–5 T. Applying a field perpendicular to the planes, however, does result in further splitting.

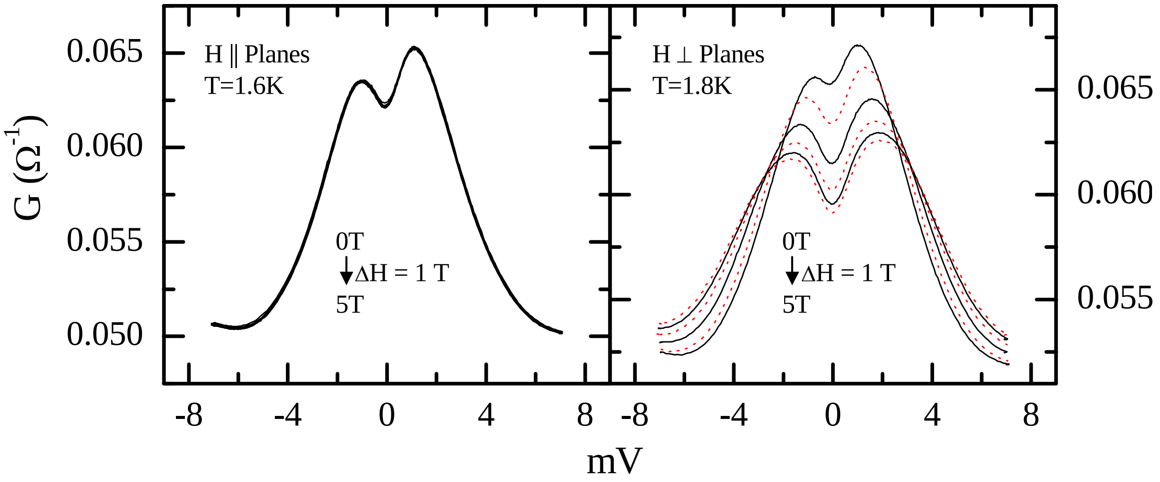

Figure 6.3. Magnetic field orientation dependence of the ABS in (103)-oriented YBCO fabricated with a zirconia barrier and evaporated silver counter electrodes. Though the peak has already split for H = 0, no further splitting is measured with applied field parallel to the CuO_2 planes. Applying the field perpendicular to the planes, however, does produce further splitting.

Field Magnitude Dependence: Splitting vs. Non-Splitting of the ZBCP

Spontaneous splitting, as shown in Figure 6.3, does not always occur, nor does the ABS always split with applied field, even when applied perpendicular to the CuO_2 planes. Whether or not a splitting is detected depends on several factors. Junction fabrication method and CuO_2 plane orientation in our studies and surface disorder [7, 9] and carrier doping [16, 17] in other work have been shown to influence the presence and magnitude of the splitting or suppression of the ZBCP.

The type of counter-electrode used to fabricate the junction affects whether or not splitting is observed in the field dependence of the ABS. Field dependence measurements on four different junctions fabricated with pressed indium counter electrodes always showed splitting of the ABS. While junctions fabricated with silver paste counter electrodes showed a suppression in of the ABS with applied field perpendicular to the CuO_2 planes on eight different junctions, they never showed splitting. Junctions fabricated with evaporated silver counter electrodes have mixed results. The data shown in Figure 6.3 come from a junction fabricated with evaporated silver counter-electrodes but this was the only time splitting was observed. Four other junctions using this counter-electrode deposition technique did not show splitting. The different magnetic field dependencies observed for the different types of counter electrodes are shown in Figure 6.4.

Crystallographic orientation of the YBCO thin film on which the junction is fabricated has a strong influence on the effect of applied magnetic field on the ABS as well. This is also shown in Figure 6.4. In this figure, data from junctions fabricated on (103)-oriented thin films consistently show a stronger field effect than junctions fabricated with the same technique on (110)-oriented YBCO thin films. It should be noted, however, that the counter-electrodes used in the top two panels are different. The evaporated silver junction is used for comparison in this case since no pressed indium junctions were fabricated on (103)-oriented films, and since splitting was observed in both junctions. This same anisotropy is observed by Beck *et al*. [18] when comparing the splitting of pressed indium junctions on bare (110)-oriented YBCO thin films to the same type of junctions on (100)-oriented YBCO. Since tunneling into (103)-oriented films probes the *a*-axis, as described in Section 5.7, this is consistent with our results. Furthermore, we performed one successful field-dependent experiment on a silver paste junction fabricated on a (100)-oriented thin film and the result was a very weak suppression of the ABS. The crystallographic orientation effect on splitting for the two ZBCPs in Figure 6.4 that show splitting is quantified in Figure 6.5.

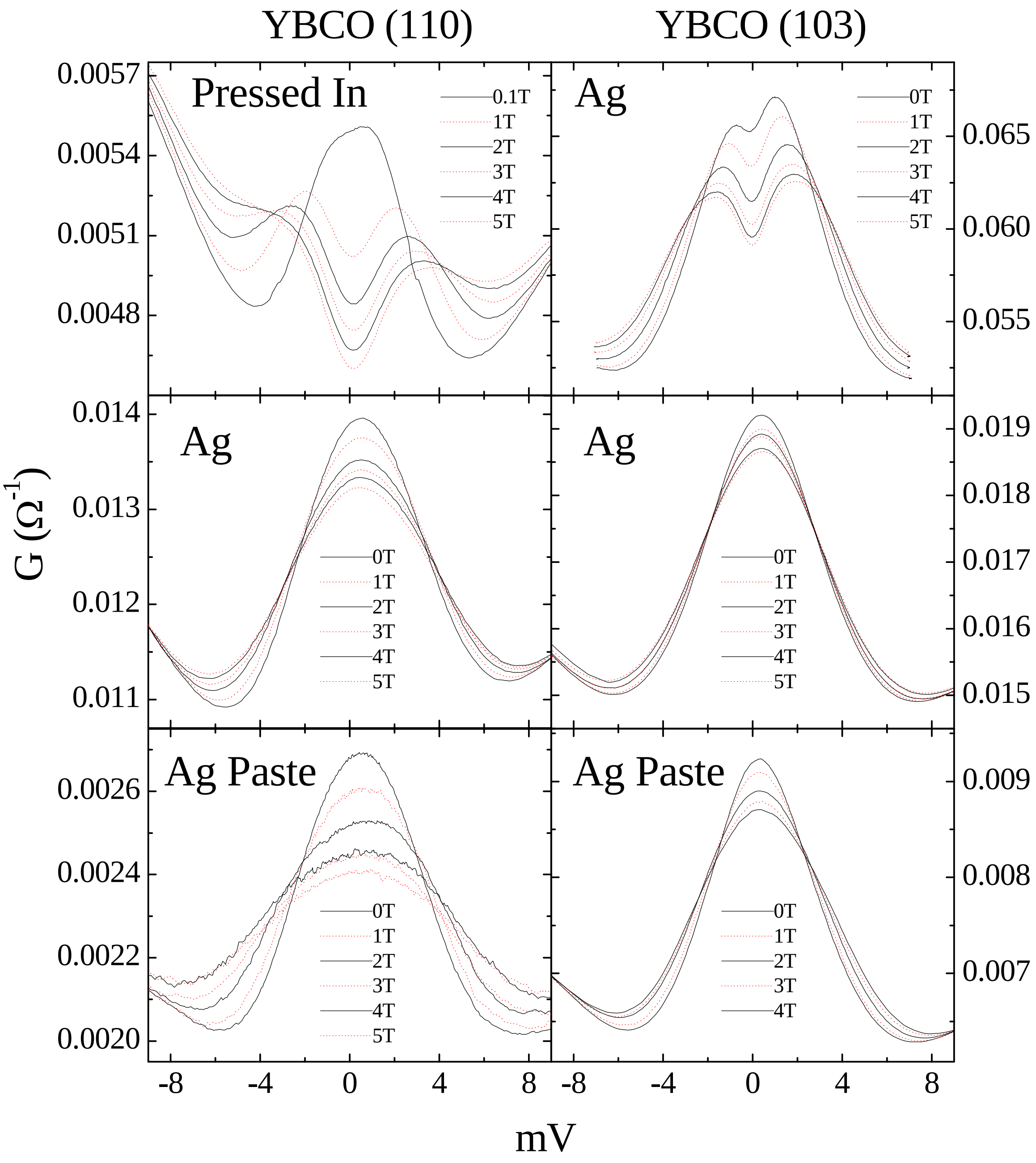

Figure 6.4. Magnetic field dependent measurements on various types of junctions fabricated on zirconia-coated YBCO thin films of two different orientations. The effect of the field is always stronger on (110)-oriented YBCO, but splitting is not always observed.

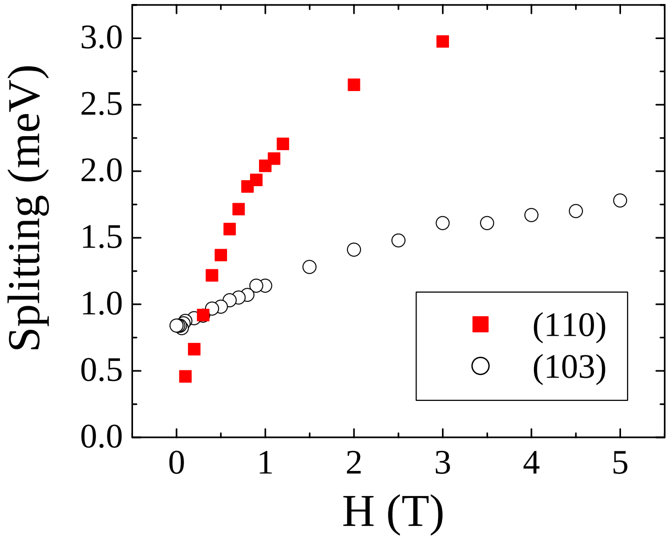

Figure 6.5. Measured ABS splitting as a function of applied magnetic field for the two junctions in Figure 6.4 that exhibit splitting. The splitting is defined as half the distance (in meV) between the two components of the split peak. The effect of the magnetic field is stronger on ABS observed on (110)-oriented YBCO thin films.

Hysteresis in the ABS splitting as a function of the direction of the field sweep (*i.e.*, sweeping up or down in field) has been measured previously [3, 4], and this has been observed in our measurements. In addition to hysteresis in the position of peaks, however, differences are noted in the shape of the split peak when sweeping upward in field versus sweeping downward. This effect is seen in the pressed indium junction in Figure 6.4. We analyze this effect by dividing low-field data from the data taken at higher field. Low field (0.035 T) data is used for normalization rather than zero-field data since this small field is required to quench superconductivity in the indium counter electrode. The result of this analysis is shown in Figure 6.6. We find that spectral weight that moves to high bias during ramping up persists at high bias during ramping down in the data shown.

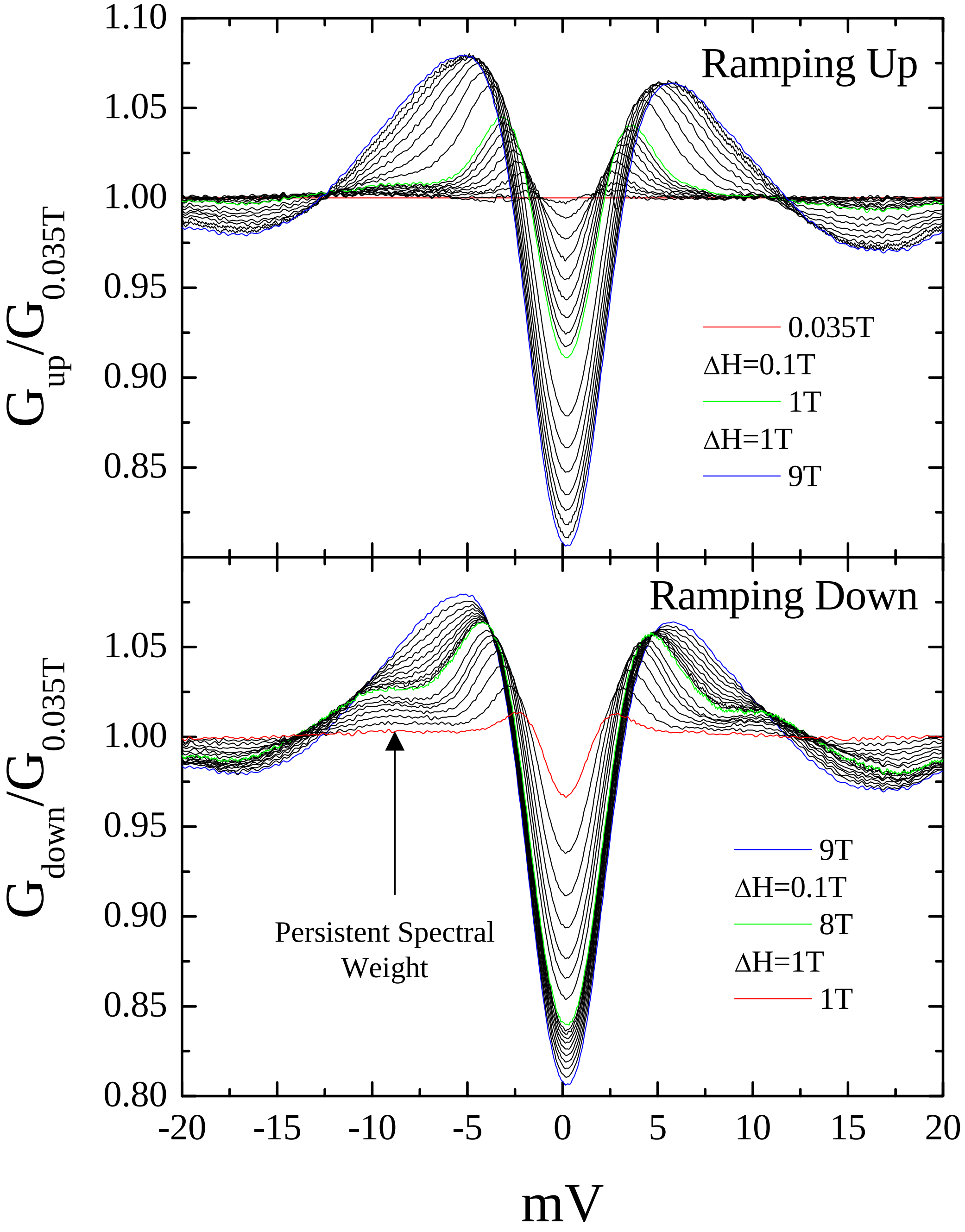

Figure 6.6. Magnetic field-dependent conductance data from a zirconia-coated (110)-oriented YBCO thin film fabricated with indium press counter electrodes. Each curve is normalized by data taken at 0.035 T. This small field is required to quench the superconducting indium. Data taken in increasing field is shown at top and in decreasing field at bottom. Hysteresis is observed not only in the position of the split peak but also in that the data taken in decreasing field exhibits persistent spectral weight at ± 7–12 meV. Further analysis is shown in the following figure.

Even after performing the normalization analysis to elucidate the splitting, interpretation can be difficult. A useful exercise is to compare two normalized curves with peaks at coincident energies. Due to the hysteresis in the splitting of the ABS, these data correspond to different applied fields. Figure 6.7 compares the data taken at 3 T ramping up to the data taken at 8 T ramping down. The persistent spectral weight in the ramping down data is clearly observed in this analysis.

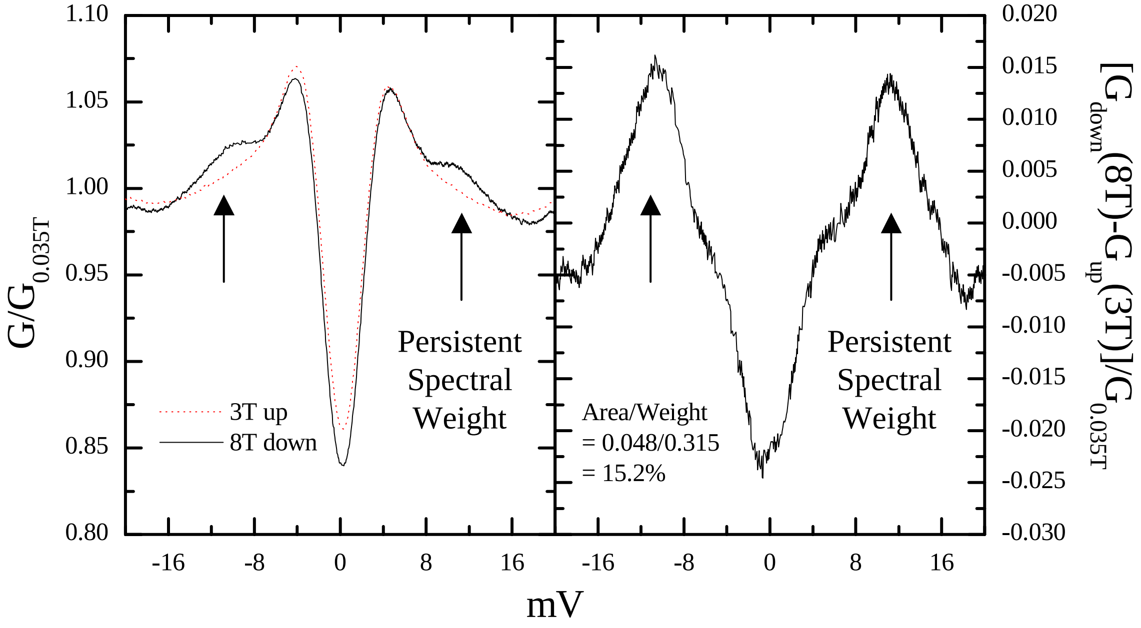

Figure 6.7. Analysis of the hysteresis observed in the field dependent tunneling measurements from the previous figure, showing one curve from each field ramping direction with coincident peaks in energy. The 3 T data (dotted line) from the ramping up dataset is shown, as is the 8 T data (solid line) from the ramping down dataset. Comparing these two curves clearly shows the persistent spectral weight in the ramping down data. The right panel shows the difference between these two curves, indicating where the excess and dearth in spectral weight reside. The spectral weight is conserved to within 15 % between the two curves.

Doping Dependence of ABS Splitting

Carrier doping in YBCO thin films has a strong effect on the splitting of the ABS as well. Dagan, Deutscher and coworkers have published extensive work on the dependence of the YBCO tunneling conductance on various values of doping and species of dopant [16, 17] using pressed indium counter electrodes on as-grown, (110)-oriented YBCO thin films. They find that for underdoped YBCO, no zero-field splitting is observed but the ABS can be split with a field, while for overdoping, the ABS is strongly split in zero field but does not split much further with applied field. Optimally doped samples do not show zero-field splitting in their work. Our results using zirconia-coated YBCO thin films with pressed indium counter electrodes are consistent with theirs. Our films are nominally optimally doped, show no zero-field splitting at 4.2 K (above the T_c of indium) and show splitting with applied field in all cases.

6.3 Modeling the Tunneling Conductance

To understand why splitting is not observed in most evaporated silver junctions, and all silver paste junctions, we must model not only the low-bias ABS region, but the higher-bias regions as well. The full surface DoS for a normal metal/insulator/*d*-wave superconductor junction was calculated in the tunneling limit by Fogelström *et al.* [19]. In their model, the surface DoS is given by

$$N(\theta,E) = \mathrm{Im}\left(\frac{\varepsilon(\theta,E)}{D(\theta,E)} - \frac{|\Delta(\theta)|^2}{D(\theta,E)\varepsilon(\theta,E)}\right), \text{ where}$$

$$D(\theta,E) = \sqrt{|\Delta(\theta)^2 - \varepsilon(\theta,E)^2} \text{ and} \tag{6.4}$$

$$\varepsilon(\theta,E) = E + i\Gamma + v_F \bullet p_S\,.$$

Here, the gap function $\Delta(\theta) = \Delta_0 \sin(2\theta - \alpha)$, where α describes the orientation of the surface. For (110)-oriented YBCO, $\alpha = 0$, and θ is measured from the surface normal.

In Equation 6.4, $N(\theta,E)$ describes the angle-resolved DoS, so to calculate what we expect to measure in the tunneling conductance, we must integrate over the measured trajectories. To quantify the tunneling cone, we define the transmission, $T(\theta)$, such that transmission is maximal at normal incidence and falls to e^{-1} at ϕ_c. Thus, we have

$$T(\theta) = \exp\left[\left(\frac{\cos(\phi_c)}{1-\cos(\phi_c)}\right)\left(\frac{\cos(\theta)-1}{\cos(\theta)}\right)\right]. \tag{6.5}$$

Furthermore, faceting at the tunneling interface is modeled by summing the contributions from a uniform distribution of values of α ranging from $-\phi_D$ to ϕ_D. Thus, the tunneling conductance is given by

$$G(eV) \propto \sum_{\alpha=-\phi_D}^{\phi_D} \int_{-\infty}^{\infty}\int_{-\pi/2}^{\pi/2} T(\theta)N(E)\frac{\partial f(E-eV)}{\partial(eV)}d\theta dE \tag{6.6}$$

The finite width of the ABS is determined by surface roughness and impurities, which lead to short quasiparticle lifetimes. The physics of these effects are contained the Dynes parameter Γ [15]. Increasing the value of Γ in the expression above broadens the ABS and other features and prevents splitting in the ABS from being observed in tunneling measurements. In addition to Γ, there is an additional parameter that affects the ability to observe splitting. The tunneling cone, ϕ_c, describes the distribution of quasiparticles incident on the superconductor in a tunnel junction. Since the splitting of the ABS goes as $\varepsilon_B = \pm v_F \bullet p_S$, only ABS trajectories with a significant component parallel to the interface are strongly Doppler shifted. If ϕ_c is small, however, the distribution of incident quasiparticles is closely centered around the normal to the interface, so that the states into which the quasiparticles tunnel are only weakly split by the Doppler shift. The tunneling cone is illustrated in Figure 6.8.

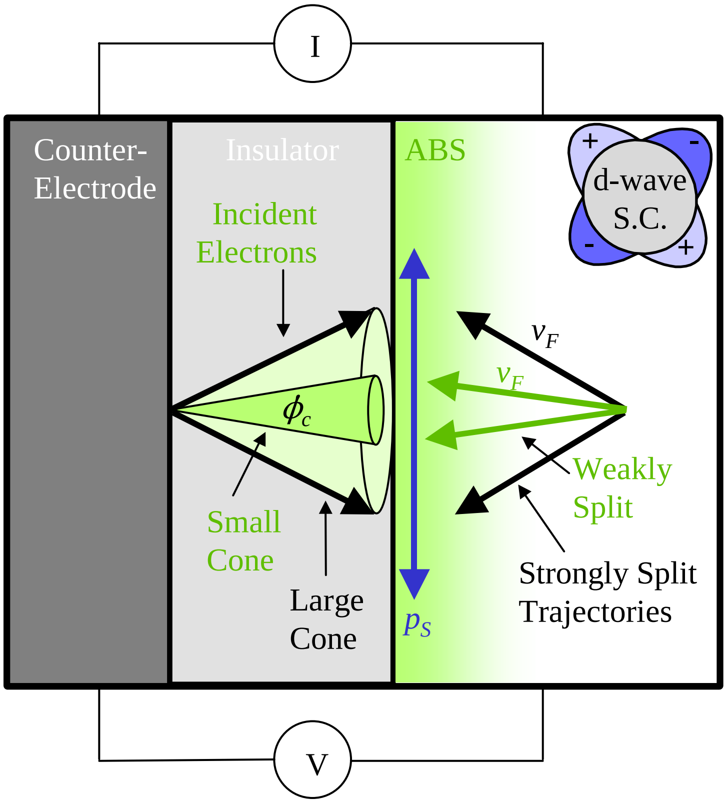

Figure 6.8. Illustration of the tunneling cone effect in a planar tunnel junction on a *d*-wave superconductor. Narrow tunneling cones probe only weakly-split quasiparticle states while larger cones detect a greater splitting.

Figure 6.9 shows the effects of the two angular parameters, ϕ_c and ϕ_D. We find that in the case of a small faceting parameter, ϕ_D (Figure 6.9a), coherence peaks are only resolved for the smallest values of ϕ_c considered. While, for larger values of the tunneling cone, ϕ_c (Figure 6.9b), faceting must be large in order for the coherence peaks to appear in the spectrum. This can be understood since in the small faceting limit, the few quasi-particle reflection trajectories without sign changes in the order parameter are located near normal incidence on the largest-angle facets. Thus, for these trajectories to make a significant contribution to the conductance, the cone must be narrow to prevent larger-angle trajectories (which contain sign-changes of the order parameter) from dominating the spectrum. For the case of a large tunneling cone, the faceting must increase to maintain the presence of the coherence peaks in the spectrum. The small-ϕ_c regime is important because our AFM measurements show RMS roughness values of less than 1 nm over a 150 nm square region. Thus, we believe these films are characterized by small values of ϕ_D. The large-ϕ_c regime is important to consider in other cases since it is necessary for detecting ABS splitting.

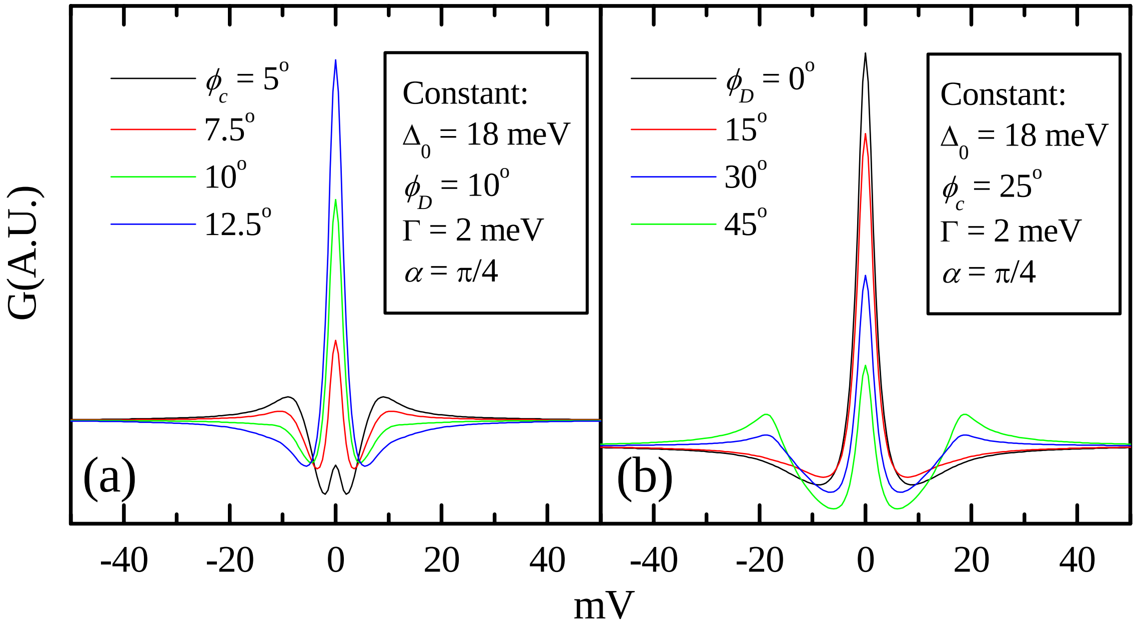

Figure 6.9. Simulations of the *d*-wave DoS showing the effect of varying ϕ_c (a), and varying ϕ_D (b). The results show that the coherence peaks are only observed for small ϕ_c for small ϕ_D, whereas for large ϕ_c, larger ϕ_D is needed for coherence peaks to be resolved.

Preliminary results of fitting the tunneling conductance data with this model (Figure 6.10) show that small values of ϕ_D are also necessary to reproduce negative curvature of the region inside the gap leading up to the GLFs, corroborating the AFM results of smooth surfaces. The fit concentrates on the negative bias region only, since asymmetry present in the data is not included in the model. Both fits reproduce the ABS shape and magnitude equally well. The region outside the GFL is not reproduced by either model. The deep drop in conductance outside the GLF is similar to the dip feature observed in *c*-axis data as shown in Figure 5.8, in which the lost spectral weight is attributed to DoS activity in that region. Since the model presented above assumes a *d*-wave BCS DoS function, no consideration is given to additional DoS activity outside the gap.

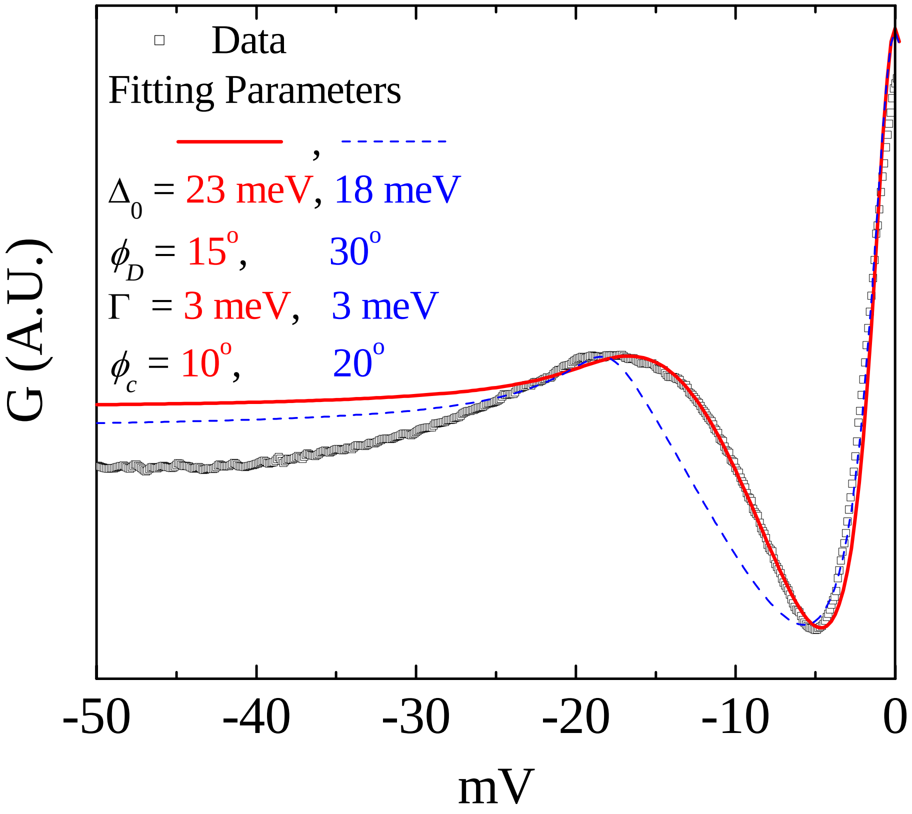

Figure 6.10. Tunneling conductance data taken on zirconia-coated, (110)-oriented YBCO thin films fabricated with silver paste counter electrodes are fit using two sets of parameters for the model described in the text. Each model fits the ABS feature equally well, while neither properly describes the region outside the gap. The fit with smaller ϕ_D (red) provides better fit to the gap region leading up the GLF, consistent with smooth films as measured by AFM.

Though the success of the fit corresponding to $\phi_D = 15^\circ$ speaks to the applicability of the model used here for (110)-oriented YBCO thin films, we find very little difference in the shape of the conductance measured for (110)-oriented films vs. (103)-oriented films which should be better fit by calculations using $\alpha = \pi/4$. However, this is not the case and further investigation is required to attempt to reconcile this result.

Simulations including the Doppler shift of the ABS, as shown in Figure 6.11, demonstrate the conditions necessary to observe splitting. The model shows that the energy shifts of the quasiparticle trajectories can be masked in the tunneling measurements either by a narrow tunneling cone (Figure 6.11a) or by large values of Γ (Figure 6.11c). The values of the Doppler shift are the same in all three simulations, the maximum of which corresponds to the value necessary to produce splitting in Figure 6.11b that matches what is typically observed in observations of splitting. Evidence for a narrow tunneling cone in our measurements is given by the fit in Figure 6.10. The fit also shows a small value of Γ relative to the value shown in Figure 6.11c necessary to mask the splitting. This suggests that the lack of splitting in all conductance measurements on silver paste junctions on *ab*-plane oriented YBCO thin films is due solely to a narrow tunneling cone.

Effect of Disorder on the ABS

Figure 6.11 shows that increased quasiparticle lifetime, modeled as an increase in Γ, leads to an increase in the FWHM of the ZBCP. Ion-induced damage at the YBCO surface has been studied by Aprili *et al* [8]. According to our analysis of the digitized data, the data show a roughly linear increase in FWHM of ZBCP with increasing ion flux. Values of the FWHM of the ZBCP range from 4.8 to 6.0 meV. In addition, the energy value of the GLF_L, which was visible at zero ion flux, had already diminished significantly by an ion flux of 1.0×10^{16} He^+/cm^2 (in the measurements, the flux ranges to 3.0×10^{16} He^+/cm^2).

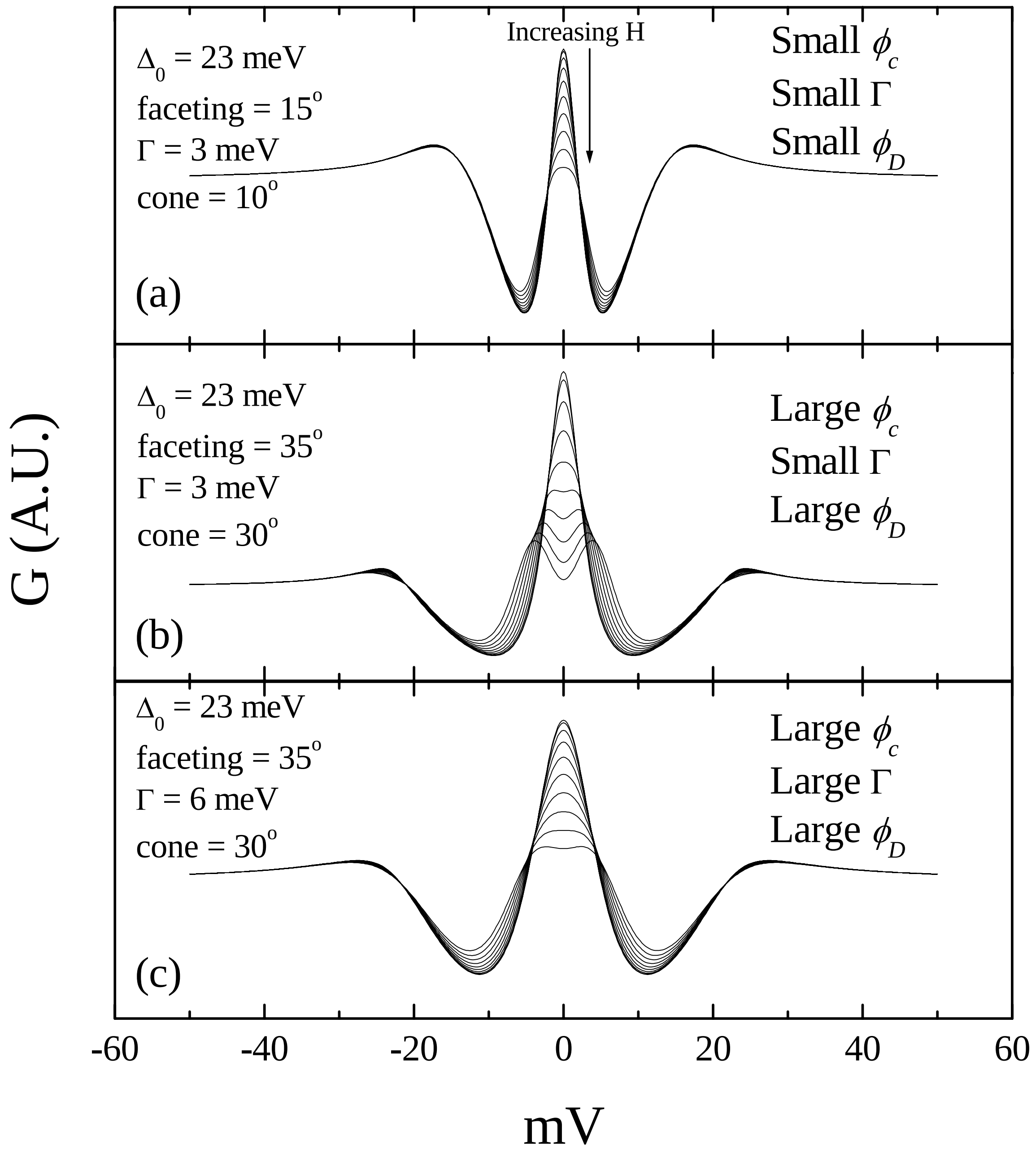

Figure 6.11. Simulations of splitting of the ZBCP for different parameter sets. The model shows that applying the Doppler shift to the best fit shown in Figure 6.10 (with small values of ϕ_c, ϕ_D, and Γ) produces no splitting (a), while increasing ϕ_c reveals the splitting (b). Note that ϕ_D must also be increased to maintain the presence of the coherence peaks. By simply increasing Γ compared to (b), though, splitting is quenched (c).

Tunnel junction fabrication techniques that inherently contain larger values of surface disorder also show increased FWHM of the ZBCP. Planar tunneling measurements on ramp junctions fabricated on YBCO thin films [7] also contain high values of atomic-scale surface disorder [20], due to the ion-milling process that defines the junction geometry. In this case, the data shows an average FWHM of the ZBCP of 7.1 meV. As stated in Section 5.7, the average values for the FWHM of the ZBCP in our measurements are 5.14 and 5.03 for (110)- and (103)/(100)-oriented YBCO, respectively. Thus, since larger values of Γ lead to broader ZBCP and GLF features (also measured in the Wang *et al.* data) it is likely that the lack of splitting consistently measured in ramp junctions is due primarily to large Γ.

A large value of Γ is also required to fit the data from the junction fabricated on (100)-oriented YBCO in Figure 5.10. In this case, no ZBCP is measured. We use $\alpha = \pi/4$ to simulate the (100) surface. We find that values of ϕ_D and ϕ_c in the fit in Figure 6.12 are larger than the best-fit values for *ab*-oriented films. Furthermore, while the overall shape is reproduced by the model, details of the shape inside the GLF are not. Since this fit is based on characteristics observed in only one junction, however, more data is needed before more extensive interpretation of the results can be justified.

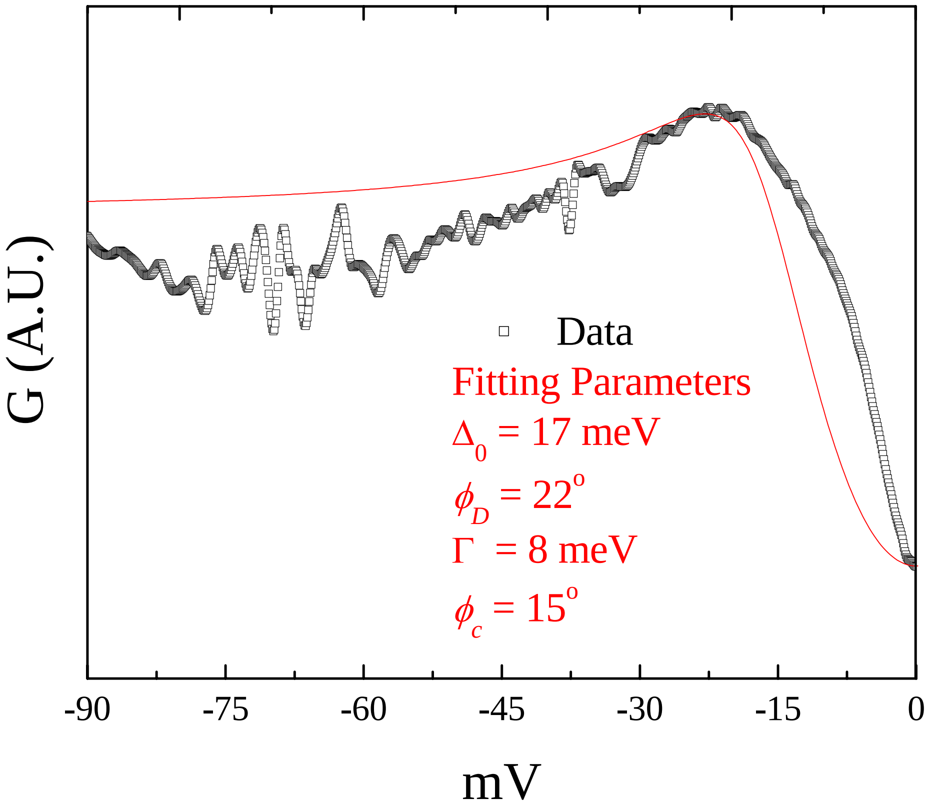

Figure 6.12. Data from the junction presented in Figure 5.10 are fit with the model discussed in the text for a (100)-oriented YBCO surface.

6.4 Current Injection Effects on the ABS

Since a magnetic field-induced supercurrent along he CuO_2 planes of YBCO splits or suppresses the ABS, it is natural to expect an injected supercurrent to have a similar effect. The bound state energy shift, given by $\varepsilon_B = \pm v_F \bullet p_S$, should not discriminate the source of p_S. We have performed current injection experiments on planar junctions of zirconia-coated (110)-oriented YBCO thin films, using silver paste, evaporated silver and pressed indium counter electrodes. The details are given here.

The pressed indium junction, for which magnetic field effects on the ABS are presented in Figures 6.4–6.7, was also used for current injection experiments. The YBCO thin film on which the junction was fabricated was 1000 Å thick and 5 mm wide. Assuming a penetration depth of ~1500 Å in YBCO, the current was approximately uniform across the thickness of the sample. The current was injected from silver strips that were evaporated across the width of the sample at each end, so that the current was as uniform as possible across the width of the sample as well. Since heating due to the injected current was a problem in early attempts at measurements, the sample was submerged in liquid helium, rather than being cooled by pumped helium vapor. The sample was mounted on a copper block with the Si diode temperature sensor mounted within the block, as shown in Figure 6.13.

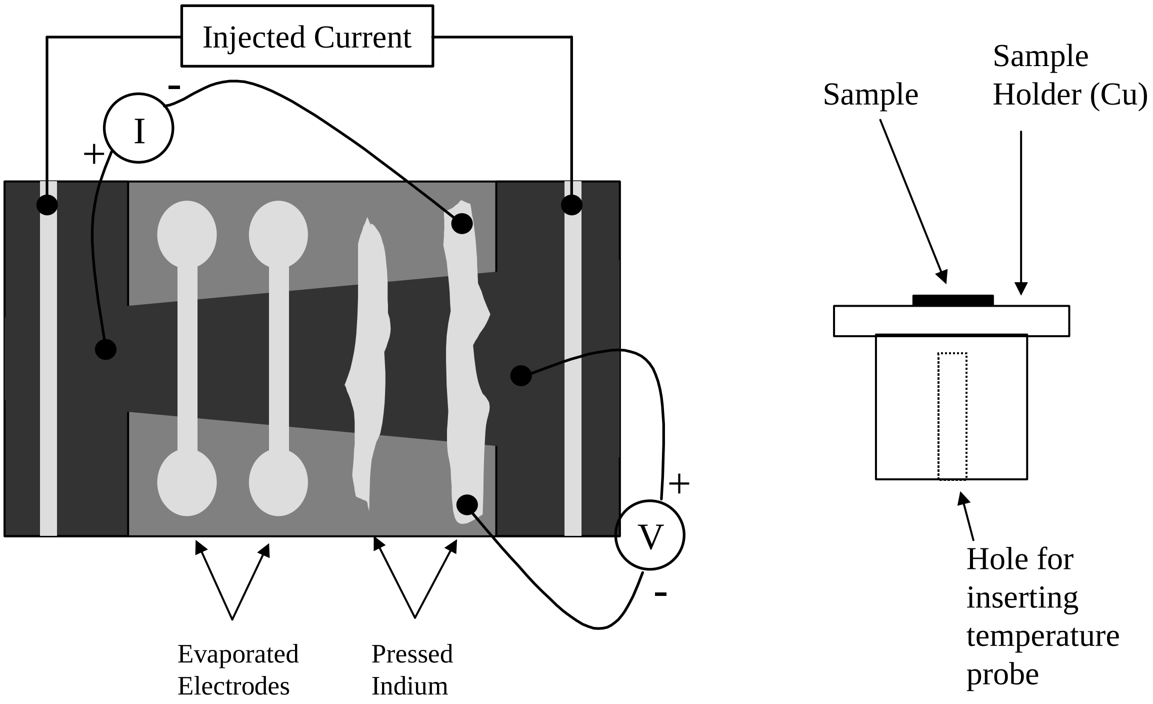

Figure 6.13. Schematic illustrations of the junction geometry for current injection tunneling measurements on YBCO thin films. The geometry is similar to that shown in Figure 3.5, but with added evaporated silver strips at each end for uniform current injection. The diagram on the right shows the sample holder used for these experiments, including the placement of the temperature probe.

The results of the current injection measurements are shown in Figure 6.14 and 6.15. Figure 6.14 shows the results for the pressed indium junction, in which the injection current, up to 50 mA, induces a suppression of the ZBCP. The temperature reading for all of the measurements except the 50 mA measurement was 4.2 K, as the measurements were performed in liquid helium. During the 50 mA measurement, however, the temperature reading from the embedded silicon diode sensor increased to 8.7 K. Furthermore, the spectrum at this temperature is broadened significantly, not only in the low-bias region, but also away from the ZBCP. This suggests significant heating, likely to a higher temperature than 8.7 K. It's possible that since the heater block was submerged in liquid helium, is was kept at 4.2 K in the measurements at lower values of the current, even while local heating took place on the YBCO film. If this was the case, heating could be the cause for the measured effect on the ZBCP for all values of injected current. Figure 6.14 also shows the effect of thermal broadening on the ZBCP. Due to the small range of data (– 15 meV, + 15 meV), edge effects prevent us from fitting the entire spectrum, but the simulations show that if heating alone is the cause of suppression of the ZBCP, the sample temperature was close to 30 K, rather than 8.7 K.

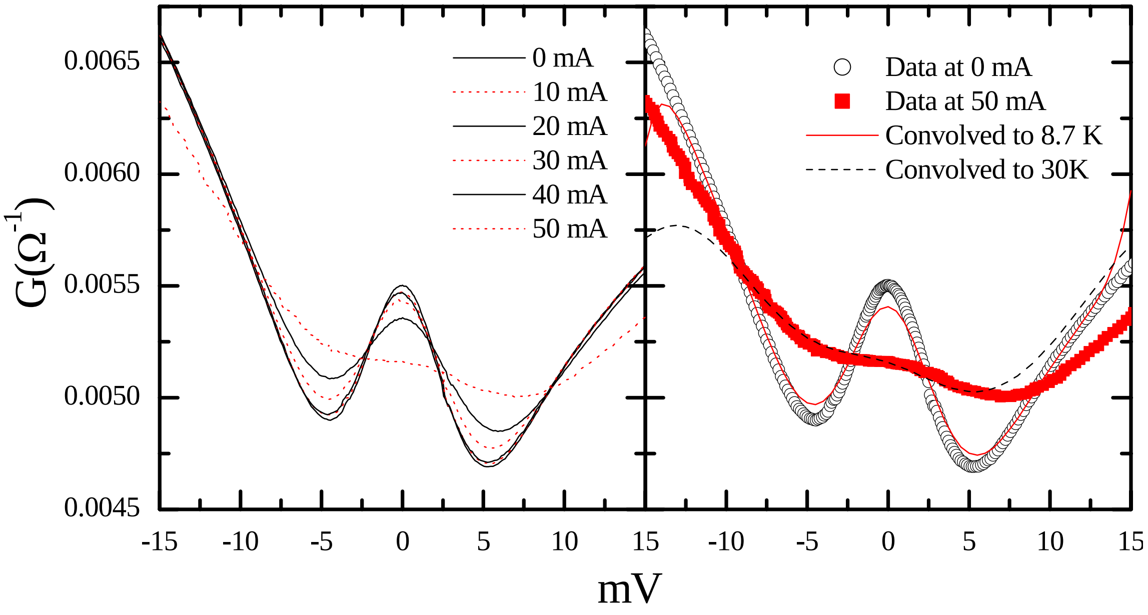

Figure 6.14. Current injection measurements (left) on zirconia-coated (110)-oriented YBCO thin films fabricated with pressed indium counter electrodes. The YBCO thin film is 2.5 mm wide and 1000 Å thick, resulting in a maximum current density of 2×10^4 A/cm^2. Increased current gives a suppression of the ZBCP, but the effect could be due to heating. If heating is the only cause of the changes in conductance, the sample temperature is more likely to be at 30 K than the measured 8.7 K, according to the simulations of thermal broadening (right).

Measurements on a junction fabricated with an evaporated silver counter electrode gives further support that current injection in our experiments does not induce changes in the ABS. Figure 6.15 shows the data from this experiment. We see no effect with an injected current of ± 100 mA in the sample. Contact resistance in this junction was improved and the measurements were taken in pumped helium vapor, so that any joule heating of the sample would be better detected by the temperature sensor. No deviations in the temperature (1.5 K) were observed during the current injection experiments. The sample cross sectional area is the same as the previous experiment, yielding a current density of 4×10^4 A/cm^2. The results of applied magnetic field perpendicular to the CuO_2 planes on this sample are also shown and a suppression is measured. Similar measurements on a junction fabricated with silver paste counter electrodes show the same results, *i.e.*, no effect due to the injected current.

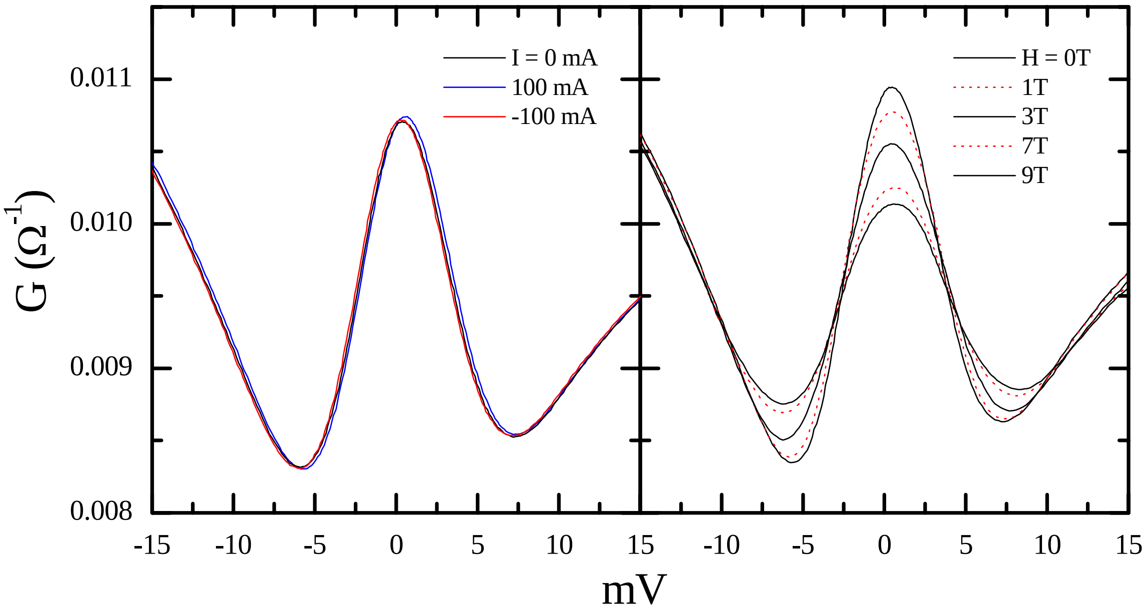

Figure 6.15. Current injection measurements on a zirconia-coated (110)-oriented YBCO thin film. The data show no effect due to the injected current of ± 100 mA (4×10^4 A/cm^2). Magnetic field dependent measurements on the same film show suppression of the ABS.

Thus, we believe the suppression of ZBCP in the pressed indium junction experiment was due to joule heating of the film in the electrode contact region, with poor thermal coupling to the silicon diode thermometer. Furthermore, upon calculating the current equivalent to the field at 1 T, the current density across the film is given by

$$J(x) = \frac{B}{\mu_0 \lambda} \frac{\sinh\left(\frac{x}{\lambda}\right)}{\cosh\left(\frac{d}{2\lambda}\right)}, \tag{6.7}$$

where x is the coordinate that runs along the thickness of the sample and is measured from the center of the sample. Thus, at the surface (*x* = *d/2*), we have

$$J(surface) = \frac{B}{\mu_0 \lambda} \tanh\left(\frac{d}{2\lambda}\right). \qquad (6.8)$$

In our experimental geometry, a field of 1 T corresponds to 650 A, whereas our highest value of injected current was 100 mA. Thus, it is not surprising that we saw no effect due to injected current.

6.5 References

1. C.R. Hu, Phys. Rev. Lett. **72,** 1526 (1994).
2. M. Covington, M. Aprili, E. Paraoanu, L.H. Greene, F. Xu, J. Zhu, and C.A. Mirkin, Phys. Rev. Lett. **79,** 277 (1997).
3. M. Aprili, E. Badica, and L.H. Greene, Phys. Rev. Lett. **83,** 4630 (1999).
4. R. Krupke and G. Deutscher, Phys. Rev. Lett. **83,** 4634 (1999).
5. G. Deutscher, Y. Dagan, A. Kohen, and R. Krupke, Physica C. **341-348,** 1629 (2000).
6. L. Alff, H. Takashima, S. Kashiwaya, N. Terada, I. Toshimitsu, O. Kunihiko, K. Masao, and Y. Tanaka, in *Advances in Superonductivity IX*, S. Nakajima and M. Murakami, Editors. 1997, Springer-Verlag: Tokyo. p. 49.
7. W. Wang, M. Yamazaki, K. Lee, and I. Iguchi, Phys. Rev. B. **60,** 4272 (1999).
8. M. Aprili, M. Covington, E. Paraoanu, B. Niedermeier, and L.H. Greene, Phys. Rev. B. **57,** R8139 (1998).
9. L. Alff, A. Beck, R. Gross, A. Marx, S. Kleefisch, T. Bauch, H. Sato, M. Naito, and G. Koren, Phys. Rev. B. **58,** 11197 (1998).
10. H. Aubin, L.H. Greene, S. Jian, and D.G. Hinks, Phys. Rev. Lett. **89,** 177001 (2002).
11. Y.S. Barash, A.A. Svidzinksy, and H. Burkhardt, Phys. Rev. B. **55,** 15282 (1997).
12. S. Kashiwaya and Y. Tanaka, Rep. Prog. Phys. **63,** 1641 (2000).
13. G.E. Blonder, M. Tinkham, and T.M. Klapwijk, Phys. Rev. B. **25,** 4515 (1982).
14. M.B. Walker and P. Pairor, Phys. Rev. B. **59,** 1421 (1999).
15. R.C. Dynes, V. Narayanamurti, and J.P. Garno, Phys. Rev. Lett. **41,** 1509 (1978).
16. Y. Dagan and G. Deutscher, Phys. Rev. Lett. **87,** (2001).
17. Y. Dagan and G. Deutscher, Europhys. Lett. **57,** 444 (2002).
18. R. Beck, Y. Dagan, A. Milner, A. Gerber, and G. Deutscher, Phys. Rev. B. **69,** 144506 (2004).
19. M. Fogelstrom, D. Rainer, and J.A. Sauls, Phys. Rev. Lett. **79,** 281 (1997).
20. U. Schoop, M. Schonecke, S. Thienhhaus, S. Schymon, L. Alff, and R. Gross, Physica C. **351,** 200 (2001).

Chapter 7

Conclusions

As described throughout this work, a wide range of results have been observed in the literature on planar tunneling measurements on YBCO. The focus of this thesis is to address this range of results in attempt to reconcile discrepancies. The extreme surface sensitivity of planar tunneling motivates us to produce thin films of outstanding surface quality and this has been achieved, as demonstrated by AFM measurements showing atomically smooth regions of over 100 nm per side. The high surface quality is maintained through a novel insulator deposition technique employing solution-deposition of zirconia. AFM, TEM and tunneling spectroscopy measurements give evidence for very low surface damage. These high surface quality films, coated with solution-deposited zirconia insulators are used to fabricate planar tunnel junctions using three different counter-electrode deposition methods. Various results are obtained for different types of counter-electrodes and different crystallographic orientations.

Sharp features observed in the tunneling conductance spectra, allowing for detection of several new features. Double-peak structures in the GLFs of (001)-oriented YBCO thin film junctions are observed. Shoulders inside the gap in (103)- and (110)-oriented thin film junctions are detected and are shown to be robust to applied magnetic field. Finally, persistent spectral weight at ±12–17 meV in decreasing magnetic field measurements of the ABS is observed.

Splitting *vs.* non-splitting of the ABS has been a source of controversy in the literature. We observe both splitting and non-splitting of the ABS, depending on the counter-electrode deposition technique employed, and show that by modeling the tunneling conductance with different values of surface faceting, tunneling cone and quasiparticle lifetime, we can define regimes in which splitting of the ABS is, or is not, expected to be observed. We find that non-splitting spectra can be modeled in two regimes. The first is the small ϕ_c regime and the second is the large Γ regime, as described in Chapter 6.

Fits to our data from junctions fabricated with silver paste counter-electrodes on (110)-oriented YBCO thin films show that the characteristics are described by low values of Γ, ϕ_c and ϕ_D. Thus, the lack of splitting of the ZBCP in these data, with applied magnetic field perpendicular to the CuO_2 planes is due solely to the small value of ϕ_c in these junctions. Data from the literature with broad overall features compared to characteristics shown in this work, which do not show splitting of the ZBCP are described well by simulations in the large Γ regime. Data in this work and in the literature that do show a splitting of the ZBCP with applied field are characterized by larger values of ϕ_c but must have values of Γ small enough to reveal the splitting. By taking differing values of Γ, ϕ_c and ϕ_D into account, the splitting/non-splitting behavior observed in this work and in the literature is be understood in one consistent picture.

Future work includes additional experiments on (100)-oriented YBCO using optimized insulator deposition process to increase reproducibility and explore orientation dependence of the conductance spectra. Further studies of the persistent spectral weight observed in decreasing magnetic field measurements of the ABS are needed to elucidate this behavior. Preliminary measurements of the effect of current injection on the ABS have shown that higher current densities are needed to produce an effect, if it exists.

Patterned films will likely be necessary to achieve the current densities necessary to observe a splitting due to the current. However, surface effects of photolithographic processing must be carefully considered, as surface quality is of utmost important in these measurements. The passivation of the YBCO surface by the solution-deposited zirconia insulator may provide the protection necessary for successful tunneling measurements on patterned films. Finally, more complete modeling of the conductance spectra will provide further insight into the measurements. Including back-tunneling effects of ABS quasiparticles into the normal electrode in an extended BTK formulation will more accurately simulate quasiparticle lifetime effects on the ABS and allow for the modeling of various values of the barrier strength.

Vita

Patrick Jay Hentges was born in Jefferson City, Missouri on March 18, 1975. He lived with his family in the house his parents built until he left to attend Drury College (now Drury University) in Springfield, Missouri in 1993. After transitioning from Architecture, to Engineering, to Physics, he graduated B.A., Magna Cum Laude, with a double major in Physics and Mathematics in 1997. After a year of taking courses and teaching as a graduate student at the University of Illinois at Urbana-Champaign, he began work with Peter McCullough on a project to implement a robotic telescope used to map Balmer-alpha radiation for subtraction from the cosmic microwave background at the Mt. Laguna Observatory near San Diego, California. After working for a year on this exciting project, he changed focus and joined Laura Greene's group to study the electronic structure of the high-temperature superconductor $YBa_2Cu_3O_{7-\delta}$ in January of 1999. This work continued until the summer of 2004, when he was hired as a process engineer with Intel Corporation in Portland, Oregon.